AN ABSTRACT OF THE THESIS OF

Jason Magalen for the degree of Master of Ocean Engineering in Ocean Engineering presented on March 17, 2006.

Title:

A Laboratory Experiment on Sand Bar Migration with Comparisons to Recent Models

Abstract approved:

Merrick C. Haller

Successful prediction of nearshore sediment migration is important in determining the vulnerability of a coastline. During energetic wave climates (storm events) sediment rapidly erodes from beaches and is deposited offshore. In subsequent milder wave conditions, the sediment migrates shoreward, accreting on the beach and helping to protect the coastline. It is well understood that beaches undergo temporal variations on many scales (daily, seasonally, annually, etc.). However, predictions of the nature of beaches remain poor because the processes which govern the variability of the nearshore hydrodynamics and sediment dynamics are not yet understood well.

Recent modeling efforts using a process-based total load sediment transport model have predicted the offshore migration of sediment well, but have failed to predict onshore migration [*Thornton et al.* (1996); *Gallagher et al.* (1998)]. It has been suggested that onshore migration of sediment occurs when the velocity asymmetry and the closely related acceleration skewness are large. Recent empirical extensions to the total load sediment transport model have incorporated this hypothesis [*Hoefel and Elgar* (2003)]. The results were encouraging, but the model has only been applied to one field dataset. Therefore, to validate the model, additional comprehensive datasets of onshore migration are necessary.

A recent large-scale laboratory experiment (CROSSTEX) has augmented the number of comprehensive laboratory datasets that encompass migratory bar events. One offshore migration and two onshore migrations were observed over a four-week period. The nearshore hydrodynamics (water surface elevations, velocities and suspended sediment concentrations) were sufficiently measured with expansive cross-shore and vertical instrument arrays.

We applied two process-based sediment transport models using the observed cross-shore velocity data and compared the predicted beach profile evolution to the observed profile evolution. Results with a classical energetics total load model predicted neither the offshore nor the onshore bar migrations with a high degree of accuracy. Results with an empirical extension to the energetics model (acceleration-based) did not improve predictions of the offshore migration, but greatly improved predictions of the onshore bar migration. Best-fit model parameters were within a factor of three of those found by other researchers [*Hoefel and Elgar* (2003)].

Model predictability and accuracy was determined by quantifying the model predictive skill, a normalized rms error comparison of the model predictions to the observations. Model predictive skill was a reliable assessment tool when the skill level was high ($\simeq$1.0). However, if the skill level was low ($\simeq$0.0) or negative, it was not always indicative of poor model predictions.

A model sensitivity analysis was conducted to determine the effects that varying the coefficient of friction, low-pass filtering the velocity data and selecting the free parameters had on the model results. The model skill of predictions varied for different coefficients of friction. However, the model skill typically decreased as the friction coefficient increased.

Low-pass filtering of the data resulted in a decrease of model predictive skill and visually less appealing model predictions. This implied that high frequency noise infiltration had a significant effect on the model predictive capability, biasing the predictions in a positive manner. Model predictive skill decreased when the velocity data were low-pass filtered.

The acceleration-based model was relatively insensitive to variations in free parameters under energetic wave conditions. However, the model was highly sensitive to selection

of the free parameters when modeling milder wave conditions (onshore sediment migration). Therefore, the best-fit model parameters should be selected by tuning the model to the milder wave conditions during which onshore sediment migration occurs.

A Laboratory Experiment on Sand Bar Migration with Comparisons to Recent Models

by

Jason Magalen

A THESIS

submitted to

Oregon State University

in partial fulfillment of
the requirements for the
degree of

Master of Ocean Engineering

Presented March 17, 2006

Commencement June 2006

Master of Ocean Engineering thesis of Jason Magalen

presented on March 17, 2006

APPROVED:

Major Professor, representing Ocean Engineering

Head of the Department of Civil, Construction and Environmental Engineering

---

Dean of the Graduate School

I understand that my thesis will become part of the permanent collection of the Oregon State University libraries. My signature below authorizes release of my thesis to any reader upon request.

Jason Magalen, Author

ACKNOWLEDGEMENTS

I would like to thank Dr. Merrick Haller for his continuous patience, support and guidance throughout this learning process, and for teaching me the value of questioning my results. I would like to thank Dr. Tuba Özkan-Haller for her encouragement and unfailing ability to look positively upon numerical modeling results. The glass was always half full. From both, I have gained the confidence and skills necessary to approach complex problems with patience and resolve.

I would like to thank Tim Maddux and Linda Fayler and the O. H. Hinsdale Wave Research Laboratory staff for their help and patience planning and implementing my experiments, and for jumping to my aid and helping to put fires out when experimental "emergencies" arose.

I would like to thank Patricio Catalán for helping me get through some difficult struggles with an inexhaustible ability to explain coastal engineering theories at my level of learning. His uncanny knowledge of LaTeX programming, inside and out, is rivaled by no other. Additionally, I would like to thank Christopher Scott for all of his assistance in and out of the wave research laboratory; at times until very early in the morning. Furthermore, I would like to thank graduate students Joe Long and Greg Guannel for their invaluable assistance along the way.

I would like to thank Dr. Robert Holman and Dr. Thomas Plant for rounding out my committee with their helpful criticism and support.

I would like to thank my family, as well, for without their support, guidance, criticism and love, I would not be where I am today. Thank you for encouraging me to always try my hardest and teaching me the value of never giving up.

Finally, I would like to thank the love of my life, Holly, for being my biggest fan and supporter. Your ceaseless love and your endless patience helped me bring this chapter of my life to a close. The best is yet to come...

TABLE OF CONTENTS

TABLE OF CONTENTS (Continued)

TABLE OF CONTENTS (Continued)

TABLE OF CONTENTS (Continued)

LIST OF FIGURES

LIST OF FIGURES (Continued)

LIST OF FIGURES (Continued)

LIST OF FIGURES (Continued)

LIST OF TABLES

LIST OF TABLES (Continued)

1. INTRODUCTION

The shorelines and beaches of coastal zones act as the only natural protective barriers between the land and sea, helping to prevent wave energy from directly attacking the coastal bluffs and infrastructure. However, amidst heightening fears of rising sea level, coastlines are becoming increasingly populated. Thus, understanding the behavior of this protective interface has become a primary objective of coastal zone managers and researchers.

Nearshore surfzones are highly energetic regions that are influenced by random hydrodynamic processes. Storm events drive the wind waves, swell waves and infragravity waves that are superposed on tidal fluctuations and arrive at varying angles of incidence to the coastline. Subsequently, spatially and temporally varying nearshore currents are generated in the wave-breaking regions and cause changes in the morphology of the beach face and submarine profile. The resultant beach profile affects the behavior of the incident waves, and the cycle repeats itself.

It is generally accepted that storm seasons are characterized by increased breaking wave energy (from large wave heights and short wave periods), which generate an increase in offshore-directed mean flows (undertow). Turbulence from breaking waves suspends sediment while the undertow forces it offshore. A barred beach profile often results and is commonly referred to as a storm profile. When the stormy season subsides and wave energy decreases, sediment tends to migrate shoreward under non-breaking, asymmetric and skewed waves. The resulting beach shape is called the summer profile and is often characterized by a smaller, shoreward migrating sandbar and steep foreshore, or a non-barred "equilibrium" profile.

Seasonal variation of this kind is common to many shorelines, but temporal fluctuations in profile shape can also occur on the order of days, weeks, years and decades. During a storm, for instance, rapid offshore bar migration or formation may occur over the time period of a few hours to a few days. Following the storm activity, the sandbar

may immediately begin migrating shoreward. This is called the post-storm recovery period of the beach profile and is generally characterized by milder wave conditions (smaller wave heights and longer wave periods).

The submarine profile of a beach continuously tries to achieve equilibrium with the nearshore hydrodynamics. The large number of complex contributing factors to profile change has made morphological predictions difficult for researchers, however. Moreover, the effects of each individual contributing element are not understood well, reducing the ability to interpret the combined impacts accurately.

In recent decades, researchers have attempted to predict beach profile evolution through different conventions. Predictive model complexity has ranged from simple, descriptive models, which qualitatively describe beach states as erosive or accretionary, to process-based models which attempt to quantitatively predict sediment transport using observed hydrodynamics. Results have varied but have been encouraging. While the simpler models have their advantages, the process-based models remain under focus because they model the actual physics of the energetic nearshore.

Using the process-based models, offshore migration has been modeled with a high degree of success. Onshore sediment migration, though, has not been modeled with a large amount of success, in part because the processes by which it occurs are not yet well understood.

The largest hinderance to the advancement of onshore sediment transport modeling is the scarcity of available comprehensive datasets recording the migration (both field and laboratory) to validate theories. Experiments are costly (both in time and financial requirements). In addition, while offshore bars generally form rapidly under storm wave action, onshore sediment transport tends to be a lengthy process (e.g. time scales can range from days to decades). And, it generally is not feasible to deploy instruments in the field for time periods long enough to encompass an onshore migration event. Furthermore, wave climate is stochastic, making the planning of a field experiment devoted to capturing onshore bar migration difficult. Thus, the benefits of controlled laboratory experiments become evident, in which the incident wave conditions can be specifically selected. However, controlled laboratory experiments introduce additional factors that

contradict natural processes observed in the field (e.g additional effects from tank side walls, seiching, etc.).

In the following section, a range of beach profile evolution models will be described. Subsequently, field and laboratory experiments in which onshore migration was observed will be discussed.

1.1 Beach Evolution Models

Descriptive Models

Early sediment transport modeling efforts attempted to predict beach profile evolution based on the type of breaking waves. *King and Williams* (1949) suggested that sediment migrated shoreward under unbroken waves, and seaward under surf waves. *Greenwood and Davisdon-Arnott* (1979) found agreement with this theory, arguing that sandbars were dependent on the oscillatory motion of the waves in the nearshore. They hypothesized that outside of the surfzone, sediment was increasingly transported shoreward, while shoreward of the break-point the sediment transport decreased.

Other researchers attempted to predict profile evolution based on type of breaking wave [see *Sallenger et al.* (1985), and references therein.] *Miller* (1976) found plunging breakers to be the cause of bar formation when beginning from an initially flat beach profile. He also suggested that spilling breakers transport sediment shoreward from initially barred profiles, and form onshore migrating ripples when beginning from initially flat profiles. He reasoned that the turbulent energy from the plunging breaker extended to the bed surface causing sediment suspension while the turbulent bore of the spilling breaker remained near the water surface, not affecting the sediment at the bed.

Additional researchers suggested that standing wave or edge wave motions in the surfzone contribute to bar formation and migration [*Bowen* (1980)]; that drift velocities associated with these motions contribute to the convergence of sediment at the nodes (or antinodes) of the standing waves, depending on whether bedload (or suspended load) is the dominant transport mechanism [*Sallenger et al.* (1985)].

Within past decades, descriptive models attempted to classify beaches and beach

states over a range of environments and time scales [*Roelvink and Brøker* (1993)]. *Wright and Short* (1984) classified beaches in 6 states: dissipative, reflective, and four intermediary states. They found that the relevant hydrodynamic processes to sediment transport varied greatly depending on the state of a beach. Moreover, a beach state could be classified as erosional or accretionary based on its present state and its previous state. The six beach states of *Wright and Short* (1984) are:

1. Dissipative (fully erosional beach state)
2. Intermediate: Longshore Bar-Trough
3. Intermediate: Rhythmic Bar and Beach
4. Intermediate: Transverse Bar and Rip
5. Intermediate: Ridge-Runnel or Low Tide Terrace
6. Reflective (fully accreted beach state)

Wright and Short (1984) also compared the parameter

$$\Omega = \frac{H_b}{\bar{w}T} \tag{1.1}$$

to the beach modal state to determine the correlation with beach state. This was later termed the "Dean number" by *Dean* (1973). Here, H_b is the wave height at breaking, $\bar{w}$ is the sediment fall velocity and T is the wave period. They found that if $\Omega < 1$ then the beach was reflective (accretionary), if $1 < \Omega < 6$ then the beach was classified as an intermediary state, and if $\Omega > 6$ then the beach was dissipative (erosional) [*Wright and Short* (1984)].

Lippmann and Holman (1990) extended the 6-state beach stage model of *Wright and Short* (1984) to 8 states using time-averaged video images of incident wave breaking. Beach state (2): "longshore bar and trough intermediate" of *Wright and Short* (1984) was expanded into an "infragravity scaled 2-D bar" state and a "non-rhythmic 3-D bar" state. Secondly, beach state (4): "transverse bar and rip" of *Wright and Short* (1984) was expanded to an "attached rhythmic bar" and a "non-rhythmic, attached bar".

Lippmann and Holman (1990) found that sequential progression in the model from

a dissipative state to reflective state was associated with lower wave conditions, corresponding to accretionary wave conditions. Under higher wave energy conditions, the beach states were categorized near the dissipative side of the spectrum, implying erosional conditions. Furthermore, they suggested that longshore linear sandbars tended to form under increasingly energetic incident wave conditions, and that three-dimensional bars formed rapidly as the wave energy decreased.

Researchers also examined the use of simple beach descriptors to predict whether a beach will erode or accrete [*Wright and Short* (1984); *Kraus et al.* (1991)]. *Kraus et al.* (1991) consider (among other criterion) the wave steepness,

$$S_o = \frac{H_o}{L_o}, \tag{1.2}$$

and the parameter,

$$D_o = \frac{H_o}{wT} \text{ (another version of the "Dean number")} \tag{1.3}$$

[*Dean* (1973); *Kraus et al.* (1991)]

where H_o is the deep water significant wave height, L_o is the deep water wavelength and w is the fall speed of the sediment. They found a relationship between the wave steepness and Dean number to determine erosional or accretionary wave conditions:

$$S_o = M \cdot D_o^3, \tag{1.4}$$

where M is the slope of the line of separation. The slope value, $M = 0.00027$ was empirically derived by separating erosional and accretionary states on a plot of wave steepness versus Dean number. Similar agreement was found using the *average* deep-water significant wave height, $\bar{H}_o$ ($\bar{H}_o = 0.626 \cdot H_o$), and a slope of $M = 0.0007$, lending support to using wave height criteria as a determining factor of beach erosion or accretion tendency.

Based on their analysis, the additional criteria by which a beach state may be predicted with the deep-water significant wave height, H_o, are:

$$\begin{cases} \text{If } D_o < 2.4, \text{then ACCRETION is highly probable} \\ \text{If } D_o < 3.2, \text{then ACCRETION is probable} \\ \text{If } D_o \geq 3.2, \text{then EROSION is probable} \\ \text{If } D_o > 4.0, \text{then EROSION is highly probable} \end{cases} \tag{1.5}$$

and

$$\begin{cases} \text{If } \frac{S_o}{D_o^3} > 0.00054, \text{then ACCRETION is highly probable} \\ \text{If } \frac{S_o}{D_o^3} > 0.00027, \text{then ACCRETION is probable} \\ \text{If } \frac{S_o}{D_o^3} \leq 0.00027, \text{then EROSION is probable} \\ \text{If } \frac{S_o}{D_o^3} < 0.00014, \text{then EROSION is highly probable} \end{cases} \tag{1.6}$$

The Dean number criterion of predicting accretion or erosion suggested by *Kraus et al.* (1991) is in agreement with the criterion suggested by *Wright and Short* (1984), even though they computed the Dean number with different parameters. *Wright and Short* (1984) use the breaking wave height while *Kraus et al.* (1991) use the deep-water significant wave height (or deep water average significant wave height). For low Dean numbers and large wave steepness ($D_o < 2.4$, $S_o > 0.00054 D_o^3$), both models (*Wright and Short* (1984) and *Kraus et al.* (1991)) predict the beach to be accretionary. For large Dean numbers ($D_o > 4$, $S_o < 0.00014 D_o^3$) the beach state is predicted to be erosional. When Dean numbers fall between these extremes the beach is in one of several intermediate states following the descriptive model of *Wright and Short* (1984). It presumably can be in an erosional state or an accretionary state, depending on the existing wave conditions. The *Kraus et al.* (1991) model found similar ambiguity as the wave steepness and Dean number ranges approached the threshold separating erosion from accretion. Descriptive models need to be interpreted carefully when criteria are in this range. Using strictly the Dean number is reliable, however, incorporating the wave steepness into predictions may enhance reliability.

Empirical Beach Profile Evolution

Many empirical formulations have been suggested in attempts to model beach profile evolution in response to varying hydrodynamics. One such model, SBEACH [*Larson and Kraus* (1989)] uses existing offshore wave conditions (sediment fall velocity and wave steepness) to predict cross-shore profile evolution and shoreline change. The beach profile is separated into 4 distinct sections: a prebreaking zone, transition zone, broken-wave zone and swash zone. The sediment flux and transport rates are empirically derived based on data collected from large, near-prototype wave channels [*Larson and Kraus* (1989)].

Empirical evolution models are advantageous because they require little computation time. One disadvantage, however, is that the calibration coefficients encompass so many processes that they require site-specific calibrations [*Roelvink and Brøker* (1993)].

Another type of empirical model researchers have used to predict beach profile shape is the equilibrium beach profile model. *Bruun* (1954) derived an equation for average beach profile shapes based on the local sediment grain size:

$$h(y) = A(d) \cdot y^{2/3} \tag{1.7}$$

where h is the depth of the profile at a distance y offshore. The parameter $A(d)$ is a function of the median sediment diameter, d (mm). The value for A is determined from laboratory, field and empirical relationships based on sediment size and fall velocities [see Figure 7.6 in *Dean and Dalrymple* (2002)]. *Dean* (1977) later confirmed the equation formulation by analyzing over 500 beach profiles along the eastern and Gulf coasts of the United States. He found a range of values for the power which had a mean value near 0.66, in accordance with Bruun's value of $\frac{2}{3}$.

Process-Based Models

Process-based models attempt to predict profile evolution by incorporating all of the relevant physics into the model. These models have shown encouraging results for predicting specific aspects of beach change [*Thornton et al.* (1996); *Gallagher et al.* (1998)], yet no model has been presented, to date, that accounts for all forms of possible beach

morphology.

Perhaps the most well-known processed based models are those based on the energetics model of Bagnold [1966], though there are many others being used presently in the nearshore community. Bagnold's model for sediment transport in uniform stream flow was extended in the past decades to incorporate cross-shore oscillatory effects in nearshore breaking wave regions [*Bailard* (1981); *Bowen* (1980)]. The expansions of the model are examined in detail in section 3.

These models, like other sediment transport models, have their limitations, though. They have not predicted onshore sediment transport with the same consistency that they predict offshore transport [*Thornton et al.* (1996); *Gallagher et al.* (1998)]. Since the models rely on observed hydrodynamic measurements, the lack of understanding of the processes that transport sediment may be to blame. Until these processes that govern nearshore circulation and sediment transport are understood well, they will be limiting factors to the predictive capability of process-based nearshore models.

1.2 Beach Evolution Experiments

Over the last few decades, a small number of‘ field experiments have fortunately taken place during which comprehensive datasets of onshore and offshore bar migration were collected. In addition, several laboratory experiments with portions devoted to profile evolution have been conducted. Some relevant experiments are described below, but other datasets than those mentioned may exist.

1.2.1 Field Measurements

DUCK82

The DUCK82 experiment took place at the U.S. Army Corps of Engineers Field Research Facility (USACE FRF) site in Duck, North Carolina. Prior to this experiment, however, a significant onshore sandbar migration event was observed. During two three-month periods prior (February-May and May-August), the offshore, shore-parallel sandbar migrated shoreward nearly 100 meters [*Birkemeier* (1984); *Trowbridge and Young* (1989)].

Between February and May, 1982, the initial sandbar had a cross-shore distance of bar crest to shoreline, X_b, of 260 meters and a water depth over the bar crest of $h_b = 3.5$ meters. The bar crest migrated approximately 52 meters shoreward in 82 days. Between May and August, 1982, the initial sandbar crest was at a distance of $X_b = 208$ meters offshore and the water depth over the crest was $h_b = 3.2$ meters. The bar continued to migrate shoreward a distance of 33 meters in a period of 99 days. These values were computed from beach profile data during the respective time period.

The DUCK82 experiment actually took place during the month of October, 1982. Its purpose was to measure the nearshore morphological response to storm-induced waves and currents. In fact, along with offshore migrating beach response to energetic storm waves, further onshore bar migration was observed. During this time period onshore migration was observed at rates of up to 1-2 m/hr.

Onshore beach migration is commonly thought to occur when the crest of the sandbar falls outside of the surfzone, and steep, unbroken waves transport sediment shoreward. In agreement with this theory, *Trowbridge and Young* (1989) found the onshore beach migration prior to the DUCK82 experiment when the sandbar crest was well outside the surfzone, under the influence of unbroken waves. However, during the DUCK82 experiment in October, further onshore migration was observed even though the bar crest was within the region of breaking waves [*Birkemeier* (1984)], adding confusion to the theory that sandbars form at the dominant wave breaking location, at the offshore extent of the surfzone.

We analyzed the predicted beach states of the six-month onshore migration, based on the wave steepness and Dean number criteria of *Kraus et al.* (1991). Deep-water significant wave heights were 1.18 and 0.72 meters, respectively; wave periods were 8.5 and 8.6 seconds, respectively; sediment fall velocities were 0.025 m/s for each period. From these parameters, the Dean number and wave steepness parameter, $\frac{S_o}{D_o^3}$ (as *Kraus et al.* (1991) calculated), were 5.6 and 3.4, 6×10^{-4} and 1.6×10^{-4}, respectively.

Interestingly, the Dean number for the first 3-month period predicts a strongly erosive period, even though accretion was observed. The wave steepness parameter for the same case predicts a strongly accretive scenario, however, in accordance with the observations.

The Dean number and wave steepness parameter for the second 3-month period predict an erosive period, in contrast to observations. One explanation for the discrepancy between observed and predicted migrations might be that the wave height and period were averaged over a three-month time period, which clearly does not represent any short temporal (i.e. daily) variations in nearshore hydrodynamics that may have occurred.

DUCK94

The DUCK94 experiment took place at the FRF during the fall of 1994 (August - October). During the experiment, the bar migrated a net distance of approximately 150 meters offshore. For a five-day period in the month of September, however, onshore bar migration of 22 meters was observed. Immediately prior to the onshore migration, the sandbar was at a distance of $X_b = 112$ meters offshore of the shoreline with a water depth over the crest of $h_b = 2.1$ meters.

The bar migrated shoreward at approximately 0.5 m/hr [*Gallagher et al.* (1998)] during the five-day period. The deep-water significant wave height was approximately 0.80 meters, but varied to large (3.0 meters) heights periodically. The peak period was estimated at 10 seconds.

With these wave conditions, the Dean number, $D_o = 3.16$ and $\frac{S_o}{D_o^3} = 1.5 \times 10^{-4}$. the Dean number predicts the beach to be an an accretionary state, while the wave steepness parameter predicts the beach to be in an erosional state, in conflict with the observed accretionary state of the beach.

SW Washington State Study

A beach morphology monitoring program was initiated during the summer of 1997 along the Columbia River littoral cell (CRLC) in the Pacific Northwest. The monitoring program is part of a larger investigation with the objective to understand and predict the coastal behavior of the region so that managers may plan over temporal scales of decades and spatial scales of tens of kilometers [*Ruggiero et al.* (2005)].

El Niño and La Niña years have had highly destructive impacts on this area of coastline, causing severe erosion of sediment from the shoreface. However, in the three years

following the 1997/1998 La Niña event, the beaches in the area recovered, some experiencing net progradation [*Ruggiero et al.* (2005)].

Significant onshore bar migration was observed in an area immediately north of the Gray's Harbor jetty system, in Washington [*Ruggiero et al.* (2006)]. The period of comparison was between April and August, 2001. Significant onshore migration was observed (60 meters along one transect and 150 meters along another transect, spaced in the alongshore direction by several kilometers) during this time period. The initial cross-shore distance from shoreline to bar crest was $X_b = 550$ meters with a depth of water over crest of $h_b = 3.2$ meters.

The offshore significant wave height was 1.70 meters with a peak period of 8.9 seconds. Using these values, the Dean number was computed as a very large number, $D_o = 12.1$, and the wave steepness parameter at 1×10^{-5}. Both parameters predict strong erosional conditions, when accretion was actually observed in the field.

Of noteworthy importance is the physical differences in nearshore characteristics between the Washington State study and the Duck experiments on the East coast. In this region of the Pacific Northwest, the grain sizes are relatively smaller, leading to beach profiles with milder slopes than those at Duck, N.C. Additionally, the longshore influences of currents on sediment transport in this region of the West coast cannot be ruled out.

1.2.2 Laboratory Measurements

SUPERTANK - 1991

SUPERTANK was a multi-institutional collaborative laboratory research experiment at the O.H. Hinsdale Wave Research Laboratory at Oregon State University. The experimental phase took place in the Large Wave Flume (LWF) during August and September, 1991 (further detail about the LWF is provided in Section 2). The purpose of the experiment was to gather comprehensive datasets to quantitatively predict cross-shore hydrodynamics, sediment transport and beach change [*Kraus and Smith* (1994)].

A variety of wave conditions were involved, including a wave case devoted to beach

accretion. The accretionary wave test conditions consisted of wave heights varying between $H_{mo} = 0.4$-0.5 meters and wave period $T_p = 6$-10 seconds; small wave heights and long wave periods. Tests consisted of both random and monochromatic waves. The total duration of wave action was 870 minutes if only the random wave cases are considered (this amounted to 19 wave runs of varying lengths of time). During the test period the crest of the sandbar was observed to decrease in height and migrate shoreward on the order of several meters [*Kraus and Smith* (1994)], providing a dataset of controlled onshore bar migration.

LIP 11D - 1993

The Large Installation Plan (LIP) 11D experiment took place in the Delta Flume at Delft Hydraulics between April and June, 1993. The flume is 240 meters in length, 5 meters in width and 7 meters in depth. The objective of the study was to generate high quality and high resolution data of hydrodynamics and sediment transport dynamics on a natural beach under equilibrium, erosive and accretive conditions [*Roelvink and Reniers* (1995)].

Strongly accretive wave conditions occurred during test 1c, when $H_{mo} = 0.6$ meters and $T_p = 8$ seconds. Wave action proceeded for 13 hours. Over the duration of the accretive wave case, the crest of the sandbar migrated approximately 4-5 meters shoreward [fig 3.3.2 in *Roelvink and Reniers* (1995)]. This wave case, too, provided a comprehensive dataset encompassing onshore bar migration.

1.3 Research Focus

The focus of this report is two-fold: first, a recent sandbar migration study that took place as a part of a large-scale laboratory experiment (CROSSTEX - CROss Shore Sediment Transport EXperiment) will be discussed. Specifically, the experimental bar migration portion of CROSSTEX will be discussed in full detail. Second, two leading energetics total load sediment transport models will be described [*Bailard* (1981); *Drake and Calantoni* (2001); *Hoefel and Elgar* (2003)]. Their ability to predict bathymetric change using the hydrodynamic and bathymetric data collected during CROSSTEX will be assessed.

This thesis is organized as follows: section 2 will discuss a recent large-scale laboratory bar migration experiment (CROSSTEX) in full detail. The cross-shore sediment transport numerical modeling techniques and results will be described in Sections 3 and 4. Section 5 will dicuss model sensitivity to several factors. Conclusions from this analysis will be discussed in Section 6. The appendices contain additional relevant information from CROSSTEX and the modeling efforts described within this report (Appendices A - G).

2. CROSSTEX

2.1 Experiment Description

The CROSSTEX (CROss-Shore Sediment Transport EXperiment) project was a multi-institutional, collaborative laboratory research experiment that took place between June and September, 2005. The experiment was conducted in the Large Wave Flume (LWF) at the O. H. Hinsdale Wave Research Laboratory (HWRL) at Oregon State University (Figure 2.1). The LWF is 104 meters long, 3.7 meters wide and 4.6 meters deep, which permits most experiments to be performed at near prototype scale. (Figure 2.2). Beach sand from the Oregon coast was placed in the LWF to create a natural beach ($d_{50} = 0.22$ mm, see Appendix G for sediment size analysis).

The laboratory allowed for strict control over wave conditions. Moreover, alongshore variation of hydrodynamics were considered negligible due to the narrowness of the channel, allowing researchers to analyze one directional component of the hydrodynamics. Four major phases occurred during the time frame of the experiment (See Table 2.1).

Table 2.1: CROSSTEX Phases

Research Focus	Principal Investigators	Institution(s)	Exp. Dates
PIV & Sand Ripples	Foster/Stanton (FS)	Ohio State U.; NPS	6/6 - 7/17
Turbulence	Cox/Maddux (CM)	Oregon State U.	7/18 - 8/14
Bar Migration (BM)	Özkan-Haller/Kirby (OHK)	Oregon State U.; U. Del.	8/15 - 9/11
Swash Zone	Cowen/Liu (CL)	Cornell U.	9/12 - 9/30

The focus of the this report is the OHK experiments, which collected data in the nearshore region, including the region of breaking and non-breaking waves. One objective of the OHK portion of the experiment was to generate an extensive dataset of onshore and offshore sandbar migration that will be used to validate (or disprove) leading theories of cross-shore sediment transport. The wave cases during this portion are discussed in Section 2.5.

Fig. 2.1: Image of waves breaking in the LWF at the O. H. Hinsdale Wave Research Laboratory. The view is toward the wavemaker and waves are traveling toward the front left of the image. Image left and right is hereinafter referred to as East and West, respectively.

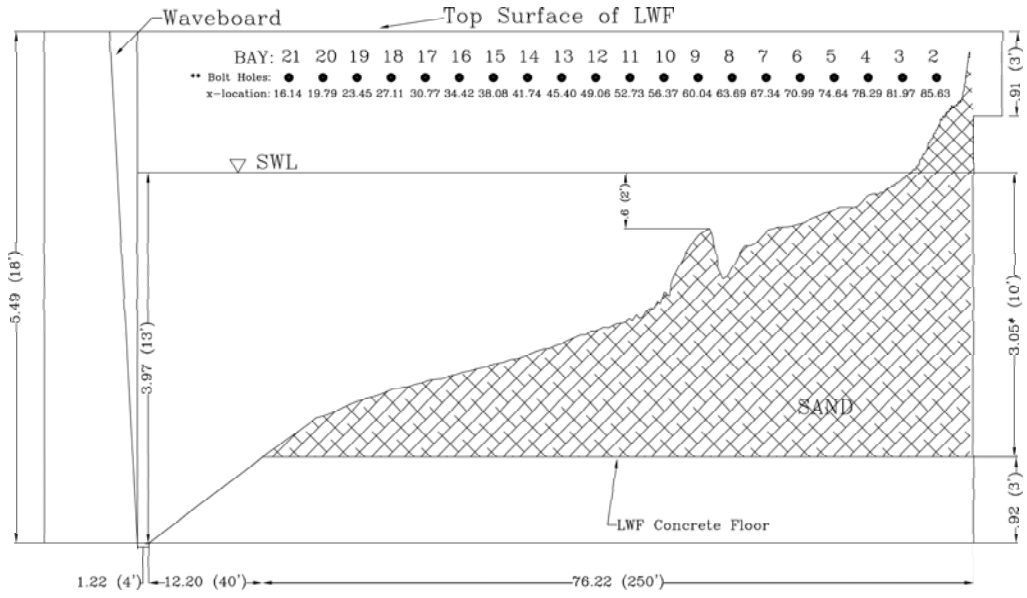

Fig. 2.2: Sectional Elevation of the LWF showing the location of the tank floor and typical water level and beach shape. *Note: Vertical scale is 10 times greater than horizontal scale.*

2.2 Experiment Scale

CROSSTEX experiment scale ratios were determined by comparing the cross-shore distance from the shoreline to the sandbar crest for field and laboratory datasets, X_b. The final cross-shore location of the sandbar crest for the offshore migration case and the initial cross-shore location for the onshore case are identical at X_b =21.5 meters. Assuming a representative field scale of X_b =200 meters, the length scale ratio of the offshore and first onshore bar migrations was approximately **1:9.3**.

Using the same representative field scale as above, the relative experimental scales of the CROSSTEX onshore migratory event, compared to the SUPERTANK and LIP 11D migratory events, are shown in Table 2.2.

Table 2.2: Recent laboratory experimental scales

Experiment	Year	Scale
SUPERTANK	1991	1:8.7
LIP 11D	1993	1:4.25
CROSSTEX	2005	1:9.3

2.3 Instruments Used

Acoustic Doppler Velocimeters (ADVs), Optical Backscatter Sensors (OBSs), Fiber-Optic Backscatter Sensors (FOBSs), Electromagnetic Current Meters (EMCMs) and Resistance-type wave gauges were deployed in both a cross-shore array and a vertical array in the LWF. Two types of velocimeters were used during the experiment: Nortek Cable Probe Vectrino Velocimeters (supplied by the HWRL) and side-looking Nortek (Rigid-Stem) Doppler Velocimeters (supplied by the University of Delaware). The OBSs used were D & A Instruments OBS-3 models [*D&A* (1991)]. The FOBSs were supplied by A. Ogston from the University of Washington. The EMCMs were supplied by T. Stanton of the Naval Postgraduate School.

The Nortek Vectrinos used for CROSSTEX were bistatic sonars. The sample volume is located approximately 5 cm from the beam axis (with a programmable sample volume height between 0.3 and 1.5 cm). In this case, the sample volume was 1 cm in height. The

instruments use separate transmitting and receiving beams; one transmitting beam and four receiving beams which convert the return signals into 3-component velocities (x, y and z directions) [*Nortek* (2004)].

Optical sensors, like OBSs and FOBSs, transmit and receive infrared light, measuring the amount of light that backscatters off of solids in the water. On the OBSs, a high intensity infrared emitting diode transmits the signal and 4 photodiodes detect the return beam. Their primary function is to measure turbidity and suspended sediment concentration (SSC) in the water column by detecting the infrared radiation scattered from the suspended matter [*D&A* (1991)].

The response of the turbidity meters depends strongly on the size, shape and composition of the suspended matter. Because of this, the instruments required calibration with suspended solids from the area of study to ensure the most accurate measurements. Details of our calibration procedure are provided in Appendix E.

The OBSs transmit infrared light at a wavelength of 875 nm. The effective range of measurable suspended solids is 2-100,000 mg/L, based on an estimated sand size of 200μm. The sample volume distance from the sensor is strongly dependent on the turbidity in front of the sensor. Higher concentrations of suspended matter in the water will decrease the distance that the infrared light can pierce the water column. Additionally, ambient light from adjacent surfaces can bias OBS measurements. Further detail of OBS sensitivity is provided in Appendix F.

2.3.1 Cross-Shore Array Deployment

The origin of the coordinate system in the LWF was located at the wave paddle, on top of the east wall of the tank. X is onshore positive, Y is positive to the west and Z is positive up, following a right-handed system. An important aspect to note is that the Bay numbers (Bays in 12' (3.65 m) increments) of the LWF are numbered sequentially from onshore to offshore (see Figure 2.2). See Appendix D for further detail about the LWF coordinate system and instrument deployment locations.

Twelve wave gauges remained fixed on the east wall of the flume for the duration of the experiment. They were arranged to sufficiently measure the water surface elevation

inside and outside of the anticipated surfzone region. Unequal horizontal spacings of wave gages outside of the breaking wave region provided the means to measure the wave reflection in the tank for waves of varying wavelengths.

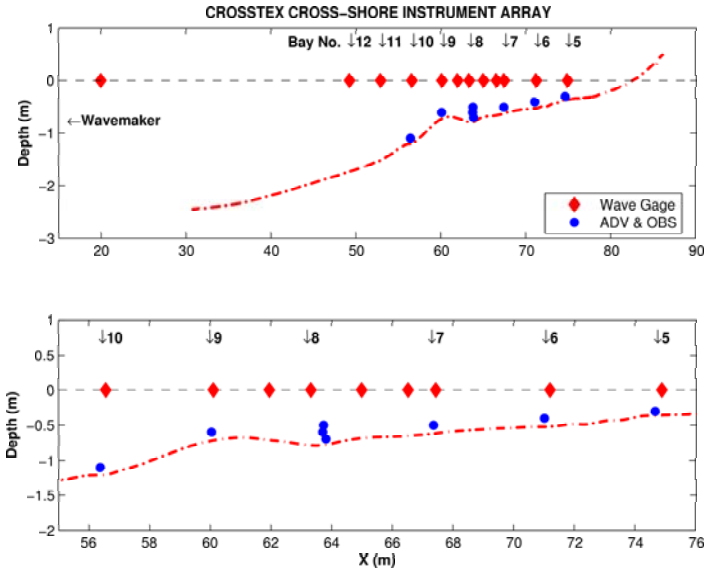

Fig. 2.3: (Top) Sample Bathymetric Survey showing x-shore locations of wall-mounted wave gauges (diamonds) and ADVs/OBSs (circles). (Bottom) Enlarged view of nearshore instrument array.

The cross-shore array of ADVs and OBSs measured the near-bottom water particle velocity and suspended sediment concentration (SSC), respectively. An instrument pair consisting of one Vectrino and one OBS was deployed at each offshore bolt hole location at Bays 5-10, excluding Bay 8 (at which 3 pairs of instruments were deployed). One-inch diameter coarse-threaded, round aluminum bars ("stingers") were machined to secure into the LWF bolt holes at each bay number. Each aluminum stinger was designed to support both a Vectrino and OBS in a near-bottom measuring manner (i.e. Vectrino probes facing the bed, OBS sensor facing the Vectrino sample volume). Figure 2.3 shows the locations of the cross-shore array of wave gauges, ADVs and OBSs.

At the Bay 8 bolt holes, a vertical arrangement of instruments was implemented on a thin steel plate that was mounted flush against the wall. One-inch diameter, coarse-threaded bolts were welded on the steel plate to provide a location to mount horizontal stingers. The plate was designed such that stingers could be raised or lowered easily to

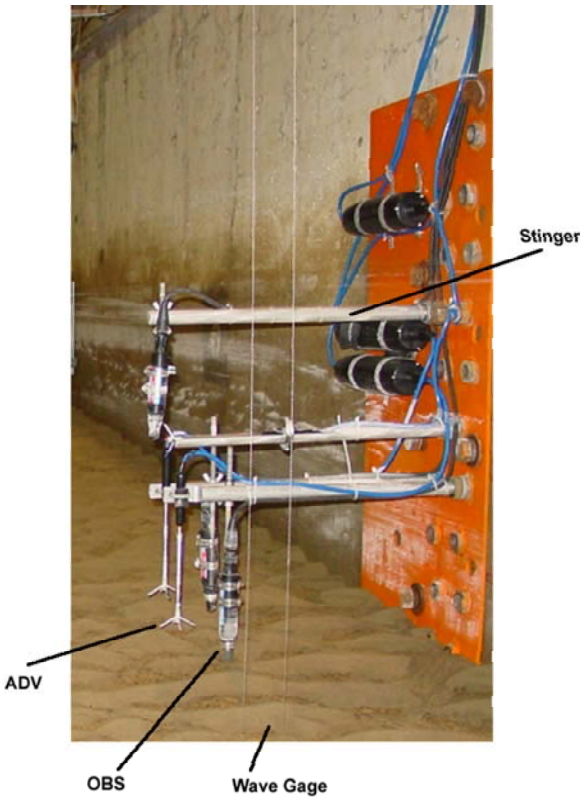

Fig. 2.4: Bay 8 near-bottom vertical array on wall plate. Each cable-probed Vectrino is paired with an OBS.

correspond to the vertical variation in sand level during the course of the experiment (Figure 2.4). Three pairs of Vectrinos and OBSs were mounted in a closely-spaced vertical array to measure the velocity and SSC at several near-bottom elevations. Two Vectrinos sampled near-bottom locations with their probes facing the bed. Each had a corresponding OBS deployed in proximity. The final ADV/OBS pair consisted of a side-looking Vectrino and a diagonally looking OBS (top of Figure 2.4).

A difficult aspect of any field or laboratory research experiment is attempting to measure both velocity and SSC at the same spatial location, without causing flow disturbance due to the instruments. Since it is virtually impossible to sample in a particular location without having any adverse effects on the flow characteristics, the objective was to sample in proximity to other instruments while *minimizing* flow disturbance.

The sample volume of the ADVs was programmed to be 1 cm in height. The sample

volume of the OBSs, however, depended on the turbidity of the solution. Increasing turbidity decreases the separation distance between the OBS sensor and sample volume. Because of the strong attenuation of infrared light in water, the sample volume will never be further than 20-25 cm from the OBS sensor in clear water [*D&A* (1991)]. This was also verified by "hand-waving" tests in clear water (e.g. waving a finger in front of the sensor).

A distance of 7.5 cm was chosen to represent the sensor-to-sample-volume distance of the OBSs. This was in enough proximity to the ADV sample volume to still sample in the same vicinity reliably, yet, at enough distance to avoid flow disturbance around the velocimeter. All but one cross-shore mounted OBS was oriented to face an ADV in the positive alongshore direction.

The highest OBS mounted on the wall plate at Bay 8 was oriented in a diagonal fashion (pointing at an ADV at a 45^o angle). We assumed the inherent variability in any OBS measurement overshadowed any errors that might surmount from orienting an OBSs in this manner.

2.3.2 Carriage Array Deployment

The carriage array of instruments included 4 Nortek Vectrinos, 4 NDVs, 4 Electromagnetic Current Meters (EMCMs), 7 OBSs and a set of 20 FOBSs. An additional (13th) wave gauge was mounted on the mobile carriage to measure the water surface elevation at the cross-shore location of the carriage instruments. Excluding the wave gauge, the instruments were mounted off of a vertically mobile aluminum frame, which allowed precise vertical positioning of the instruments. Three "wings" shaped like airfoils, in order to minimize water disturbance, were mounted on this frame (See Figures 2.5 and 2.6). Instruments and housings were bolted to the frames or mounted with hose clamps. Housings and cables were then wrapped in plumbing tape to further minimize water disturbance due to the bulky equipment housings.

Instruments were arranged in a vertical array, staggered in the along-shore and cross-shore directions. Alongshore deployment of the instruments was spread across a majority of the width of the LWF channel. On the other hand, the largest spacing of carriage

Fig. 2.5: View of the 3 "airfoil" wings on the mobile carriage with instruments mounted in a cross-shore and along-shore staggering vertical array. Left to Right: Wing 1, 2 and 3.

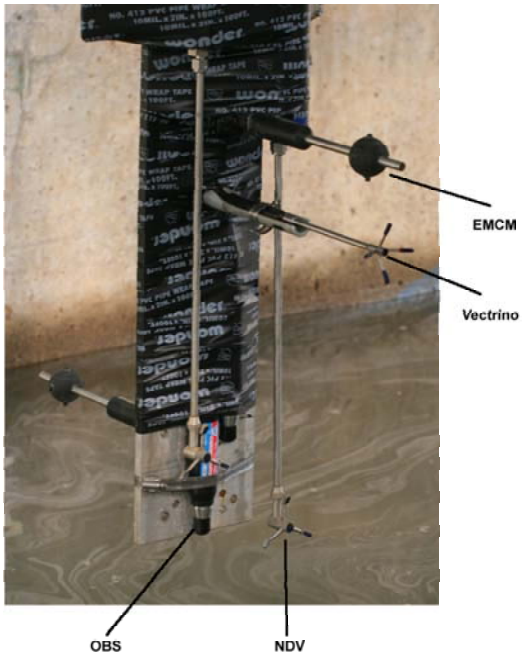

Fig. 2.6: Enlarged view of one of the "airfoil" wings showing several instruments arranged in a vertical array. From left to right: EMCM, NDV, OBS, NDV, EMCM, Vectrino (side-looking).

instruments in the cross-shore direction was on the order of $\mathbf{O}(20\text{ cm})$.

The FOBS were mounted lowest in the array; on the center wing of the carriage (Wing #2). The vertical elevations of the remaining OBSs and ADVs were designed such that the lowest FOBS probe was inserted 1 cm into the sand bed prior to the start of each wave case. This aligned the lowest ADV sample volume at an elevation of 1 cm above the bed.

Each OBS was paired with at least one ADV (NDV or Vectrino). Some redundant mounting of instruments occurred, as well, to test repeatability of the instrument measurements. For instance, 2 NDVs, 1 Vectrino and 2 OBSs were mounted at the same elevation ($h = 15$ cm above the bed), spaced in the alongshore direction. This provided repeatability tests between the 2 NDVs, between the NDVs and the Vectrino, and between the 2 OBSs. The OBS elevations also corresponded to the same elevation as a FOBS sensor, allowing comparison of SSC measurements between the two optical instruments. Additionally, there was correlation between the elevation of the EMCM's and the ADVs at certain elevations, though a comparison between measurements is not discussed in this report.

FOBS

The FOBS were a system of 2 probes (upper and lower), each of which contained 10 fiber optic sensors (Figure 2.7).

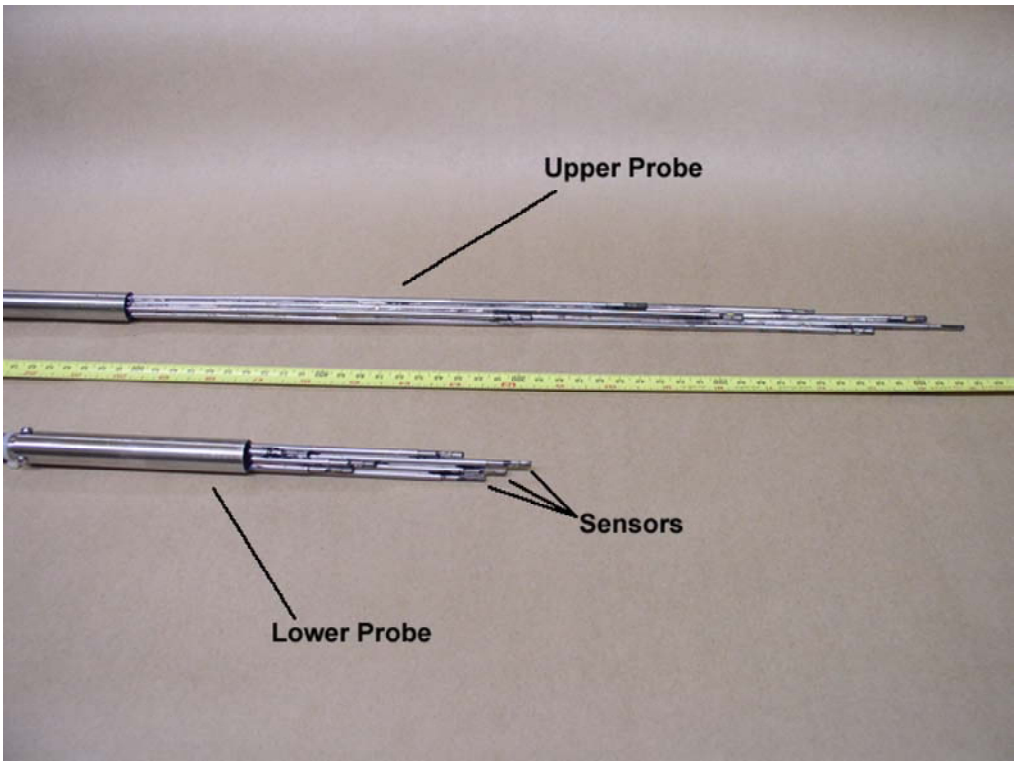

Fig. 2.7: Image of upper and lower probe from FOBS system. Each probe consisted of 10 sensors.

2.4 Data Collection

Data from the 15 OBSs, 12 Vectrinos and 13 wave gauges were recorded with two (Master and Slave) National Instruments PXI-Data Acquisition (DAQ) Systems (supplied by the Hinsdale Wave Research Laboratory (HWRL)). Additional data-logging PC's from the NPS, University of Delaware and the HWRL were used to record the data from the 4 EMCMs, 4 NDVs and set of 20 FOBS sensors, respectively. Time synchronization was obtained through an internet time pulse and controlled by the Master DAQ. The master DAQ collected data for all cross-shore instruments mounted on the LWF wall. The slave DAQ recorded data from the ADVS and OBSs mounted on the carriage. The

NDVs also were synchronized by the same system, but were logged on a separate PC. The FOBSs were synchronized to the wavemaker board displacement signal, but were not post-synchronized for this report. The EMCMs were not synchronized with any of the other instruments. The EMCM data collection, however, always encompassed the entire duration of wave action. Presumably, they can be post-synchronized as well, but were not for this report.

2.4.1 Hydrodynamic Data

The data collection procedure began with the startup of the EMCMs so that their data records encompassed all periods of data collection. The NDVs and Slave DAQ were initialized and waited for a trigger pulse from the Master DAQ. Then, the Master DAQ was started (also triggering the Slave DAQ and the NDV data collection). The FOBS data collection began manually after this, having an arbitrary start sometime prior to the start of wave action. FOBS data collection was concluded manually following the cessation of waves.

A typical wave run consisted of 20 minutes of data collection: approximately 1 minute of still water time, 15 minutes of wave action and approximately 4 minutes of tank seiching (settling) time. The DAQ systems recorded data for the entire 20 minutes. The first minute of data collection provided a baseline of the still water mean voltages for all the instruments. The final 4 minutes of data collection can be used for future studies of seiching modes in the LWF.

The DAQ systems allowed a range of -5 to +5 volts to be recorded from the instruments. For the wave gauges, this was not of concern because the zero means can be reset at anytime. Any effects of the arbitrarily chosen zero mean for the wave gauges are eliminated during the reduction of wave data (See Section 2.6.1).

The OBSs, however, do not allow the selection of a zero mean. Furthermore, they have the ability to record voltages larger than + 5 Volts. Any voltage greater than + 5 Volts would be cut off ("clipped") by the DAQ system, and recorded at the DAQ limit, + 5 Volts. The limitation on recordable voltages by the DAQ severely restricted

the range of measurable voltages, and thus SSC. This makes interpretation of the time series' difficult and may not be fully representative of the SSC in the sample volume of the OBS. To ameliorate this limitation, the options were:

1. Lower the gain settings on the OBSs to make them less sensitive to backscatter.
2. Divide the incoming voltage in half before the DAQ records the data, effectively allowing for a 10 Volt range of data to be recorded (0 to +5 Volts on the DAQ).
3. Subtract 5 Volts from the incoming signal before the DAQ records the data, which also allows for a full 10 volts to be recorded (-5 to +5 Volts on the DAQ).

A 5 Volt offset (Option 3) was selected for the experiment because it allowed for full, unaltered resolution of the incoming OBS voltages (just offset by 5 Volts). A voltage offset box (built by L. Fayler) was inserted inline between the OBSs and DAQs. This manner of recording OBS voltages was used throughout the OHK experimental phase, and during the post-calibration of the OBSs following the completion of the CROSSTEX experiment (Appendix E).

2.4.2 Bathymetric Survey Data

Bathymetric surveys were typically conducted following each wave run. If the bathymetry changed a very small amount between wave runs, however, then bathymetric surveys were conducted less frequently (every 2 or 4 wave runs). This was a subjective decision on part of the researchers, but was made in order to increase the attainable duration of wave action on the beach profile. Surveys typically occurred less frequently during onshore bar migration cases, when sediment transport occurred at slower rates.

When conducted, there were two segments to the surveys (Figure 2.8):

1. Acoustic sonar survey with the SeaTek Multiple Transducer Array (MTA) system mounted on the gray carriage.
2. A manual survey (with a survey rod) of the nearshore and swash regions where the water depth was too shallow to complete a sonar survey.

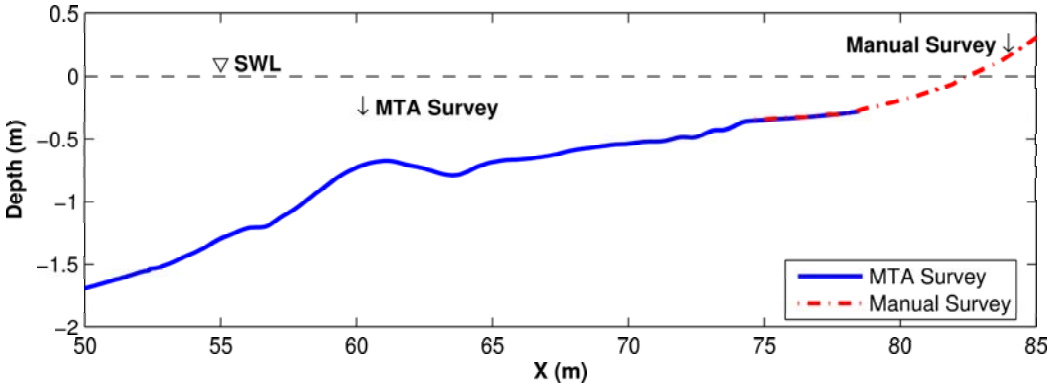

Fig. 2.8: MTA and manual bathymetric surveys and overlap region.

MTA Surveys

The MTA consisted of 32 transducers flush-mounted in a flat, horizontal aluminum bar. The array was mounted to the mobile gray carriage so that frequent, cross-shore bathymetric surveys were easily obtained.

An MTA survey was typically initiated in 20 cm of water and traveled offshore to a depth of at least 150 cm. The rate of motion was controlled on the gray carriage, and remained sufficiently slow to minimize erroneous acoustic returns.

The MTA was mounted offshore of the wing array on the cart. The cross-shore distance between the MTA centerline and offshore edge of the wing array was $X = 46.75$ cm. Cross-shore positions of the carriage instruments are presented relative to the offshore edge of the wing in Appendix D.

The vertical position of the MTA was **1.292** meters below the top of the LWF wall. This was 7 cm below the SWL of the LWF (which was **1.219** meters below the top of the LWF wall).

The cross-shore position of the carriage and instruments in the LWF coordinate system was measured with a laser mounted on the carriage. The laser pinged off of a white-colored target located on the south wall of the HWRL. The distance was sampled at 1Hz, corresponding to the same sampling rate of the MTA. The laser was calibrated by C. Scott and L. Fayler and the zero offset of the wave paddle from the laser target was surveyed (with a Total Station) by J. Killian. The surveyed distance from the wave

paddle to the target on the south wall was 9.42 meters. All cross-shore distances recorded in bathymetric survey files will need this distance subtracted in order to place the surveys in the horizontal LWF coordinate system. Additional details are provided in the headers of the survey files.

Manual Surveys

A manual survey typically began in water depths of 30-40 cm and traveled onshore (in 30 cm increments) to a dry beach area beyond the location of furthest wave runup. A survey rod was placed vertically against a second LWF gray carriage. Depth readings were taken relative to the top of a horizontal beam on the carriage and backed out into LWF coordinates after the survey. The top of the horizontal beam was $14\frac{9}{16}$ in. (37 cm) above the top of the LWF wall. Subtracting this value from the depths in the files converts the hand surveys into the LWF vertical coordinate system. In order to get measurements into the LWF horizontal coordinate system, the x-coordinates need to have 70.99 meters added to their values since this was the offshore starting point of the manual surveys. Further detail about the hand surveys may be found in the file headers.

The overlap region of the MTA and hand surveys was sampled to ensure accurate concatenation of the two surveys into a full beach survey. The accuracy of the two methods was verified by comparing the measurements in the area of overlap. Any errors become immediately evident during this direct comparison. Over the course of the experiment a consistent 1 cm vertical offset was observed between the hand surveys and the MTA surveys. The cause of this discrepancy was not determined exactly, but can be attributed to a several things, including human measurement error and MTA deviation from horizontal.

2.4.3 File Structure

The Master DAQ recorded data from the 12 wave gauges and 8 OBSs that were mounted on the LWF wall. Additionally, each file contains a record of the voltage standard, water temperature, wave board displacement and water surface elevation measured at the wave board. The Slave DAQ recorded data from the 13^{th} wave gauge and 7 OBSs mounted

on the gray carriage. The master and slave DAQ file headers describe the contents of each file in more detail. Data in the DAQ files were output as voltages. The calibration coefficients for the wave gauges are listed in the header information at the top of each DAQ file. The calibrations for the OBSs are discussed in Appendix E.

The data from all of the Vectrinos (wall- and cart-mounted) were recorded in 12 individual files corresponding to each velocimeter. Each file contained columns for an error flag, X-, Y- and two Z-velocities (in m/s), 4 amplitude columns (corresponding to each directional beam), 4 signal-to-noise ratio (SNR) columns, and 4 correlation (CORR) columns (each corresponding to a directional beam). SNR is a measure of the strength of the return signal to the ambient noise.

The data from the 4 NDVs were recorded in one file for each wave run. The raw files are in binary format. The reduced NDV data provides directional velocities in ASCII format (see next section for additional detail).

Data from all 20 FOBS sensors was recorded in one file for each wave run. The FOBS output was in digital units (bits) and required calibration to convert into dimensional units. The calibration coefficients for the FOBS are found in Appendix E.

2.4.4 File Nomenclature

Raw Data Files

DAQ. The naming convention of the *raw* DAQ files (both Master and Slave) contained the yearday day and the decimal time of day followed by the denotation of the representative DAQ. For example:

$$235.8157\_analog\_master.txt$$

where *235* is the yearday, *8157* represents a decimal time of the day (in UTC) and *_analog_master.txt* denotes the Master DAQ file.

ADVs. The naming convention of the *RAW* ADV files appears in a similar fashion:

$$236.7841\_cart\_adv00\_com3.txt$$

or

$$236.7845\_wall\_adv02\_com5.txt$$

where the yearday and decimal time are denoted as above, the location of the ADV is specified (cart or wall), and additional ADV information is provided. The final two terms in the filename can be used to determine the port number of the respective ADV. For instance, the cart ADV file listed above is located in Port 1 (add 1 to the *adv* number or subtract 2 from the *com* number). The Wall ADV is located in Port 3 (found in the same manner). The port information discloses the DAQ port reference number to which the instrument was connected. It is pertinent information when determining the proper ADV and location (See Appendix D.2).

Surveys, NDVs, FOBS. The RAW MTA and hand survey, NDV and FOBS filenames were also recorded as a combination of time and date:

$$\textbf{\textit{file}}\_082405\_1000.txt$$

where ***file*** denotes the type of file ('survey', 'hand_survey', 'ndv' or 'fobs'), 082405 is in the form $mm/dd/yy$ and 1000 denotes the time of day in 24-hr format. The raw survey file contains the data from all 32 MTA transducers. The hand_survey files contain the cross-shore location and depths measured at the centerline of the LWF. The NDV files contain data from all 4 NDVs in one binary file. The FOBS files contain raw data from each of the 20 FOBS sensors.

Reduced Data Files

ADVs. RAW ADV files were passed through a phase-space de-spiking routine of *Goring and Nikora* (2002) (by G. Guannel) and re-saved under different file names:

$$0823R06\_VelWallADV1.txt$$

where 0823 denotes the month and day, R06 denotes the Run number, and VelWallADV1.txt denotes the velocity file from the wall ADV in Port 1.

This data reduction condensed the multicolumn Vectrino files into a 3 columnar format (X-, Y- and Z-direction velocities). Furthermore, it simplified the identification of the ADV and its cross-shore location.

NDVs. The binary NDV data were converted into ASCII format by P. Terán (University of Delaware). The processed filenames have the format:

$$V\_ndv\_082305\_1235.vu$$

where the date and time that the file was created is denoted by 082305 (mm/dd/yy) and 1235 (24 hr time), respectively. The reduced NDV data is arranged in 12 columns, 3 columns for each NDV (x-, y- and z-directions). Each 3-column group (e.g. columns 1-3, 4-6, etc.) corresponds to NDVs N356 N379, N357 and N377, respectively.

2.5 Wave Case Description

The four-week OHK experiment was separated into four cases of wave conditions and transport directions. Each case consisted of varying numbers of wave runs (Cases A, B, C and D). The wave conditions along with target wave heights and wave periods are shown in Table 2.3.

A wave run consisted of 15 minutes of wave action. The number of wave runs completed during each case varied, though, typically, wave conditions were held constant until the profile change slowed to a negligible amount. For certain runs, data files were not correctly written to the DAQ, thus the discrepancies between the existing data files and the total duration of wave action. Each wave case is described below.

Table 2.3: OHK Wave Cases

Case	*Description*	Target H_o (m)	Target T_p (sec)	Existing Wave Files	Existing ADV Files	Total Wave Dur. (min)
A	Offshore Sandbar Migration	0.60	4.0	14	14	210
B	Onshore Sandbar Migration I	0.32-0.35	8.0	38	39	660
C	Variable Sandbar Migration	0.32-0.5	3.5,5.5	34	34	510
D	Onshore Sandbar Migration II	0.175-0.25	3.5	51	50	765

2.5.1 Case A: Offshore Sandbar Migration

Beginning from a small amplitude barred beach shape, the beach profile rapidly changed into a storm-bar profile under wave action. The waves were designed to replicate storm waves: large wave heights and short wave periods. Figure 2.9 displays the initial and the final beach profiles from this case.

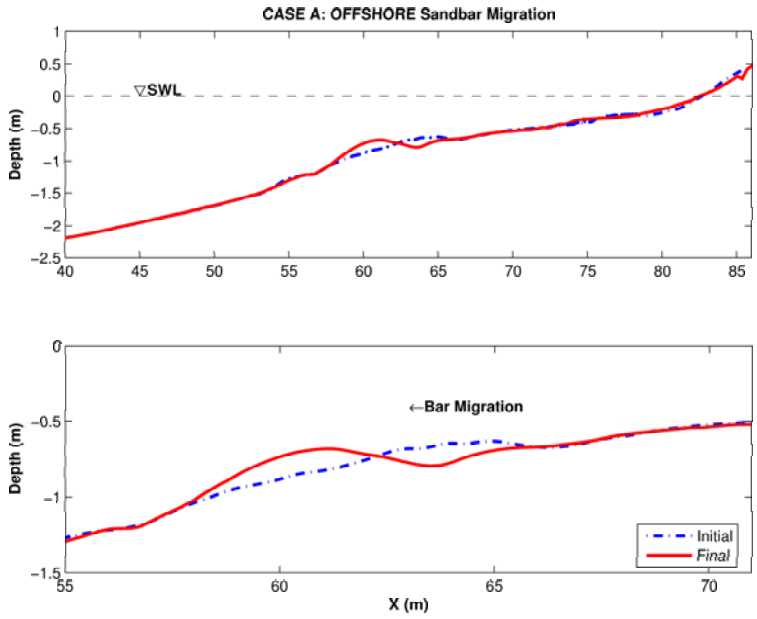

Fig. 2.9: (Top) Initial (dashed) and Final (solid) profiles for Case A, displaying offshore sand migration and sandbar formation. (Bottom) Enlargement of offshore sandbar migration. For the remainder of this paper, all plots will show the SWL as Z = 0.

2.5.2 Case B: Onshore Sandbar Migration

The wave conditions were altered to resemble milder wave action during post-storm recovery. The wave heights were decreased and the wave period was increased. During this case, the sandbar began to flatten, filling in the onshore trough. A second sandbar formed shoreward of the bar-trough as a result of wave-breaking at this more shoreward position. Figure 2.10 displays the initial and final beach profiles from this case. *Note: At the end of Case B, the beach was highly reflective. Therefore, prior to beginning Case C, the beach foreshore slope was altered to create a milder slope.*

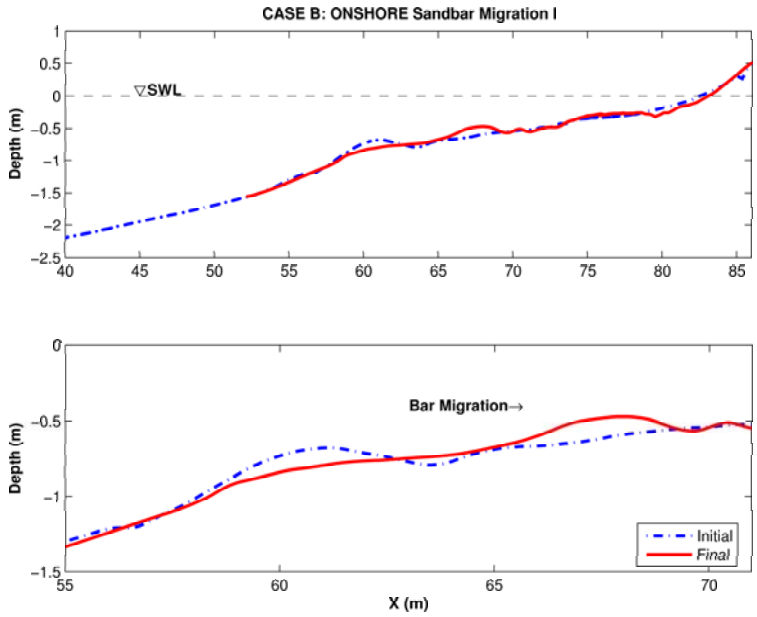

Fig. 2.10: (Top) Initial (dashed) and Final (solid) profiles for Case B, displaying onshore sand migration and sandbar formation. (Bottom) Enlargement of onshore sandbar migration.

2.5.3 Case C: Minor Sandbar Migration

At the beginning of this case, there was a mild, offshore sandbar and a pronounced, onshore sandbar; a result of the Case B wave conditions. An attempt was made to move the onshore sandbar towards the offshore again, with the final objective then to drive the sandbar shoreward. However, after altering the wave conditions several times, the sandbar did not move a great distance and remained relatively stable. This case was, therefore, used to observe the effects varying wave conditions had on a stable profile. The changes to the beach profile were minor during this period. Further analysis of this particular wave case will not be performed in this report. Figure 2.11 shows the initial and final beach profiles for this case, and the minor changes in profile shape that resulted. Note that the offshore bar continued to move shoreward during this time.

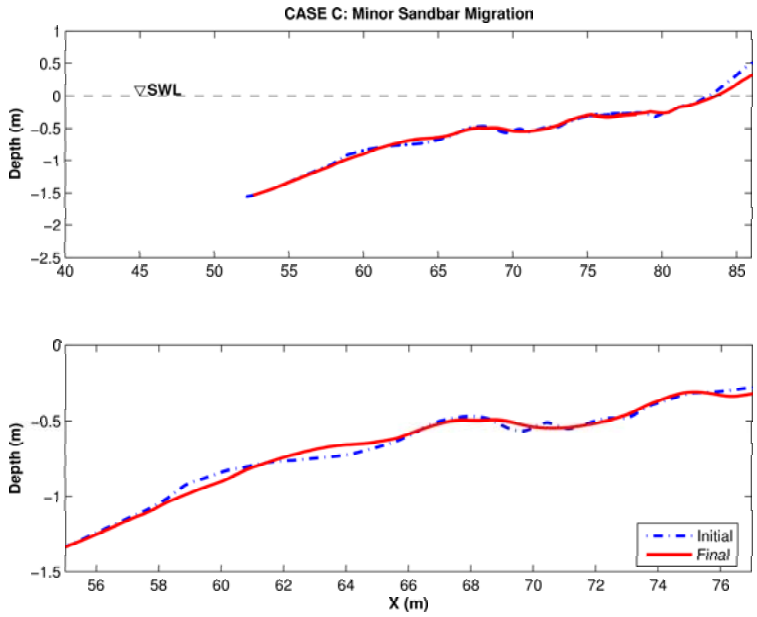

Fig. 2.11: (Top) Initial (dashed) and Final (solid) profiles for Case C, displaying variable sand migration and sandbar formation. (Bottom) Enlargement of sandbar migration.

2.5.4 Case D: Onshore Sandbar Migration

The objective of Case D was to force the existing sandbar onshore as far as possible. The effects of the wave conditions on the profile shape were monitored after each wave case. They were then altered accordingly, to ensure continuous onshore migration of the sandbar. The results of this case was the translation of a barred profile to a nearly monotonic beach. Figure 2.12 provides examples of the initial and final beach profile shape from this onshore migration case.

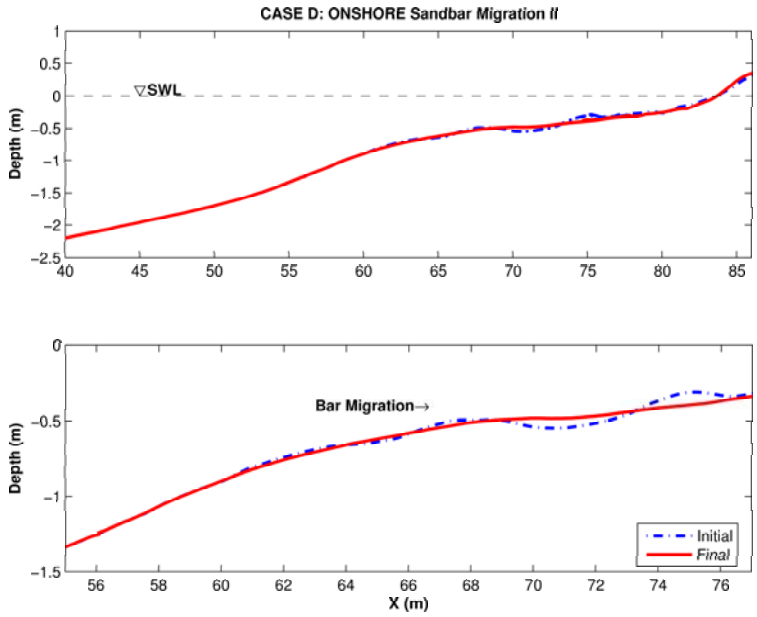

Fig. 2.12: (Top) Initial (dashed) and Final (solid) profiles for Case D, displaying onshore sand migration and sandbar formation. (Bottom) Enlargement of onshore sandbar migration.

2.6 Hydrodynamic Data Reduction

2.6.1 Water Surface Elevation Analysis

Wave gauge data were recorded (in volts) on the Master DAQ (for wave gauges 1-12) and the Slave DAQ (wave gauge 13). Calibration coefficients from the wave gauge calibrations provide conversions into water surface elevation. The calibration coefficients for wave gauges 1-12 are listed in the Master DAQ file headers. The calibration coefficient for wave gauge 13 is 0.1055 $\frac{m}{V}$. *(Note: DAQ headers for data collected prior to August 31, 2005 provide calibration coefficients in English units. DAQ headers from August 31, 2005 to the end of the experiment list the metric calibration coefficient conversion, in accordance with the units used throughout the experiment.)*

The DAQs sampled wave gauge data for 20 minutes at a sampling rate of 50 Hz, for a total of 60,000 data points collected during each wave run. The following procedure was used to analyze the wave data:

1. wave gauge voltages were converted into water surface elevation (meters).
2. A mean elevation from a section of still water data prior to wave action was computed (data points [1:1500]) and subtracted from the entire wave gauge time series, removing the still water mean from the time series.
3. A section of waves was selected from the period of wave action (data points [10000:42767] = approximately 11 minutes of wave action) for each wave gauge. The following wave statistics were obtained:
   - Mean water level (MWL)
   - Wave Asymmetry
   - Wave Skewness
4. A spectral analysis yieided:
   - Frequency Power Spectral Density
   - H_{mo}
   - Peak Period, T_p

The MWL was computed simply as the mean of the water surface elevation over the selected data points. The wave asymmetry was computed as

$$asym = \frac{\langle H(\eta^3)\rangle}{\langle \eta^2\rangle^{3/2}} \tag{2.1}$$

where H denotes Hilbert Transformation, and the wave skewness as

$$skew = \frac{\langle \eta^3\rangle}{\langle \eta^2\rangle^{3/2}}, \tag{2.2}$$

where η in both equations denotes the de-meaned water surface elevation time series [following *Kennedy et al.* (2000)].

Using the data range specified above, a time series with $n = 32,768 = 2^{15}$ number of points was analyzed, a number which is conducive to efficient Fast Fourier Transforming (FFT). The data were multiplied by a Kaiser window prior to FFT-ing. It was bandpass filtered ($fmin$ and $fmax$ were determined from a spectral analysis, over the expected range of wind and swell waves). A Bartlett averaging scheme was applied using 8 windows of 4096 points each. The *average* power spectral density (PSD) was computed from the PSD from each windowed time series.

The upper and lower cutoff frequencies, f_{min} and f_{max} were determined by examining

the average PSD from each wave case. The high-pass cutoff frequencies were chosen to include the paddle-generated frequencies, but not the low-frequency seiching. Since the low frequency energy significantly increased towards the shore, high-pass cutoff frequencies were selected from the PSD of wave gauge 12 for each wave condition. The high-pass frequencies were between 0.1 and 0.2 Hz, depending on where the energy in the low frequency signal began to increase for each wave case. The low-pass cutoff frequency for all wave cases was chosen as 10 Hz, a frequency at which the power was five orders of magnitude less than the peak energy.

The rms wave heights, H_{rms}, were computed from the zero-order moment of the spectrum over the bandpass frequencies as

$$H_{rms} = \sqrt{8 \cdot m_o} \tag{2.3}$$

where

$$m_o = \int_{fmin}^{fmax} \bar{S_f} \cdot df, \tag{2.4}$$

and $\bar{S_f}$ corresponds to the average PSD of the eight Bartlett blocks from each analyzed time series. The peak period, T_p, was obtained from the frequency carrying the highest energy within the spectral bandwidth under analysis.

2.6.2 Wave Statistical Analysis

Figures 2.13 and 2.14 present the frequency PSD (for wave gages 1 and 12) and the cross-shore varying wave statistics, respectively. Table 2.4 provides the cross-shore varying statistics in tabular form for wave case A. Similar plots for the remaining CROSSTEX wave cases are presented in Appendix A.

Note that lower frequencies were dominant frequencies at the shallowest wave gauges, showing the potential influence of low-frequency motions (seiching) on the hydrodynamic data.

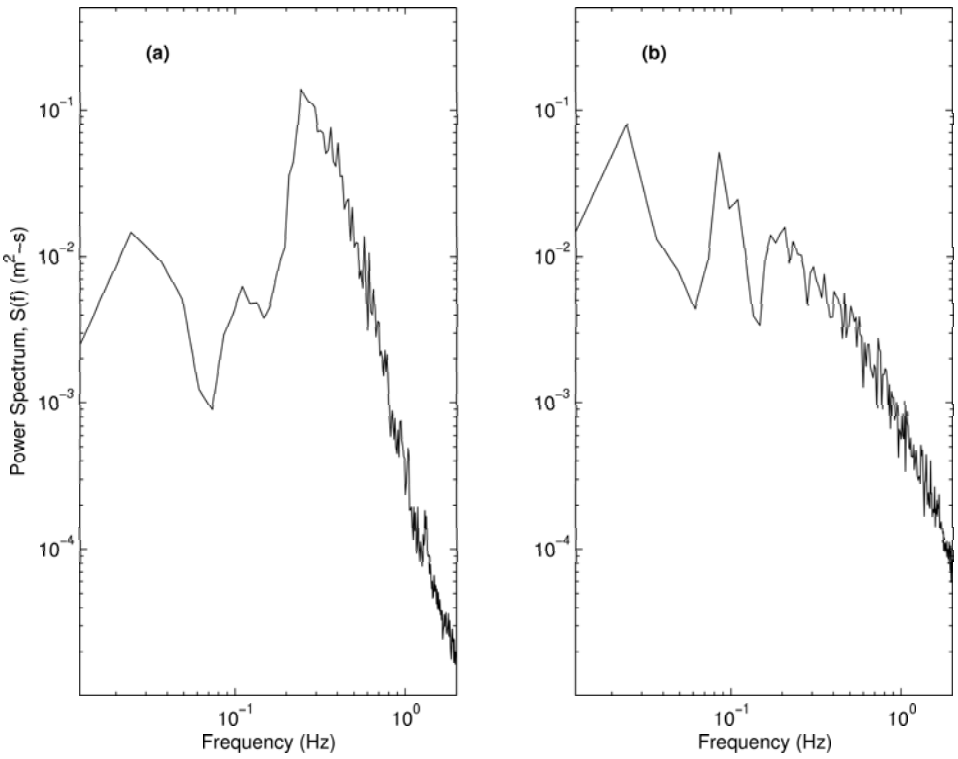

Fig. 2.13: Wave case A: *offshore* bar migration (a) Wave spectra from wave gauge 1 (Bay 20), (b) Wave spectra from wave gauge 12 (Bay 5).

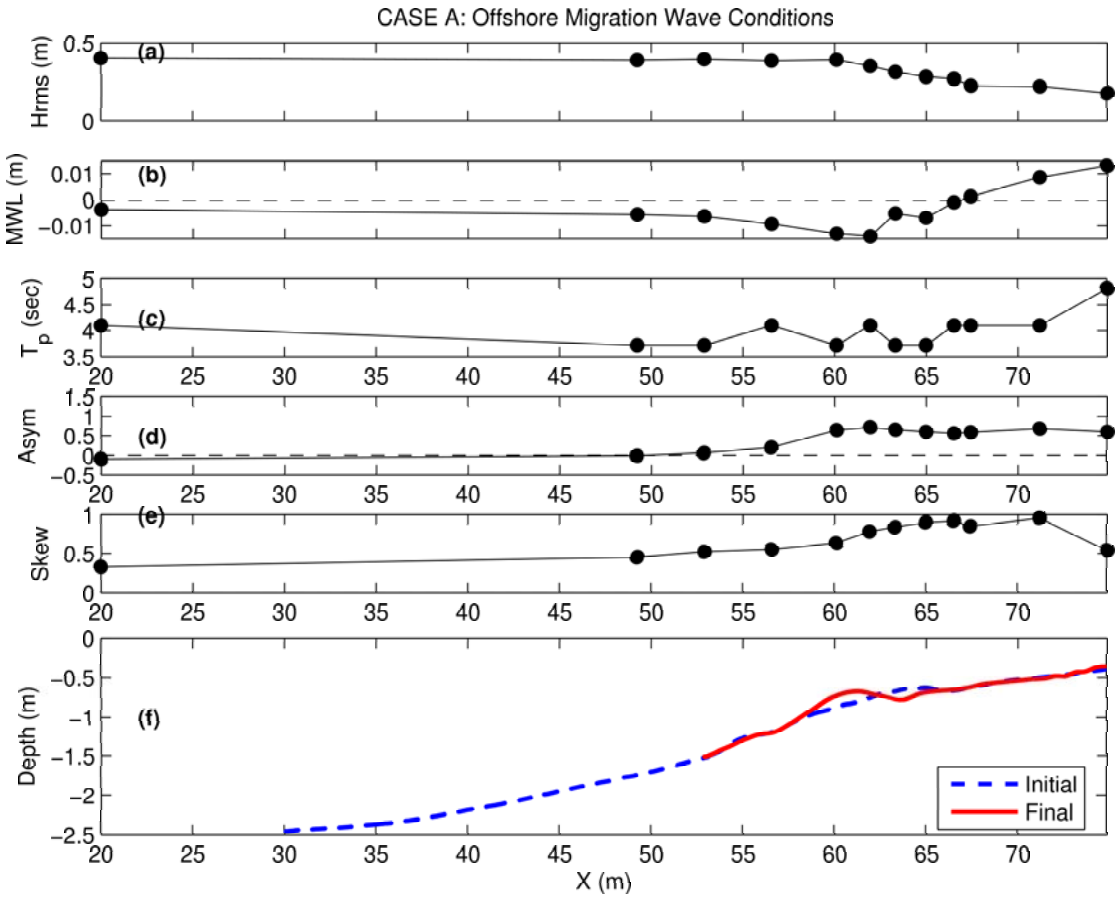

Fig. 2.14: Wave case A: *offshore* bar migration (a) H_{rms}, (b) mean water level, (c) peak period, (d) wave asymmetry and (e) wave skewness vs. cross-shore location averaged over all CASE A wave runs. (f) initial and final bathymetries.

Table 2.4: CASE A Wave Statistics

	WG 1	WG 2	WG 3	WG 4	WG 5	WG 6
Hrms (m)	0.40	0.39	0.40	0.39	0.39	0.35
MWL (m)	-0.004	-0.006	-0.006	-0.009	-0.013	-0.014
Tp (sec)	4.10	3.72	3.72	4.10	3.72	4.10
Asym	-0.09	-0.01	0.06	0.20	0.64	0.72
Skew	0.33	0.45	0.52	0.55	0.63	0.79

	WG 7	WG 8	WG 9	WG 10	WG 11	WG 12
Hrms (m)	0.31	0.28	0.27	0.23	0.22	0.18
MWL (m)	-0.005	-0.007	-0.001	0.001	0.009	0.013
Tp (sec)	3.72	3.72	4.10	4.10	4.10	4.82
Asym	0.65	0.60	0.56	0.59	0.68	0.60
Skew	0.84	0.90	0.92	0.85	0.96	0.54

Dean Number Migration Prediction

The Dean number, $D_o = \frac{H_o}{wT}$, and wave steepness, $S_o = \frac{H_o}{L_o}$, have often been used as predictors of sediment erosion or accretion based on the deep-water incident wave conditions. In this thesis, the term wave steepness parameter refers to the wave steepness divided by the cube of the Dean number. Based on the criteria discussed in section 1.1, the following values for D_o and $\frac{So}{D_o^3}$ were calculated for the CROSSTEX wave conditions:

Table 2.5: Dean number and wave steepness parameter

Wave Case	Do	Prediction	$\frac{So}{D_o^3}$	Prediction
A	4.77	Strongly Erosive	2.8×10^{-5}	Erosion Highly Probable
B	0.91	Strongly Accretive	3.5×10^{-4}	Accretion Probable
C*	1.92	Strongly Accretive	1.7×10^{-4}	Erosion Highly Probable
D	1.99	Strongly Accretive	1.8×10^{-4}	Erosion Probable

* Wave Case C actually consisted of 2 different wave periods

In wave case A, the offshore migration case, both the Dean number and the wave steepness parameter predict erosive conditions, in accordance with observations. Wave case B, the first onshore migration case, the Dean number and wave steepness parameter predicts accretion, also in accordance with the observations.

Wave case C contained wave records of two wave periods, but because no further analysis was done with it in this report, is analyzed as one wave case. The Dean number and wave steepness parameter predict conflicting beach states: The Dean number predicts accretion while the wave steepness parameter predicts erosion. The can be due to the fact that the Dean number and wave steepness were computed for varying wave periods and heights during this period.

Finally, wave case D was an onshore migration case. The Dean number predicts strongly accretive wave conditions. However the wave steepness parameter predicts a strongly erosive condition, in contrast to the observations.

2.6.3 Velocity Data Analysis

The raw ADV data typically contained noise when the amount of particles in the water column was not sufficient to backscatter the acoustic signal. This was problematic towards the beginning of wave records, and continued into the data record until sufficient flow was attained. Much of the noise at the beginning of data files was avoided during analysis by selecting a time period to in which a wave signal was known to exist at all cross-shore locations [e.g. data points 10000:42767].

Additionally, noise in data files was attributed to situations in which the probes were measuring within a scour hole, buried in the bed or measuring at the same elevation as the bed. If this occurred, there was not sufficient flow to measure velocity.

Each (20 minute, 60,000 point) ADV data file was passed through two pre-filtering routines to replace obvious erroneous data points. The first filter was a correlation and SNR threshold filter. If a data point had a correlation value < 70 % and a SNR < 15 dB, then the data point was flagged for further analysis. Indices of flagged data points were saved in a separate file to be accessed later.

Then, the raw data files were passed though a phase-space filtering program [*Goring and Nikora* (2002)]. This method assumed: (1) that differentiation enhances the high frequency portion of a signal (a local acceleration filter of sorts), (2) that the expected maximum of a random series is given by the universal threshold, and (3) that good data cluster in a dense cloud in phase space or Poincaré maps. The definitions of universal threshold and Poincaré maps are given in *Goring and Nikora* (2002). If the data point failed any of these conditions, then it, too, was flagged for further analysis. Flagged data points from both the CORR/SNR and phase-space filters were replaced through interpolation with a cubic spline interpolation routine.

During filtering, the following new files were created:

- Filtered ADV data files (cubic interpolation over noisy data)
- Flagged Files (*filename format* $= 0825R02\_SpikeyADV1$)
  - Saved the indices of the flagged data points

- 0825 denotes the month and day
- R02 denotes the CROSSTEX run number
- This file was used to further analyze the number of flagged data points to determine if the number of points was acceptable or if the file was too noisy to use.

Additional filtering techniques and creation of databases for modeling purposes are discussed later in Section 3.4.

3. NUMERICAL MODELS

The hydrodynamic and bathymetric data collected during CROSSTEX was used to compare two commonly used cross-shore sediment transport models. Near-bottom velocities from Vectrino's mounted on both the LWF wall and the mobile carriage were first used to compute predicted sediment flux using the classical energetics total load model [*Bagnold* (1966); *Bowen* (1980); *Bailard* (1981)]. Subsequently, the same near-bottom velocities were used to drive an empirical extension to the energetics model, based on an acceleration descriptor term [*Drake and Calantoni* (2001); *Hoefel and Elgar* (2003)]. Hereinafter, the classical energetics model will be referred to as the energetics model (EM) and the empirical extension as the acceleration-based model (AM). The results of each model applied with the CROSSTEX data are discussed in Section 4.

3.1 Classical Energetics Model

The classical formulation of the energetics-type total load sediment transport model was originally derived for unidirectional stream flow in an open channel [*Bagnold* (1963); *Bagnold* (1966)]. Bagnold derived a relation between the energy expended by the fluid stream and the resultant sediment transport:

$$i = i_b + i_s = \left(\frac{\varepsilon_b}{tan\phi - tan\beta} + \frac{\varepsilon_s(1-\varepsilon_b)}{\frac{W}{\bar{u}} - tan\beta}\right)\omega \tag{3.1}$$

[formulation used in *Gallagher et al.* (1998)]

where i is the total immersed weight sediment transport rate, i_b is the contribution from the bedload, i_s is the contribution from the suspended load, ω is the stream power, $\bar{u}$ is the mean flow velocity, β is the slope of the bed, ϕ is the internal friction angle of the sediment and W is the suspended sediment fall velocity. ε_b and ε_s are the efficiency parameters of the bed load and suspended load, respectively.

ε_b = bedload work rate / stream power

ε_s = suspension work rate / stream power

[*Bagnold* (1966)]

The limiting angle of repose, $tan\phi$, is the maximum angle at which the cohesionless sediments will remain stable without "avalanching" down the slope. For most sands, this angle is approximately 33^o, which makes $tan\phi = 0.63$ [*Bagnold* (1966)].

The dissipated stream energy, ω, is proportional to some order of friction due to shear stress at the bed:

$$\omega = \tau\bar{u} = \rho_w C_f |\bar{u}|^3 \tag{3.2}$$

[*Gallagher et al.* (1998)]

where ρ_w is the density of water and C_f is a friction coefficient.

Bowen (1980) and *Bailard* (1981) extended Bagnold's steady flow model to include the effects of oscillatory motion on onshore and offshore sediment transport in the nearshore. This model was derived to include the effects of non-linearity in the surfzone. If the beach slope is small, the time-averaged, cross-shore volumetric sediment transport rate per unit width per unit time can be written as:

$$Q_x = K_b\{\langle|\vec{u}|^2\bar{u}\rangle + \langle|\vec{u}|^2\tilde{u}\rangle - \frac{tan\beta}{tan\phi}\langle|\vec{u}|^3\rangle\} + K_s\{\langle|\vec{u}|^3\bar{u}\rangle + \langle|\vec{u}|^3\tilde{u}\rangle - \frac{\varepsilon_s}{W}tan\beta\langle|\vec{u}|^5\rangle\} \tag{3.3}$$

where $\tan\beta$ is the local beach slope in the cross-shore and $\vec{u}$ is the total near-bottom velocity vector (cross-shore and alongshore), assumed by the models to exist immediately above the wave bottom-boundary layer:

$$|\vec{u}(t)| = \sqrt{u^2 + v^2} \tag{3.4}$$

and the directional velocities consist of a mean and time-varying oscillatory component:

$$u = \bar{u} + \tilde{u} \tag{3.5a}$$

$$v = \bar{v} + \tilde{v}. \tag{3.5b}$$

$\bar{u}$ is the mean component of the velocity and $\tilde{u}$ is the oscillatory component of the velocity. Angled brackets denote time-averaging [*Gallagher et al.* (1998)].

The dimensional coefficients, K_b and K_s are given by:

$$K_b = \frac{\rho_w}{g(\rho_s - \rho_w)} C_f \frac{\varepsilon_b}{tan\phi} \tag{3.6a}$$

$$K_s = \frac{\rho_w}{g(\rho_s - \rho_w)} C_f \frac{\varepsilon_s}{W}, \tag{3.6b}$$

where g is gravitational acceleration and ρ_s is the density of the sediment.

Since the equation for sediment flux, Q_x, depends on the vector of the near-bottom velocity, both the cross-shore and alongshore components contribute to the calculated sediment flux. However, to simplify computations, it is customary to assume that there are no longshore gradients in the sediment flux, so only cross-shore gradients need to be considered. Therefore, mass conservation for the model yields:

$$\frac{dh}{dt} = \frac{1}{\mu} \frac{dQ_x}{dx} \tag{3.7}$$

where h is the bed elevation and μ is a sediment packing factor [*Thornton et al.* (1996)], a measure of the porosity of the sediment.

3.2 Acceleration-Based Model

The classical energetics model has predicted offshore sediment transport reasonably well in the field, but failed to predict onshore sediment transport [*Thornton et al.* (1996); *Gallagher et al.* (1998)]. This caused researchers to suggest new model formulations. *Elgar et al.* (2001) suggested that onshore sandbar migration under mild wave conditions may be related to asymmetric orbital velocities and skewed fluid accelerations associated with the orbital velocities of nonlinear, unbroken waves. Large accelerations occur under the steep, front face of nonlinear unbroken waves, while milder accelerations occur under the rear face of these waves. Sediment is rapidly accelerated shoreward under the wave fronts but decelerates at a slower rate under the rear faces, potentially allowing sediment to settle out of suspension before it can be carried offshore. *Hoefel and Elgar* (2003)

defined the difference in magnitudes of acceleration under the front and rear faces of waves as acceleration skewness.

Drake and Calantoni (2001) used monochromatic wave computer simulations and comparisons to a recent laboratory tunnel bed-load experiment to derive a purely empirical sediment transport model. The formulation included an acceleration descriptor threshold that, if exceeded, initiated additional sediment transport, to improve onshore sediment migration prediction. The model excluded the effects of mean currents on suspended sediments, solely considering transport by bed-load. The equation they derived was:

$$\langle Q_x \rangle = \begin{cases} k\langle u^3 \rangle + K_a(a_{spike} - a_{crit}), & a_{spike} \geq a_{acrit} \\ k\langle u^3 \rangle, & a_{spike} < a_{acrit} \end{cases} \tag{3.8}$$

where a dimensional descriptor of acceleration skewness is

$$a_{spike} = \frac{\langle a^3 \rangle}{\langle a^2 \rangle}, \tag{3.9}$$

a is the magnitude of the acceleration, K_a and k are constants and a_{crit} is a critical threshold of a_{spike} that, if exceeded, will enhance the sediment flux at that location. *Drake and Calantoni* (2001) solved for values for their free parameters by comparing their computer simulations to the experimental results they describe. The best-fit free parameter values they found were $K_a = 0.07kg \cdot s/m^2$, $a_{crit} = 1m/s^2$ and $k = 0.8kg \cdot s^2/m^4$. The median sediment size used in the laboratory experiment and in the model simulations was $d_{50} = 1.1mm$. Their model is entirely empirical.

Hoefel and Elgar (2003) suggested a slightly different approach to modeling onshore transport, extending the classical energetics model to include fluid acceleration effects. Their model utilized the same energetics model formulation for the sediment flux, Q_x (Equation 3.3), but can add additional sediment flux, as the *Drake and Calantoni* (2001) model, to enhance the flux if the fluid descriptor, a_{spike}, exceeds a critical threshold. The

equation they derived is of the form

$$Q_x = Q_x + Q_{acc} \tag{3.10}$$

where

$$\langle Q_{acc} \rangle = \begin{cases} K_a(a_{spike} - sgn[a_{spike}]a_{crit}) & \text{if } |a_{spike}| \geq a_{acrit} \\ 0 & \text{if } |a_{spike}| < a_{acrit}, \end{cases} \tag{3.11}$$

a_{spike}, K_a and a_{crit} are defined as above, and *sgn* denotes the sign of a_{spike}. This model reverts to the classical energetics model if the acceleration descriptor does not exceed the critical value, a_{crit}. The values of the free parameters in this model differ from the one of *Drake and Calantoni* (2001) since this model is not entirely empirical, but, rather, process-based with an empirical extension. *Hoefel and Elgar* (2003) found best-fit parameter values (tuning to the DUCK94 beach profile data) to be $a_{crit} = 0.2m/s^2$ and $K_a = 1.4 \times 10^{-4} m \cdot s$.

The acceleration-based model follows the same remaining procedure as the energetics model of computing the resultant bathymetric change: sediment flux gradients and the corresponding bed elevation change are computed, and mass is still conserved in the system.

3.3 Model Parameters Used in this Study

Following *Bagnold* (1966), *Thornton et al.* (1996), *Gallagher et al.* (1998) (and references therein), the bedload and suspended load efficiency factors chosen were 0.135 and 0.015, respectively; the packing factor chosen as $\mu = 0.7$. For the steep beach slope constraint we used the value suggested above, $tan\phi = 0.63$ [*Bagnold* (1966)].

A coefficient of friction value of $C_f = 0.003$ has typically been used for previous sediment transport modeling efforts [*Thornton et al.* (1996); *Gallagher et al.* (1998), following *Church and Thornton* (1993)], though it is accepted that the coefficient of friction may vary from 0.001 to 0.006 [*Drake and Calantoni* (2001)]. Model sensitivity to C_f is discussed in Section 5.1.2.

The density of water and sediment was 1000 kg/m^3 and 2650 kg/m^3, respectively,

assuming natural quartz beach sand.

The values of K_a and a_{crit} were chosen based on a best-fit analysis by minimizing the mean squared errors between the model beach profile evolution predictions and observations. The best-fit values to the CROSSTEX data are discussed in Section 4.3.

3.4 Model Setup

3.4.1 Survey Databases

Only wave runs in which ADV files existed were used for modeling in this report. A wave run in which an ADV file was missing was skipped to the next sequential wave run for which an ADV file existed. The survey databases are tabulated in Appendix C.

3.4.2 ADV Databases

During the offshore migration wave case (Case A), the majority of ADV data files contained clean wave signals. During the first onshore migration (Case B), however, there was significant noise infiltration for various reasons, including, but not limited to, possible instrument burial in the sediment. The noise had the potential to bias sediment transport results, so it was important to determine which data files were usable.

Plots of the ADV elevations above the bed over time are presented below (Figures 3.1 and 3.2). During the onshore migration, the sudden increase in elevation of the ADV at bay 7 at run number 40 occurred because the ADV was buried and was raised manually. This change was made when the ADV probe was discovered to reside very near the bed elevation.

From these two figures, it is apparent that the ADV sample volumes potentially were below the bed elevation during several of the runs. However, it is not known if the probes were buried, if the sample volumes were measuring below the bed elevation, or if the sample volumes were measuring velocity within a scour hole. The instruments were mounted on the LWF wall, a location not surveyed by the MTA. Potentially, the bed elevation near the wall (at the instrument locations) differed from that measured by the MTA in the centerline of the LWF. Therefore, it is difficult to ascertain if the instruments

were buried or at sufficient elevation above the bed, even from these plots. However, the plots provide some insight as to the proximity of the instrument sample volumes to the surrounding bathymetry.

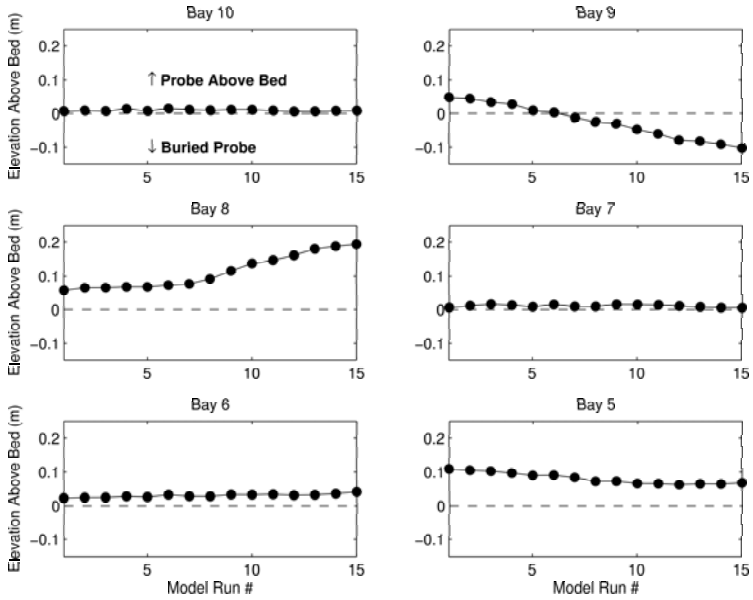

Fig. 3.1: *Offshore* migration case: ADV elevations above the bed vs. run number. ADVs are numbered bays 10-5, left to right, top to bottom.

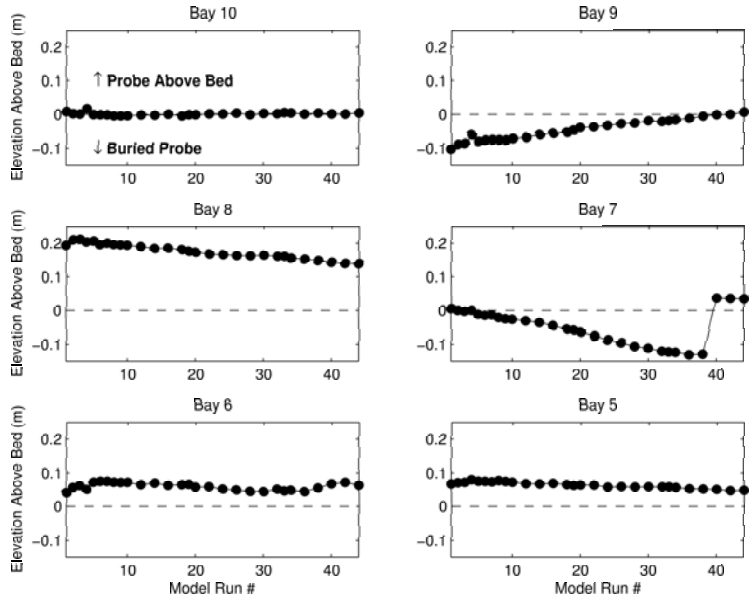

Fig. 3.2: *Onshore* migration case: ADV elevations above the bed vs. run number. ADVs are numbered bays 10-5, left to right, top to bottom.

Since the noisy data points ("outliers") were flagged during the pre-filtering routines, we analyzed the ratio of number of outliers to the total number of data points to determine a threshold at which data files would be considered too noisy. The same period of record was used for analysis as in other analysis routines (e.g. data points (10000:42767)). Flagged data points within this time period were the only points considered. The ratio of these flagged points to the total number of points in this range, $2^{15} = 32768$, was computed. Unfortunately, this analysis proved not to be a conclusive measure of separating clean and noisy data files.

Part of the problem was that many visually appealing (clean) velocity time series existed in which a large number of outlying data points had been removed by the pre-filtering (high ratio of noisy data points to total number of points). This might be explained by assuming that the pre-filtering interpolation routines successfully removed outlying data points and interpolated the wave signal reasonably well. However, the second part of the problem was that a large number of visually unappealing (noisy) time series existed in which a low number of data points were flagged by the pre-filtering routine (low ratio of noisy data points to total data points).

The largest percentage of flagged data points associated with visually appealing time series was approximately 7%, with large percentages (5%-7%) occurring frequently. Conversely, there were extremely unappealing (noisy) time series in which very low percentages of outlying data points were flagged. Often, the percentage was less than 1%. Therefore, separating noisy data files from clean data files was not possible with a simple threshold of a noisy outlier percentage. A more subjective approach was required.

Upon further examination, it was determined that a majority of the noisy looking data files suffered from a condition in which the erroneous data points were offset from the underlying wave signal by a specific magnitude. The reason for this was not discovered. It did not appear to be noise infiltration, however, since the wave signal was still visible in the noise, just offset by a certain magnitude. An example of a time series that suffered from this condition is shown in Figure 3.3.

In an attempt to alleviate this problem, all of the data files that were to be used to model sediment transport were passed through an additional acceleration filter. This was

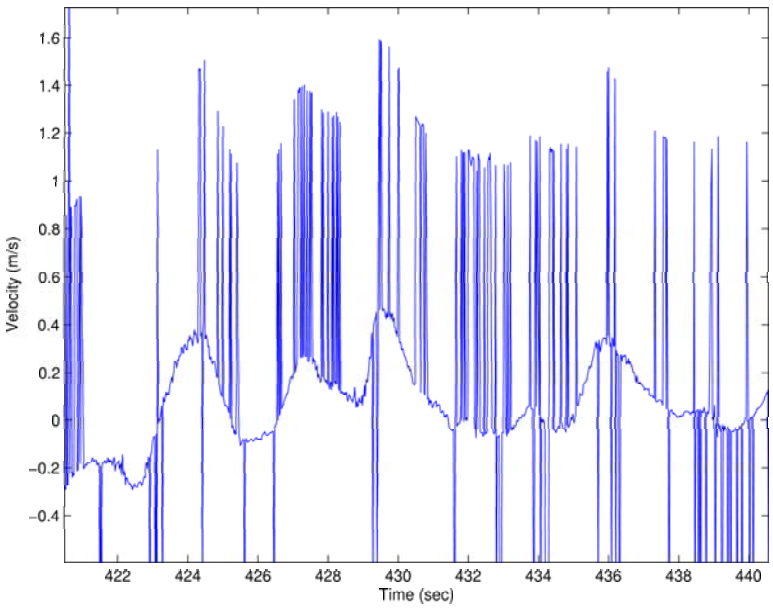

Fig. 3.3: Segment of a time series that suffered from noisy data points offset from the wave signal by a specific magnitude.

a local acceleration calculation, $\frac{du}{dt}$, between sequential data points. If the acceleration exceeded 3 g's (3 gravitational units of acceleration), then a cubic spline interpolation was applied across the outlying points. The acceleration threshold was set arbitrarily, but was deemed a conservative threshold that would filter out obvious erroneous data points.

If the original time series was clean, this filter would have no effect. However, it served to filter out many of the erroneous data points in the extremely noisy data files.

An example of the benefits of the additional acceleration filter is shown in Figure 3.4. The original time series is shown as a dashed line. The filtered time series is shown as a solid line.

The acceleration filter helped create cleaner wave signals in a few of the time series, but often not to a sufficient amount. A majority of all the data records still appeared noisy, which can be explained in two ways:

1. The threshold by which data points were deemed noisy was too large in magnitude. It would need to be decreased in order for the local accelerations to be large enough to flag the data for interpolation.

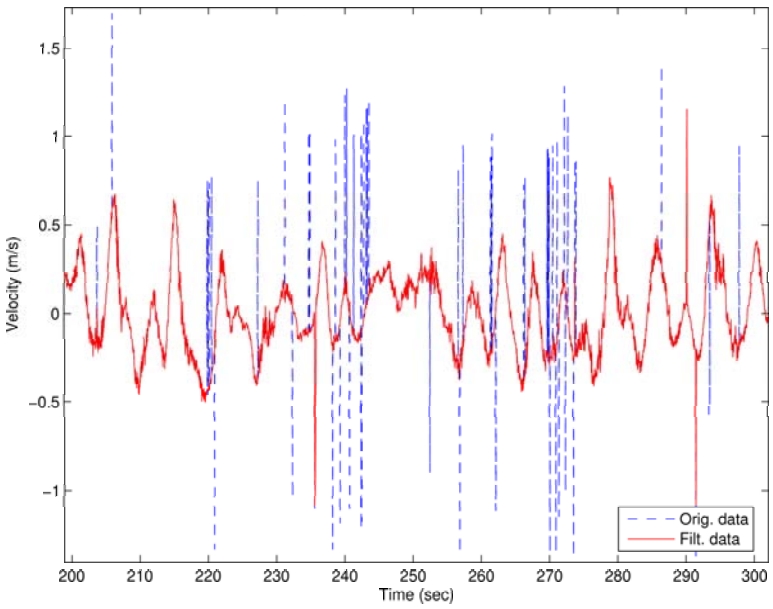

Fig. 3.4: 100 seconds of a time series that contains several noisy data "spikes" (dash). The filtered time series is shown as a solid line.

2. Too many noisy data points existed consecutively. Even though the filter may have flagged many data points within a noisy portion of the record, it may not have interpolated across all of them. Thus, the post-filtered time series still appeared noisy.

After the additional acceleration filter, time series were re-examined and noisy records were selected subjectively. Time series that contained a large number of noisy data points were marked for replacement. Fortunately, nearly all of the ADV data files for the *offshore* migration case had clean records. The data files during the *onshore* migration case required additional examination, however. Examples of clean and noisy time series, as selected subjectively, are presented in Figures 3.5 and 3.6. The time series are from two different wave runs and two different cross-shore locations. However, many more noisy data "spikes" exist in the noisy time series than the clean time series. The wave signal is evident in both figures.

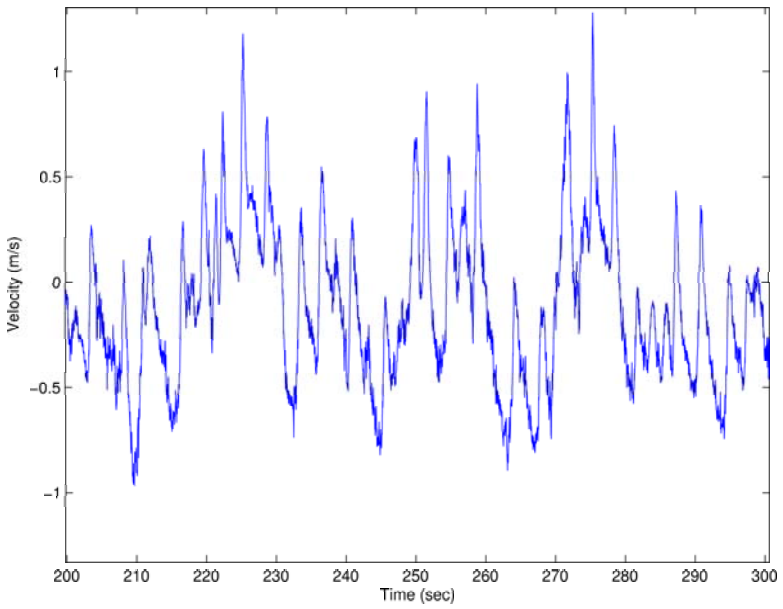

Fig. 3.5: 100 second sample of a clean time series as defined in this report.

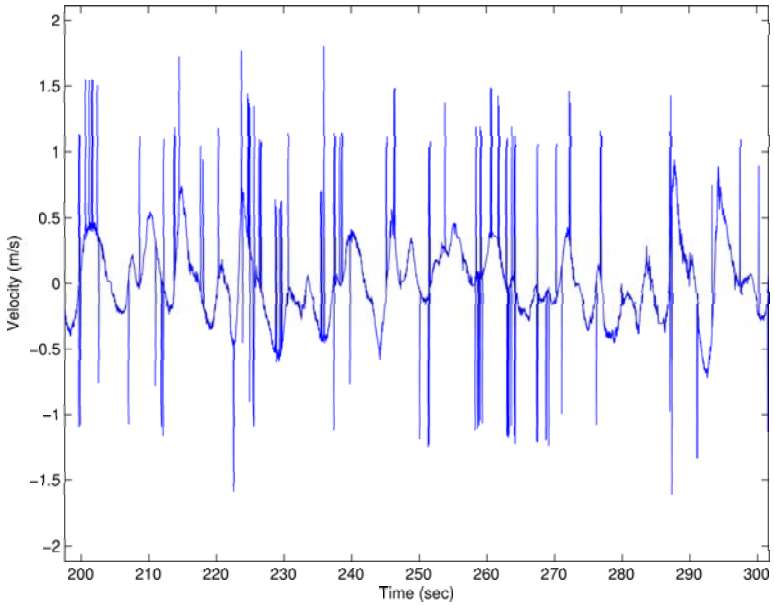

Fig. 3.6: 100 seconds of a time series that contains several noisy data "spikes".

In order to select the replacement files, it was first necessary to determine if the hydrodynamics varied greatly over the course of the onshore bar migration. This was done by analyzing certain parameters of each of the files to determine if adjacent (in time) clean data files could be substituted in place of subject data files. Specifically, the

mean cross-shore velocities and predicted sediment fluxes (Q_x) were analyzed.

ADV files were first subjectively flagged as "clean" or "suspect" through a visual analysis of the velocity time series. The relevant parameters from the *original* sequential list of velocity files were plotted, noting the parameters that corresponded to the clean and noisy dataset. It was apparent immediately that many of the subject data file parameters behaved differently from those of the the non-noisy files (Figures 3.7 and 3.8). By analyzing the clean dataset parameters adjacent to the subject dataset points, it also was apparent that the adjacent files were suitable replacements because they had similar (in magnitude) mean flow rates and predicted sediment fluxes. The following figures display the results from the *onshore* migration analysis. Plots from the *offshore* migration analysis can be seen in Appendix B.

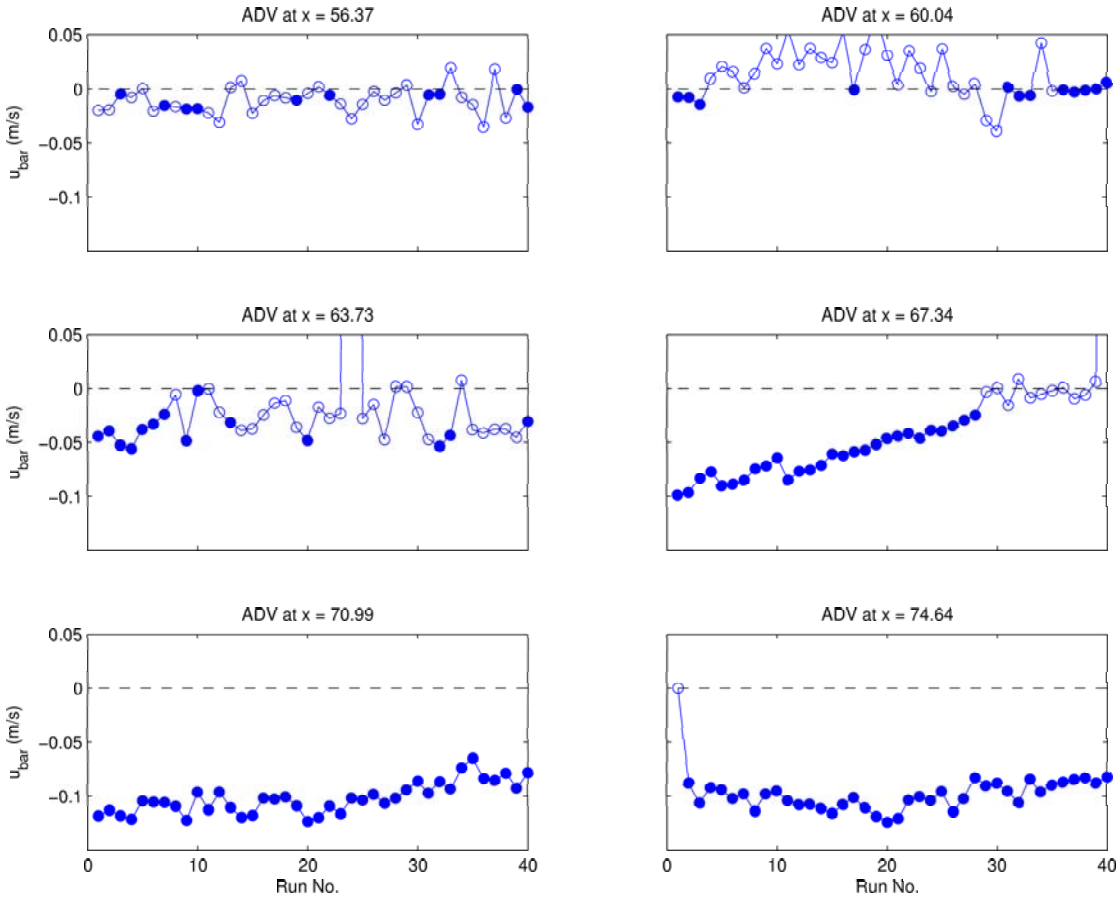

Fig. 3.7: *Onshore* Migration - Mean cross-shore velocity vs. run number for *original* sequence of wall-mounted ADV's. Clean Data (solid); Suspect data (open).

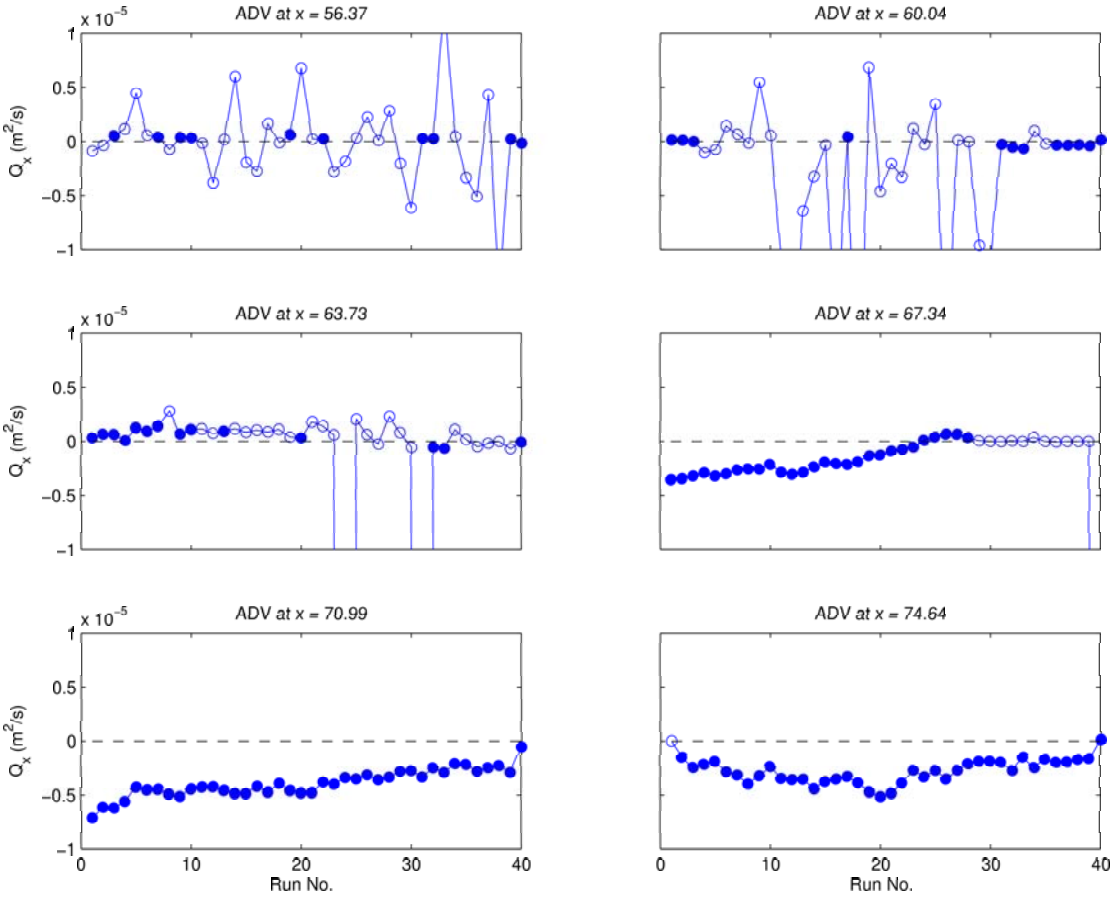

Fig. 3.8: *Onshore* Migration - Cross-shore sediment flux vs. run number for *original* sequence of wall-mounted ADV's. Clean Data (solid); Suspect data (open).

An alternative option was to replace subject ADV data with ADV data from the mobile carriage. During each wave run, the carriage migrated to a different cross-shore location of the tank. Therefore, if noisy wall-mounted ADV data files existed at a particular cross-shore location, we checked to see if the carriage was at the same cross-shore location for that particular wave run. If it was, then the data files from the lowest ADV on the carriage were analyzed in the same manner described above (for mean velocity and predicted sediment flux). Then if the data files contained similar (in magnitude) values for the parameters, then the carriage ADV data were deemed a suitable replacement for the suspect data as well.

As a matter of justification, the velocity data from the carriage should be more representative of the mean flows in the LWF that were driving the sediment transport since the

carriage ADVs were centered in the channel. Therefore, an ADV database was created with carriage ADV files substituted where appropriate. This database will be referred to as the *replacement* ADV database for the remainder of this report. The replacement ADV database, as used, is in Appendix C. Figures 3.9 and 3.10 show the mean flow and sediment flux parameters from the replacement database files.

The plots of the replacement velocity parameters appear like step-functions because there were several sequential files, generally, that needed to be replaced during the on-shore migration case. The largest 'steps' (in magnitude) appear when the carriage ADV information was inserted to replace noisy wall ADV information.

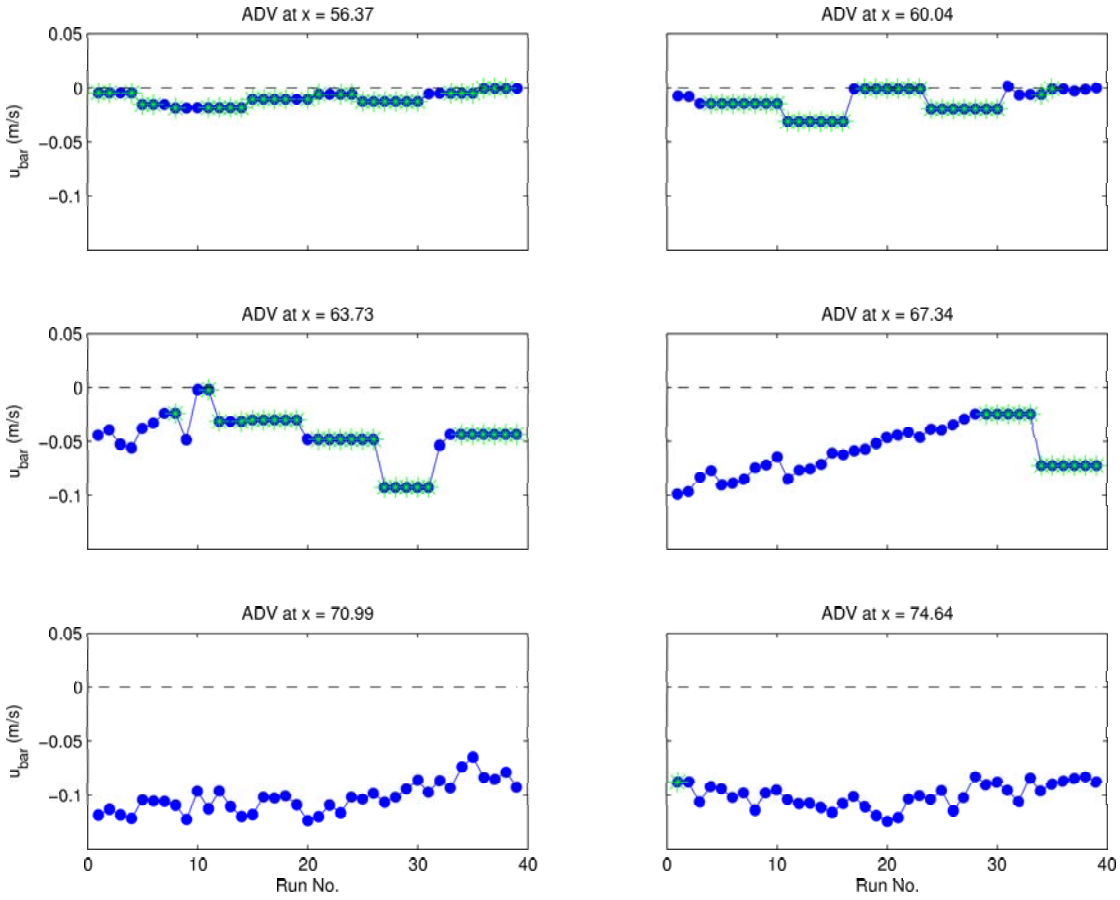

Fig. 3.9: *Onshore* Migration - Mean cross-shore velocity vs. run number for *replacement* sequence of wall-mounted ADV's. Existing data (blue circles); Replacement data (green stars)

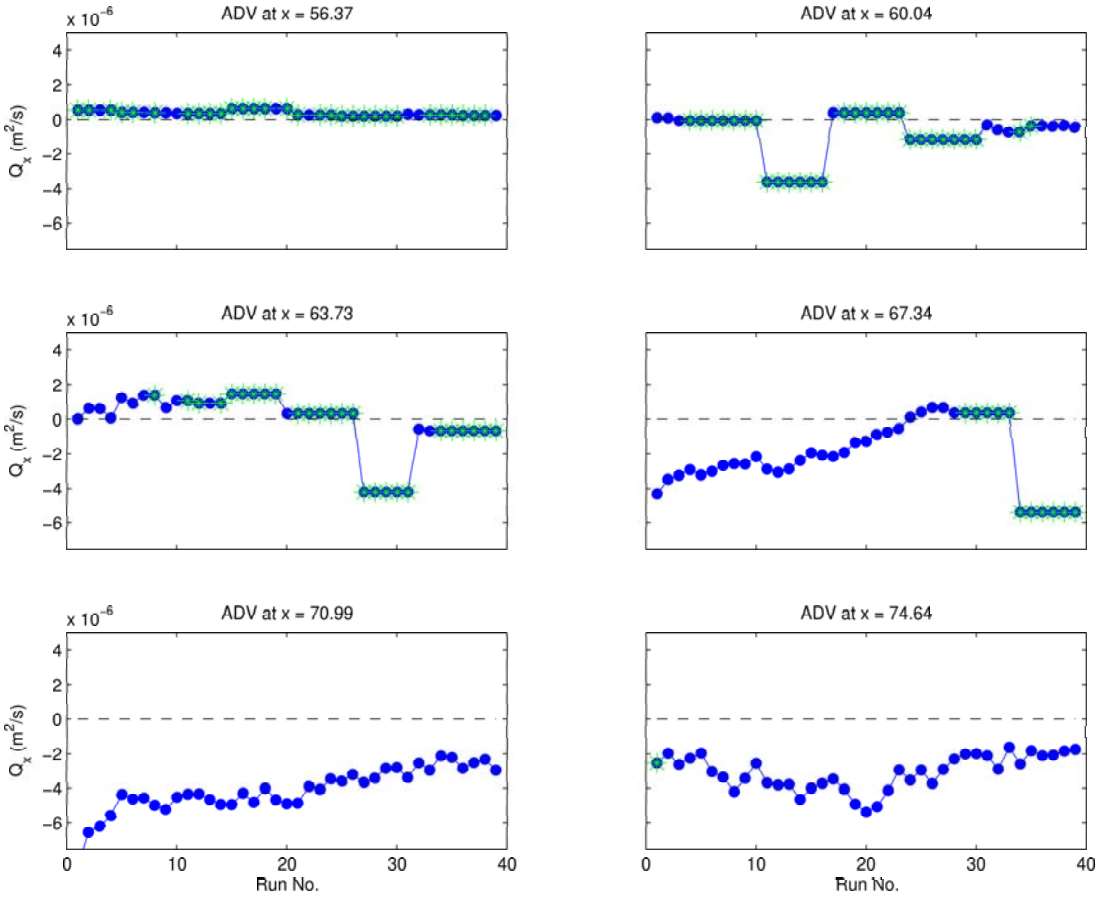

Fig. 3.10: *Onshore* Migration - Cross-shore sediment flux vs. run number for *replacement* sequence of wall-mounted ADV's. Existing data (blue circles); Replacement data (green stars)

3.5 Modeling Procedure

Both energetics-based models assume that velocity is measured at a depth immediately above the wave bottom boundary layer, requiring the near-bottom velocity data in order to drive the models. Initial and final bathymetric surveys provide the means by which to compare model predictions.

The modeling procedure was as follows:

1. Load the initial bathymetry from the survey database for the corresponding wave case (onshore vs. offshore) (Appendix C).

2. Load the corresponding velocity data from the *replacement* ADV database, per-

taining to the corresponding wave case and model run number (Appendix C).

- Cross-shore and along-shore velocity data were *not* initially low-pass filtered (Effects of this are discussed in Section 5.1.3). This deviated from the method of *Hoefel and Elgar* (2003). (They low-pass filtered with a cut-off frequency of 0.5 Hz.)

3. Sediment flux was computed using the velocity data at specific cross-shore locations. (with either the energetics model or the acceleration-based model)

4. Cross-shore gradients in the sediment flux were computed (either at instrument locations or at the mid-points of instrument locations; more detail on gradient computations in the next section).

5. The depth change was updated at specific cross-shore locations.

6. The procedure then repeated itself by loading each successive set of velocity data and predicting new bathymetric change.

7. The bathymetry was updated with the predictions for each successive model run, and can be compared to the observed bathymetry after each run, if desired.

8. The final predicted depths were compared to the final observed depths and model predictive skill was computed.

3.6 Sediment Flux Gradient Computation

While modeling with the CROSSTEX dataset, it became apparent that varying the method of computing sediment flux gradients led to widely different results. This finding is supported by other researchers who computed model skill values of the classical energetics model on the DUCK94 experimental data [*Plant et al.* (2004)]. Past modeling efforts have attempted to predict bathymetric change solely at the cross-shore instrument locations, where the near-bed velocities were measured. This report describes the results of computing bathymetric change at the instrument locations and also at the midpoints between the instruments. Hereinafter, any reference to computing bathymetric change at

the instruments (or instrument locations) means bathymetric change at the cross-shore locations at which ADVs were mounted on the LWF wall. Similarly, any reference to computing bathymetric change at the mid-points (or instrument mid-points) corresponds to computations made at the cross-shore mid-point location between wall-mounted ADVs.

3.6.1 Computations at Instrument Locations

Past experiments (e.g. DUCK94) had additional unfortunate complexity in analyzing bathymetric change because there was a cross-shore variation in instrument spacings. The standard second-order method for computing sediment flux gradients with unequal spacings is the Method for Unequal Spacings, described by *Plant et al.* (2004). This method computes the sediment flux gradient at a specific location, averaging the sediment flux at each of the adjacent cross-shore locations. A disadvantage to this method is that the furthest adjacent cross-shore location is weighted heavier than the nearest adjacent location.

The method used by *Gallagher et al.* (1998) on the DUCK94 data, called the Hybrid Method, weights the nearest adjacent cross-shore location heavier than the furthest location. This proved fortuitous for the model predictions of *Gallagher et al.* (1998) by improving model predictions and increasing the model predictive skill values [*Plant et al.* (2004)].

The instrument spacings during CROSSTEX, however, were constant and nearly equivalent for the duration of the experiment, allowing the decision between using the Method of Unequal Spacings or the Hybrid Method to be avoided. For this report, a central difference method was applied, the Method of Equal Grid Spacings, to predict bathymetric changes at the cross-shore instrument locations (6 cross-shore locations). For ease of discussion in this report, the cross-shore instrument locations are denoted as X = [56, 60, 64, 67, 71, 75] meters, rounded from actual cross-shore coordinates. To compute the sediment flux gradients, the following equation was used:

$$\frac{\partial}{\partial x}[Qx_i] \equiv \frac{Qx_{i+1} - Qx_{i-1}}{2\Delta x} \tag{3.12}$$

where Q is the sediment flux, as above, sampled at discrete locations x_i and Δx is a uniform distance between adjacent sample locations [*Plant et al.* (2004)]. The finite difference scheme used here began at the furthest offshore location and progressed shoreward.

The sediment flux gradient at the most offshore location was computed with a first-order forward difference by assuming zero sediment flux at a distance offshore (i.e. beyond the depth of closure):

$$\frac{\partial}{\partial x}[Qx_1] \equiv \frac{Qx_1 - Qx_0}{\Delta x_0} \tag{3.13}$$

in which $Qx_0 = 0$ and $\Delta x_0 = 6$ meters, beyond the depth of closure. This Δx distance was chosen because the bathymetry remained unchanged throughout the duration of the experiment at this cross-shore location.

The sediment flux gradient at the most onshore location was computed with a first-order backward difference as:

$$\frac{\partial}{\partial x}[Qx_2] \equiv \frac{Qx_2 - Qx_1}{\Delta x}. \tag{3.14}$$

The error associated with this central difference method was $\mathbf{O}(\Delta x)^2$.

3.6.2 Computations at Instrument Mid-points

Again, using the Method of Equal Grid Spacings, the sediment flux gradients were computed with a central difference, this time at the mid-point locations of sensors. The central-difference scheme began offshore and progressed shoreward using a similar equation to that seen in Eq. 3.12:

$$\frac{\partial}{\partial x}[Qx_{i+\frac{1}{2}}] \equiv \frac{Qx_{i+1} - Qx_i}{\Delta x}. \tag{3.15}$$

The resulting sediment flux gradient was applied to the cross-shore mid-point location between the two instrument locations $Qx_{i+\frac{1}{2}}$. The predicted bathymetry change was applied at the same location.

This method yielded one fewer number of predictive locations (5 cross-shore loca-

tions). Again, for ease of discussion, the cross-shore instrument mid-point locations are referred to as X = [58, 62, 65, 69, 73] meters, rounded from actual cross-shore coordinates.

The error associated with this central difference method was $\mathbf{O}(\frac{\Delta x}{2})^2$, which is smaller than that associated with the central difference method computed about the instrument locations. Therefore, prediction accuracy is presumably improved.

4. MODELING RESULTS

4.1 Modeling Offshore Migration

The offshore migration case (Figure 2.9) comprised of a total of 210 minutes (14 runs of 15 minutes each) of wave action. The waves were designed to be representative of storm waves (large wave heights, short wave periods; target $H_{mo} = 0.60$ meters, target $T_p = 4$ seconds). The sandbar crest migrated offshore approximately 3 meters from X = 64 meters to X = 61 meters.

4.1.1 Energetics Model - *Offshore Migration*

Results at Instrument Locations

A coefficient of friction of $C_f = 0.003$ was chosen for initial comparisons for all model results, the same value used in recent modeling efforts [*Thornton et al.* (1996); *Gallagher et al.* (1998)]. *(Model sensitivity to the friction coefficient is discussed in Section 5.1.2).* When the bathymetry was updated at the cross-shore instrument locations, the energetics model (EM) did not predict the building sandbar at X = 60 meters, nor the eroding trough at X = 64 meters, as expected (Figure 4.1). The trend of the model prediction at X = 60 meters appears in the correct direction (accretion), but at X = 64 meters, the model predicts accretion when erosion should be predicted.

The model predictions at the remaining cross-shore locations (X = 56, 67, 71 and 75 meters) are difficult to interpret since there was not a great deal of change between the initial and final observed bathymetry at those locations. At the two onshore locations (X = 71 and X = 75 meters), at least, the trend of erosion and accretion, respectively, appears to be correct.

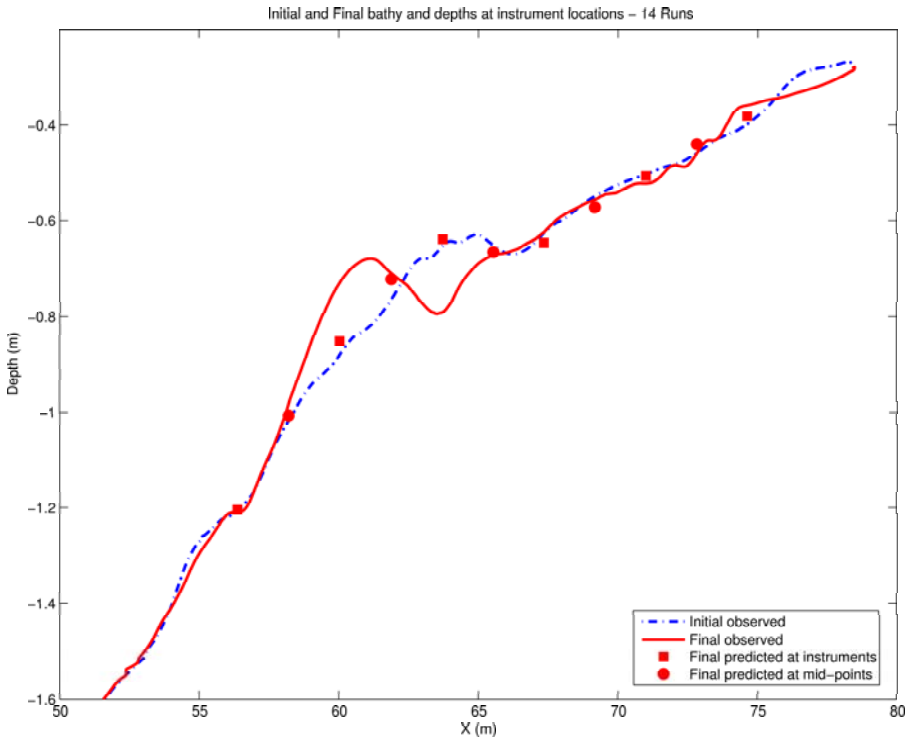

Fig. 4.1: *Offshore migration.* Energetics model at instrument locations: initial observations (dashed), final observations (solid), and final predictions (squares and circles).

Results at Instrument Midpoints

Computing the sediment flux gradient at the instrument mid-points appears to improve the model predictions slightly (Figure 4.1). Most notably, the prediction at cross-shore location X = 62 meters shows accretion nearly to the extent of the final observations. Furthermore, at the remaining cross-shore locations, X = 58, 65, 69 and 73 meters, the erosive and accretive trends are predicted, though the magnitudes of the erosion and accretion are not estimated accurately. It is difficult to interpret results from the predictions at these locations (as it was above for the instrument locations), however, due to the small bathymetric differences between the initial and final observed bed elevations.

Each model's predictive capabilities were analyzed by comparing model predictive skills. Following the methods of *Gallagher et al.* (1998) and *Henderson et al.* (2004), model skill was defined as

$$S = 1 - \frac{\int_a^b (h_p - h_f)^2 dx}{\int_a^b (h_i - h_f)^2 dx} \tag{4.1}$$

where h_i, h_f and h_p are respectively the observed initial, observed final and predicted final depths at the corresponding location (cross-shore instrument locations or cross-shore instrument mid-point locations), and a and b are the seaward- and shoreward-most locations at which the observed and predicted bathymetries are compared. Integrals were calculated using the trapezoidal rule and the known observed and predicted elevations at each corresponding cross-shore location.

Model predictive skill provided an objective measure for determining if model predictions were more accurate than if zero change had been predicted. A model predictive skill of 1 implied that the model predicted the elevation change perfectly. A positive model skill implied that the predictions were more accurate than a zero-change scenario. A negative model skill implied that the model predictions were less accurate than if no beach change had been predicted.

For the offshore migration case, using the energetics model formulation, the model predictive skill computing predictions at the mid-points sharply improved (S = 0.77) over the skill value at the instrument locations (S = 0.08) (See Table 4.1). It should be noted that model accuracy cannot be determined solely from model predictive skill, however. As others have found [*Gallagher et al.* (1998)], model predictions may be visually appealing, yet correspond to low (or negative) model predictive skills. This occurs when the difference between the initial and final observed depths is small, so the denominator in the equation for model skill becomes very small. The difference between the predicted and observed depths is large, however, creating a large number to be subtracted. This result was observed in certain modeling scenarios in this report. Instances will be discussed in later sections.

Bathymetric Change - Observations vs. Predictions

To compare the predictive capabilities of the energetics and acceleration-based models, elevation changes at each cross-shore location (instrument and instrument mid-point)

were plotted over the duration of the offshore migration (Figure 4.2).

The EM's under-prediction of accretion at X = 60 meters is evident over time here. Additionally, the over-prediction of erosion observed at cross-shore location X = 64 meters is visible.

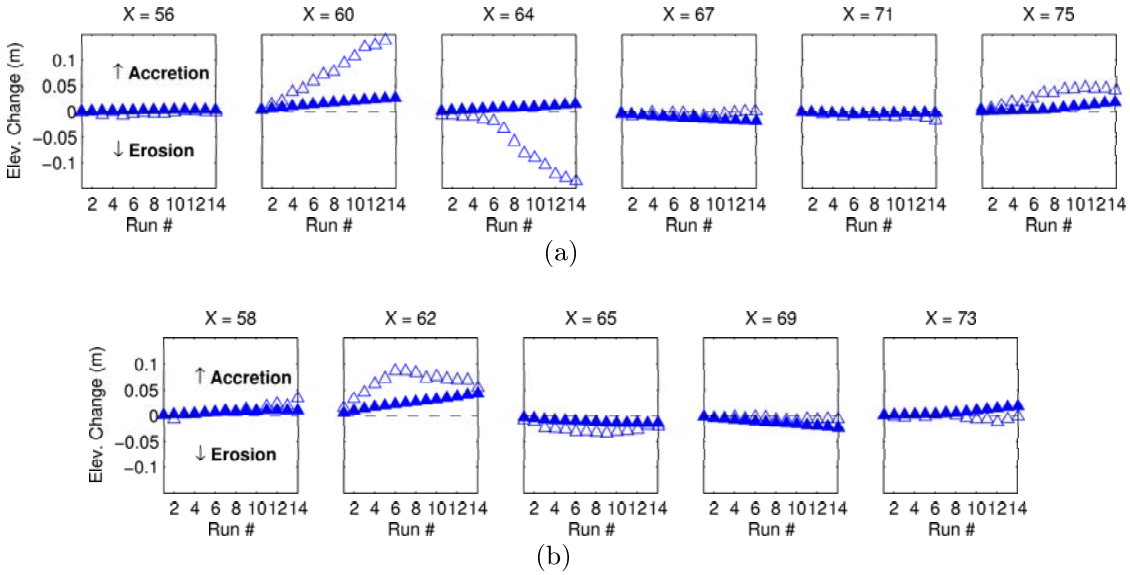

Fig. 4.2: *Offshore migration.* Energetics model - observed (open symbols) and predicted (closed symbols) of elevation change for each wave run (a) at the instrument locations and (b) at the instrument mid-points.

When the calculations were performed at the instrument mid-points, the predictions appeared to follow the trends of the observations. Interestingly, at cross-shore location X = 62 meters, the model predictions deviated from the observations, but later converged at the conclusion of the offshore migration case. This depicts the time in which the sandbar migrated offshore, past this location. But the model was predicting continuous growth of the bar at the end of the run.

Interpretation of model predictions should be done with care because model predictive skill was not always indicative of accurate modeling. If one were to compare the final observed and predicted bathymetries, the model would appear to predict the change quite well. In fact, the model skill level is quite high when computed at the instrument mid-points (S = 0.77). However, in Figure 4.2 (at X = 62 meters) it is evident that

the model predictions do not predict the migration of the sandbar at each time step, but fortuitously converge with the observations at the conclusion of the wave case. This ultimately resulted in the extremely large model predictive skill.

4.1.2 Acceleration-Based Model - *Offshore Migration*

Results at Instrument Locations

When the acceleration-based model (AM) was applied to the offshore migration case, the model predictions were very similar to that of the energetics model. Figure 4.3 shows the model predictions with the best-fit free parameters (a_{crit} and K_a) determined by minimizing the root mean square errors (rms) between the final observations and model predictions (See Section 4.3). The best-fit parameters are given in Table 4.1. The similarities between the model predictions of the energetics and acceleration-based model were not unexpected because the acceleration-based term was not expected to be a dominant contributor during erosive wave conditions, where undertow should be the dominant factor.

As in the energetics model predictions above, the accreting sandbar at X = 60 and the eroding trough at X = 64 were not predicted. At the latter location, the sign of the depth change was still not predicted correctly (the model predicted accretion when erosion was observed).

Results at Instrument Midpoints

Model predictions at the instrument mid-points were also similar for both models (Figure 4.3). The AM predicted transport trends similar to the EM, but the final predicted depths of the AM were further from the final observed depths than the final predicted EM depths. The minor differences are reflected visually but are not significant in the model predictive skills. The model skill remained essentially the same as in the energetics case (AM skill S = 0.08) at the instrument location and (AM skill S = 0.77) at the mid-points (Table 4.1).

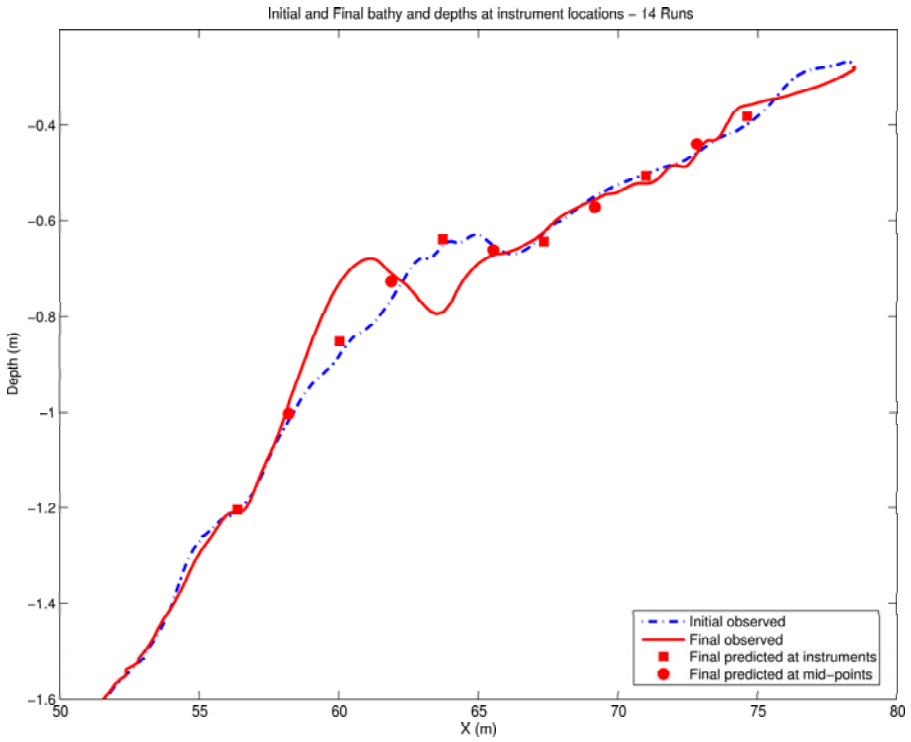

Fig. 4.3: *Offshore migration.* Acceleration-based model at instrument locations: Initial observations (dashed), final observations (solid), and final predictions (squares and circles).

Bathymetric Change - Observations vs. Predictions

The observed and predicted change from the acceleration-based model are shown in Figure 4.4. The trends of the predictions are similar to that of the energetics model.(Figure 4.4).

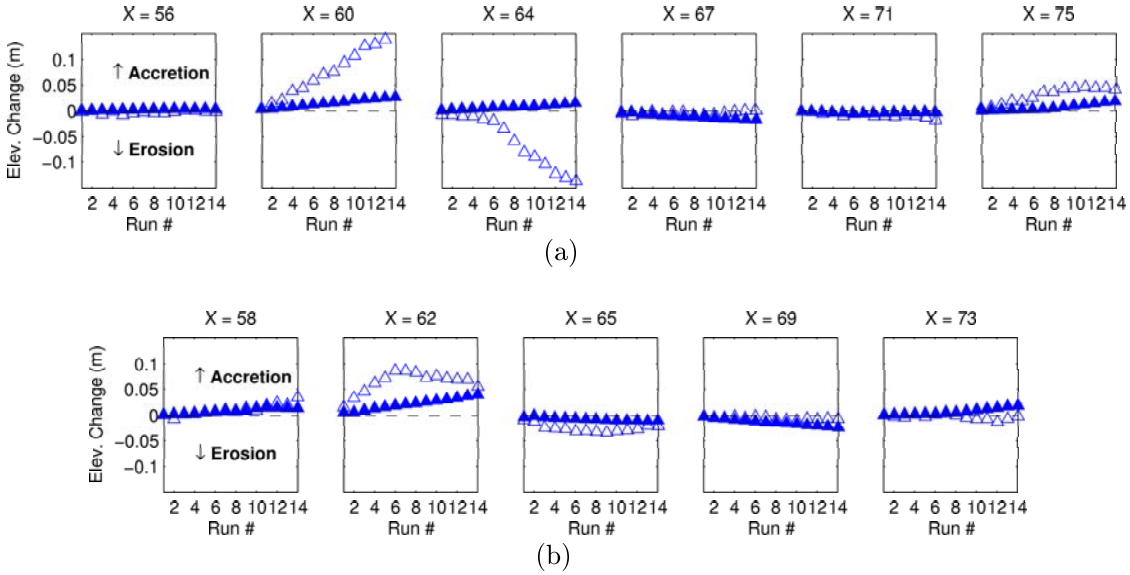

Fig. 4.4: *Offshore migration.* Acceleration-based model - Observed (open symbols) and predicted (closed symbols) of elevation change for each wave run (a) at the instrument locations and (b) at the instrument mid-points.

4.2 Modeling Onshore Migration

The onshore migration case discussed in this report (*onshore migration I*, Figure 2.10) was comprised of a total of 675 minutes of wave action. The waves were designed to be representative of storm recovery periods (small wave heights, longer wave periods; target $H_{mo} = 0.32 - 0.35$ meters, target $T_p = 8$ seconds). Erosion of an offshore bar was observed near X = 61 meters, the trough was infilled and sandbar built near X = 68 meters. The crest of the sandbar moved onshore approximately 7 meters during this time period.

4.2.1 Energetics Model - *Onshore Migration*

Results at Instrument Locations

When the EM was applied to the onshore migration case, the final predictions varied little from the initial observed depths. The erosion of the sandbar at X = 59 was not predicted, the trough infilling was not predicted at X = 64 and the building sandbar was

not predicted at X = 67 meters (Figure 4.5). The model predictive skill value was low (S = 0.2) when computed at the instrument locations (Table 4.2).

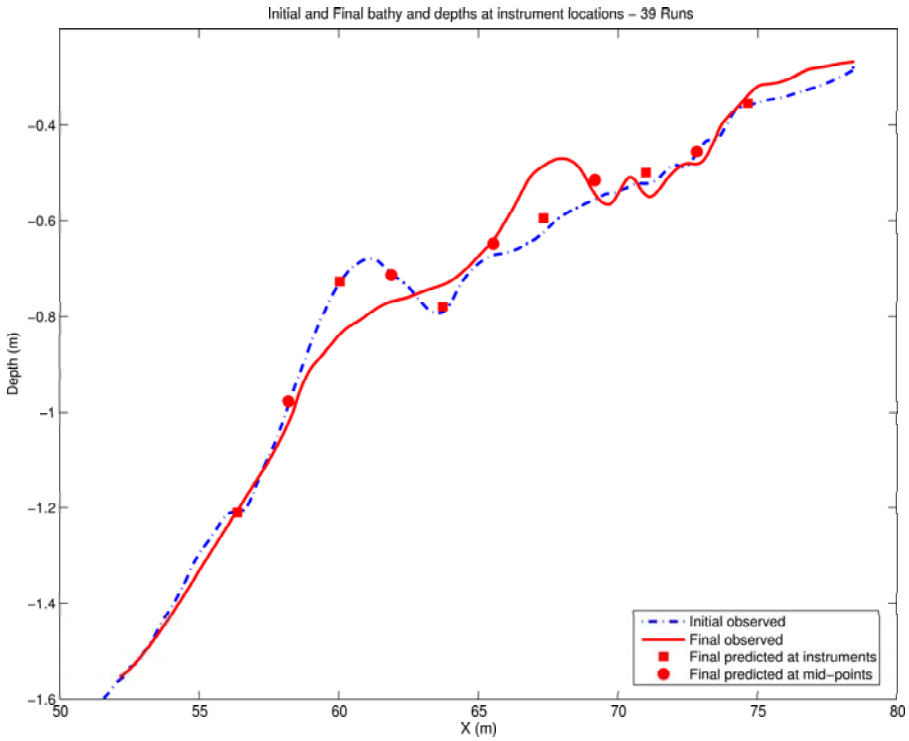

Fig. 4.5: *Onshore migration.* Energetics model at instrument locations: Initial observations (dashed), final observations (solid), and final predictions (squares and circles).

Results at Instrument Midpoints

Predictions were not improved a great amount by computing bathymetric changes at the instrument mid-points. Skill level actually decreased (S = 0.14) from that computed at the instrument locations. Erosion of the offshore sandbar was not predicted at cross-shore location X = 62. Slight accretion was predicted, however, at locations X = 65 and X = 69 meters, in accordance with observations. This appears to improve model accuracy, but it is difficult to interpret this result since there is no model behavior predicted between these locations; solely the sides of the bar are predicted (Figure 4.5). The model makes no predictions about the bathymetric change at locations in between.

Bathymetric Change - Observations vs. Predictions

For many of the cross-shore locations during the onshore sediment migration, the model-predicted depths deviated from the observed depths over time (see Figure 4.6). Specifically, cross-shore locations X = 58, 60, 62 and 67 showed the largest discrepancies. Some encouraging results were observed at locations X = 65 and 69 meters, though. The accretionary trends and magnitudes of the observations at these locations were predicted by the model.

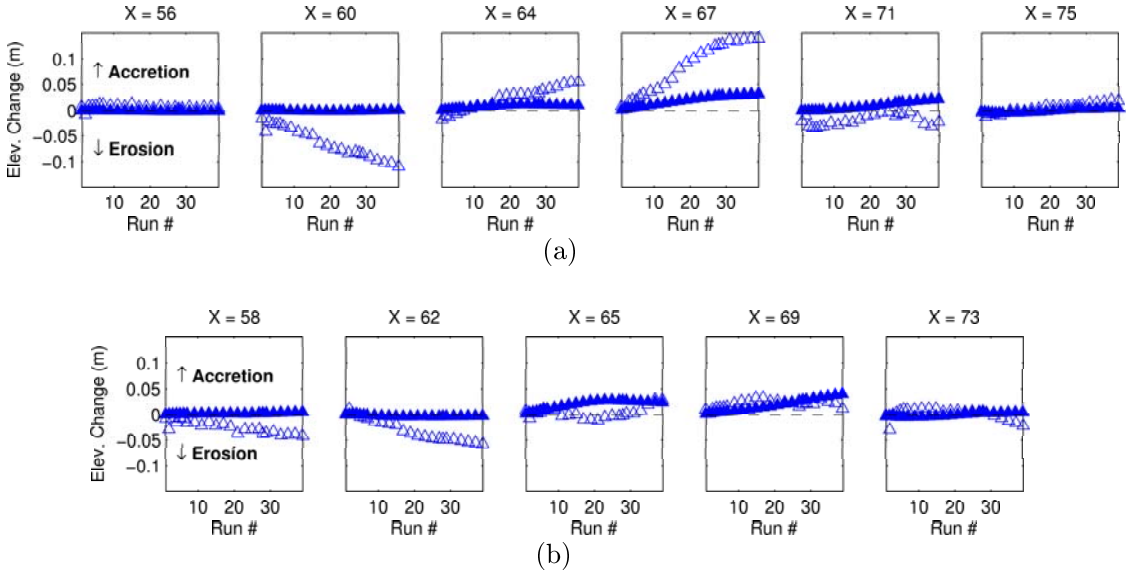

Fig. 4.6: *Onshore migration.* Energetics model - Observed (open symbols) and predicted (closed symbols) of elevation change for each wave run (a) at the instrument locations and (b) at the instrument mid-points.

4.2.2 Acceleration-Based Model - *Onshore Migration*

Results at Instrument Locations

When the AM was applied to the onshore migration data, predictions significantly improved over those of the EM (Figure 4.7). Most notably, the model predictions were improved at location X = 60, where the AM accurately predicted erosion of the existing sandbar and formation of a new sandbar at X = 67. There was also slight accretion predicted at location X = 64, in accordance with observations. Model predictive skill was high (S = 0.82) at the instrument locations.

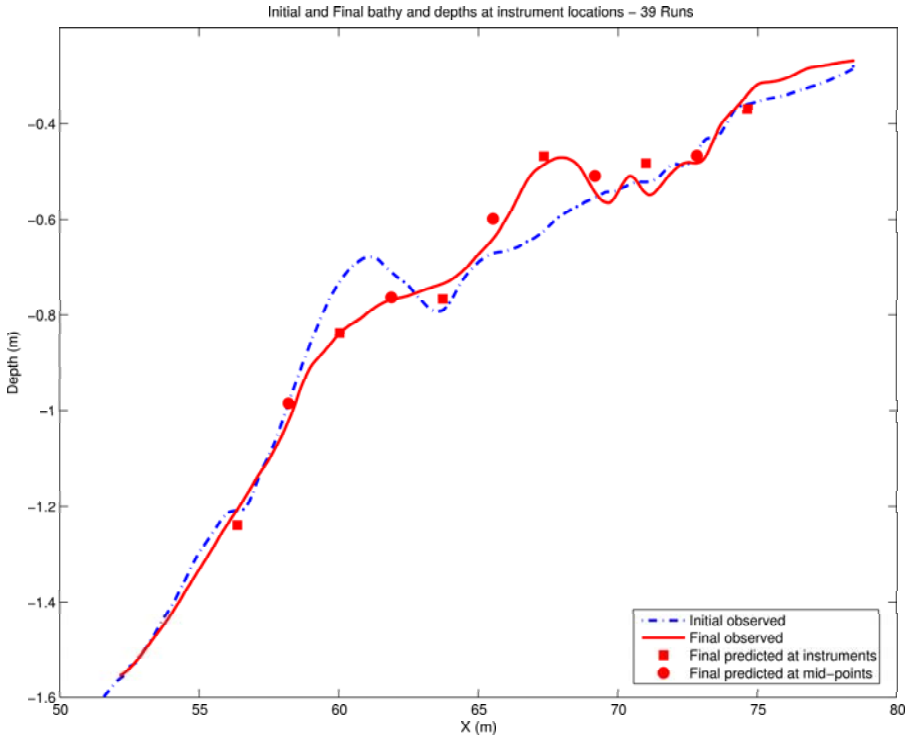

Fig. 4.7: *Onshore migration.* Acceleration-based model at instrument locations: Initial observations (dashed), final observations (solid), and final predictions (squares and circles).

Results at Instrument Mid-point Locations

Similarly, the AM predictions at the instrument mid-points showed improvement over the EM predictions at the mid-points (though skill decreased at the mid-points from the instrument locations to S = 0.25). At cross-shore location X = 62, the erosion of

the existing sandbar was properly predicted (Figure 4.7. Furthermore, at locations X = 65 and 69, more accretion was predicted by the AM than the EM, in accordance with the large sandbar observed between those two cross-shore locations. This is difficult to interpret, again, since the prediction locations from the AM (as in the EM) fall to the sides of the observed sandbar. This is an example of when predictions may appear visually appealing, but have a low model predictive skill value. The difference between the initial and final observed depths at X = 65 and 69 are small, but the predicted depths are much further away.

Bathymetric Change - Observations vs. Predictions

The improved predictive capabilities of the AM are evident in the comparisons of observed and predicted depths for each 15 minute time period (Figure 4.8). Specifically, locations X = 60 and 67 meters show large improvement over the EM predictions, when predictions are made at instrument locations. The predictions at these locations at each time step follow the same trends of magnitude and direction of transport as the observations.

Similarly, at the instrument mid-points, model predictions at each time step are improved for location X = 62. On the other hand, at location X = 65 the model predictions show more deviation than the energetics model when compared to observed predictions at each time step.

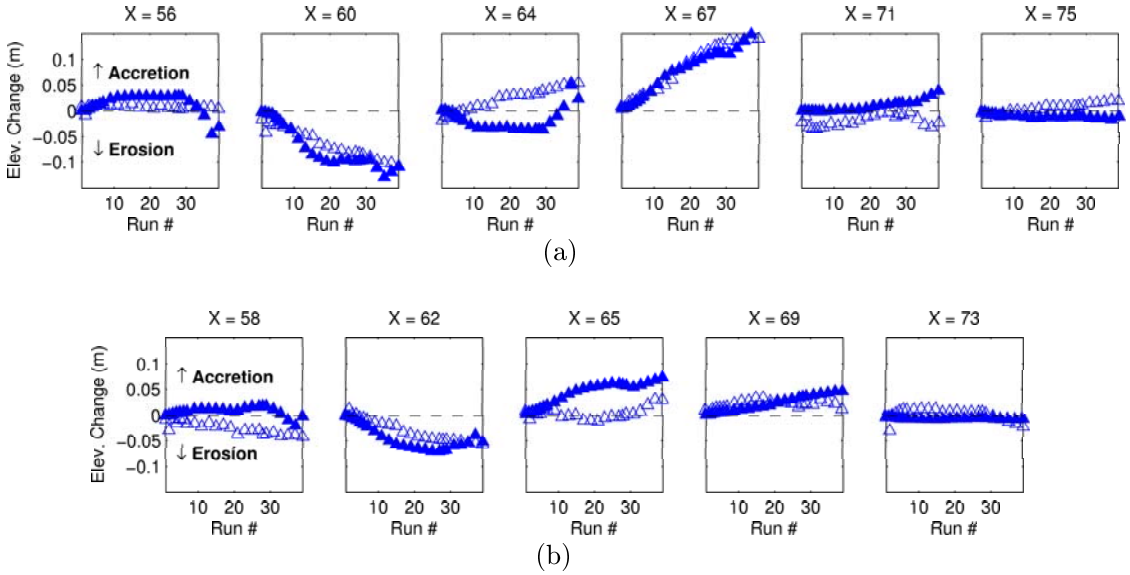

Fig. 4.8: *Onshore migration.* Acceleration-based model - Observed (open symbols) and predicted (closed symbols) of elevation change for each wave run (a) at the instrument locations and (b) at the instrument mid-points.

4.3 Best-fit Free Parameter Selection

Since the acceleration-based model added two additional free parameters, a best-fit analysis was required to determine the optimal a_{crit} and K_a values to use. The best-fit free parameters were chosen by minimizing the root-mean-square (rms) errors between the final predicted and observed depths. Often the minimum rms values corresponded to the maximum model predictive skill values. At times, however the maximum skill value did not correspond to the same free parameters as the minimum rms-errors. This was observed when the model predictive skills were negative, which made determination of best-fit parameters by model skill difficult.

Upon further analysis, it was evident that the model predictions were not affected if the model parameters were chosen either by minimizing rms errors or by maximizing model skill values, though. For instance, the model predictive skills differed by $\mathbf{O}(10^{-2})$ depending on if a model was fit by minimizing the rms errors or by maximizing the model predictive skill. For consistency, therefore, the best-fit free parameters in this report were selected by minimizing the rms errors. Free parameters and model predictive skills from

the *replacement* database are listed in Tables 4.1 and 4.2.

Table 4.1: Model Predictive Skill Statistics for *Offshore* Migration

		Model Fits to Instrument Locations				Model Fits to Instrument Mid-points			
	Cf	acrit	Ka	RMS error	Skill	acrit	Ka	RMS error	Skill
Energetics	0.001	-	-	0.043	0.03	-	-	0.013	0.41
	0.003	-	-	0.042	0.08	-	-	0.01	0.76
	0.005	-	-	0.041	0.09	-	-	0.01	0.50
	0.0065	-	-	0.041	0.08	-	-	0.02	-0.13
	0.01	-	-	0.044	-0.01	-	-	0.03	-3.05
Acceleration-based	0.001	0.7	5.0E-05	0.043	0.03	0.9	1.0E-05	0.013	0.41
	0.003	0.7	11.0E-05	0.042	0.08	0.7	5.0E-05	0.009	0.77
	0.005	0.7	11.0E-05	0.041	0.09	0.6	11.0E-05	0.011	0.58
	0.0065	0.6	11.0E-05	0.040	0.09	0.5	11.0E-05	0.015	0.17
	0.01	0.6	11.0E-05	0.043	0.002	0.4	11.0E-05	0.028	-1.99

Table 4.2: Model Predictive Skill Statistics for *Onshore* Migration

	Cf	acrit	Ka	RMS error	Skill	acrit	Ka	RMS error	Skill
Energetics	0.001	-	-	0.038	0.07	-	-	0.018	0.12
	0.003	-	-	0.040	0.20	-	-	0.02	0.14
	0.005	-	-	0.030	0.30	-	-	0.02	-0.17
	0.0065	-	-	0.030	0.35	-	-	0.025	-0.61
	0.01	-	-	0.030	0.40	-	-	0.035	-2.40
Acceleration-based	0.001	0.2	5.0E-05	0.017	0.84	0.10	1.0E-05	0.01	0.73
	0.003	0.2	5.0E-05	0.018	0.82	0.1	1.0E-05	0.017	0.25
	0.005	0.2	3.0E-05	0.019	0.79	0.7	1.0E-05	0.023	-0.42
	0.0065	0.2	3.0E-05	0.020	0.77	1.0	1.0E-05	0.026	-0.84
	0.01	0.2	3.0E-05	0.024	0.66	1.0	1.0E-05	0.035	-2.45

It is noteworthy to mention that model predictive skills for the offshore migration case were larger when computed at the instrument *mid-point* locations than at the instrument locations. Conversely, for the onshore migration case, the model skills were larger at the instrument locations than the instrument mid-points. The reason for this is unclear, but may be attributed to the locations of the predictions relative to significant features of the profile (e.g. bar crest and trough). The sand bar crest and trough formed most near the instrument *mid-points* in the offshore case, and at the instrument locations for the onshore case.

5. MODEL SENSITIVITY

5.1 Model Sensitivity

5.1.1 Varying Acceleration Skewness Parameters

The best-fit parameters a_{crit} and K_a found for the CROSSTEX data are within the acceptable ranges of those suggested by other researchers ($a_{crit} = 1m/s^2$, $K_a = 0.26 \times 10^{-4} m \cdot s$) [*Drake and Calantoni* (2001)] and ($a_{crit} = 0.2\ m/s^2$, $K_a = 1.40 \times 10^{-4}\ m \cdot s$) [*Hoefel and Elgar* (2003)] for both sediment migration directions. The best-fit threshold a_{crit} for the offshore migration case was nearly 2-3 times the magnitude of that for the onshore migration. However, the best-fit values for the constant, K_a, were also larger for the offshore case than the onshore case.

This also supports an earlier statement that different combinations of best-fit parameters may lead to similar model predictions (i.e if a_{crit} increases, K_a needs to increase accordingly). Figure 5.1 shows the predicted depths from the *offshore* migration, modeled with the best-fit parameters found for the *onshore* migration ($a_{crit} = 0.2m/s^2$, $K_a = 5 \times 10^{-5} m \cdot s$ for the instrument locations and ($a_{crit} = 0.1m/s^2$, $K_a = 1 \times 10^{-5} m \cdot s$) for the mid-point locations). The model skills decreasd slightly (from S = 0.08 to S = -0.17 for the instruments; and from S = 0.76 to S = 0.60 for the mid-point locations). However, the model predicted depths did not appear to vary greatly from the predictions that were obtained using the best-fit free parameters for the *offshore* case (Figure 5.2). From this result, it appeared that the model was relatively insensitive to varying free parameters in *energetic* wave conditions. This made sense because the physics involved in a_{crit} and K_a are not dominant in the offshore migratory case. The values of a_{crit} and K_a should be less relevant in the energetic wave conditions.

It is important to note that the parameters associated with the most accurate *onshore* migration model fit work well for the entire dataset (i.e. both offshore and onshore transport). In other words, tuning the model so that it fits with a high degree of accuracy

to the onshore migration results in an high degree of accuracy with the *offhore* migration as well.

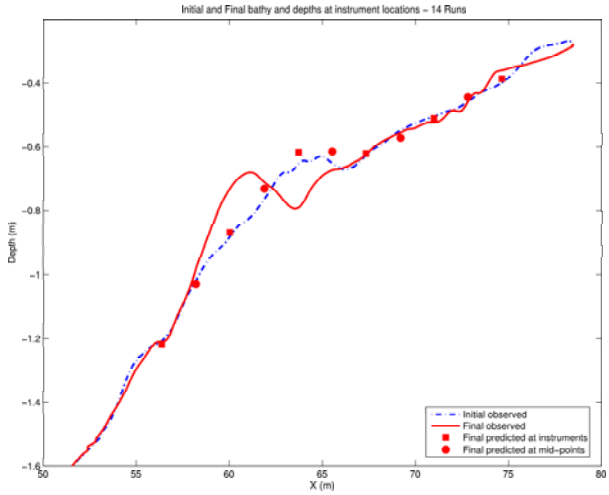

Fig. 5.1: *Offshore* migration predicted with *onshore* migration best-fit parameters (acceleration-based model). Initial observations (dashed), final observations (solid), and final predictions (squares and circles).

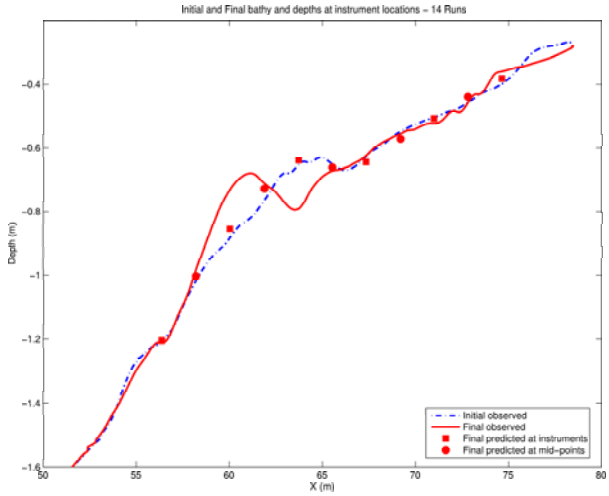

Fig. 5.2: *Offshore* migration predicted with *offshore* migration best-fit parameters (acceleration-based model). Initial observations (dashed), final observations (solid), and final predictions (squares and circles).

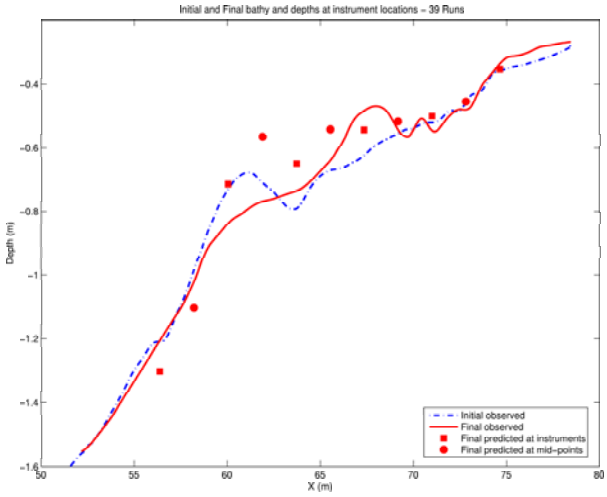

Fig. 5.3: *Onshore* migration predicted with *offshore* migration best-fit parameters (acceleration-based model). Initial observations (dashed), final observations (solid), and final predictions (squares and circles).

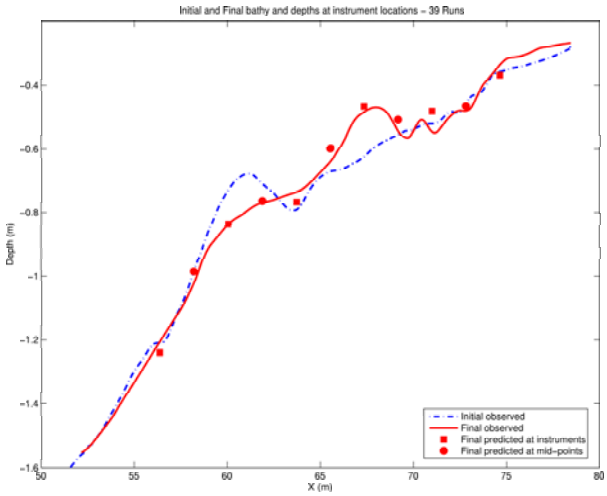

Fig. 5.4: *Onshore* migration predicted with *onshore* migration best-fit parameters (acceleration-based model). Initial observations (dashed), final observations (solid), and final predictions (squares and circles).

Conversely, model predictions proved to be much more sensitive for the *onshore* migration predictions when the best-fit parameters from the *offshore* migration for the instrument locations ($a_{crit} = 0.7m/s^2$, $K_a = 1.1 \times 10^{-4} m \cdot s$) and for the mid-point locations ($a_{crit} = 0.7m/s^2$, $K_a = 5 \times 10^{-5} m \cdot s$) were used. The model skills decreased severely (from S = 0.82 to S = 0.09 for the instruments; and from S = 0.25 to S = -2.20 for the mid-point locations). And, visually, the predictions were less accurate than those

obtained with the best-fit parameters corresponding to the onshore migration (Figures 5.3 and 5.4).

5.1.2 Varying Friction Coefficient

Varying the coefficient of friction, C_f =0.001, 0.005, 0.0065 and 0.010, had different impacts on the two migrations, offshore and onshore. For the *offshore* migration, the friction coefficient only affected the predicted magnitudes of depth change, but not the direction of predicted sediment transport. In other words, accretion and erosion were predicted in the same directions, but the magnitudes of each decreased (increased) with decreasing (increasing) C_f (Figure 5.5). This was true at both the instrument and mid-point locations. Model skills decreased with varying friction (Table 4.1), and predictions were visually less appealing than those with $C_f = 0.003$. Therefore, for the offshore migration, the conclusion is that the friction coefficient should remain at the value used by other researchers, $C_f = 0.003$.

For the *onshore* migration, decreasing the friction coefficient resulted in increased model predictive skills for both the instrument locations and the mid-point locations. The improved predictability at the instrument locations is evident in Figure 5.6. Improvements in predictive capability at the mid-points was also observed for different best-fit parameters, but are not shown in this report.

Applying a larger firction coefficient to the onshore migration case caused minor variations in predicted depths from those predicted when $C_f = 0.003$. However, model predictive skill values decreased as the friction coefficient increased (Table 4.2), in similar agreement to the findings during the offshore migration case. Additional plots from this analysis are not shown in this report.

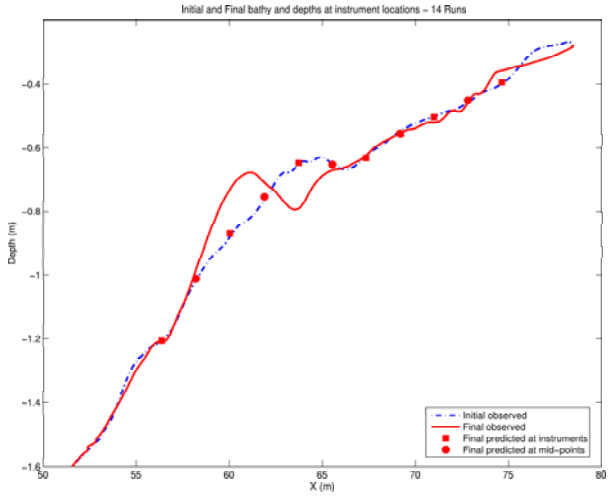

Fig. 5.5: *Offshore* Migration with $C_f = 0.001$. Initial observations (dashed), final observations (solid), and final predictions (squares and circles).

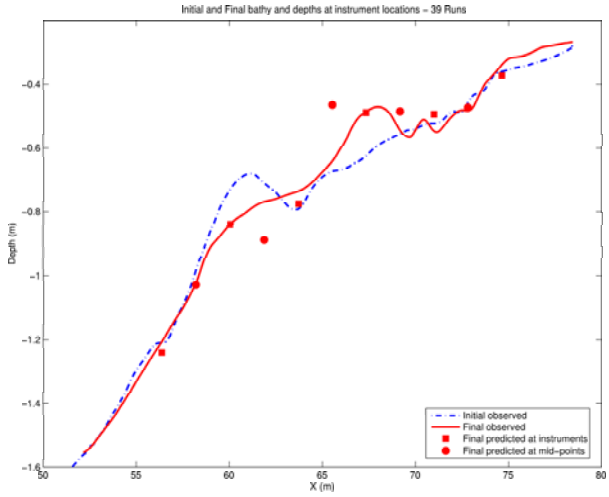

Fig. 5.6: *Onshore* Migration with $C_f = 0.001$. Initial observations (dashed), final observations (solid), and final predictions (squares and circles).

5.1.3 Low-pass Filtering of Velocity Data

[*Hoefel and Elgar* (2003)] first applied the AM on the DUCK94 experimental data. They low-pass filtered their velocity data (low-pass cutoff of 0.5 Hz on data collected at 2 Hz) prior to predicting the sediment transport to eliminate effects of high-frequency instrument noise on the acceleration computations. Therefore, to determine the effect that high frequency noise had on model predictions and sensitivity, the CROSSTEX velocimeter data were low-pass filtered prior to computing sediment transport.

The low-pass cutoff chosen for this analysis was $f_c = 1$ Hz based on a coherence analysis. Coherence was computed between co-located wave gages and near-bottom measuring current meters. The equation used for coherence was:

$$\hat{\gamma}^2_{xy}(f) = \frac{|\hat{G}_{xy}(f)|^2}{\hat{G}_{xx}(f)\hat{G}_{yy}(f)} \tag{5.1}$$

in which γ is the coherence, $\hat{G}_{xx}$ is the autospectral density and $\hat{G}_{xy}$ is the cross-spectral density between the wave gage and ADV power spectrums. Signals were coherent at the 95% confidence limit if $\hat{\gamma}^2_{xy}(f) > \mathrm{C}$, where

$$\mathrm{C} = \sqrt{1 - 0.05^{1/nblocks-1}}, \tag{5.2}$$

and nblocks is the number of blocks over which each spectrum was averaged (See Bartlett averaging scheme in Section 2.6.1).

In this report, only plots from the low-pass filtering sensitivity analysis for the acceleration-based model are shown. The reason for this is that applying low-pass filtered velocity data to the offshore migratory case resulted in minor variations in model predictive skill and chosen best-fit model parameters (Table 5.1).

The low-pass filtered model predictions for the onshore migration case are shown in Figure 5.7. For comparison, the model predictions for the onshore migration case without low-pass filtering are shown in Figure 5.8).

At the instrument locations, the sandbar at X = 60 was not predicted to erode as much and the trough at X = 64 was not infilled as much with the low-pass filtered data as it was for the unfiltered data. The model skill values of the low-pass filtered data at the instrument locations reflect this decline with lower skill values (Table 5.2).

The instrument mid-point predictions with low-pass filtered data were also not predicted as well as the unfiltered predictions. The trough infill was not predicted at X = 64, and the sediment accretion at X = 67 was not predicted by the low-pass filtered data. The model skill values at the instrument mid-points also decreased when the low-pass filtered data were used.

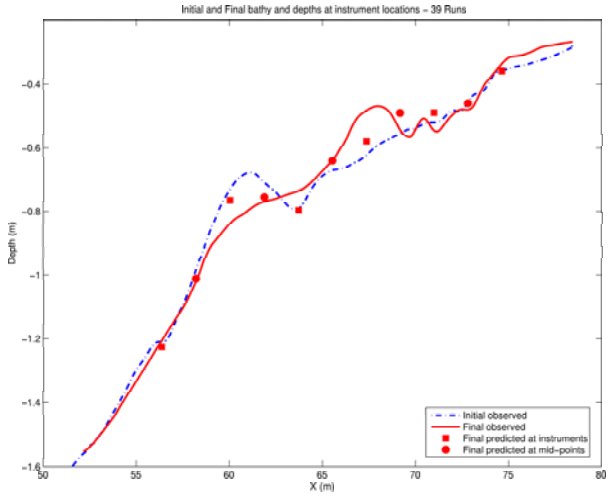

Fig. 5.7: *Onshore* migration predictions (AM Model) with 1 Hz. low-pass filtering. Initial observations (dashed), final observations (solid), and final predictions (squares and circles).

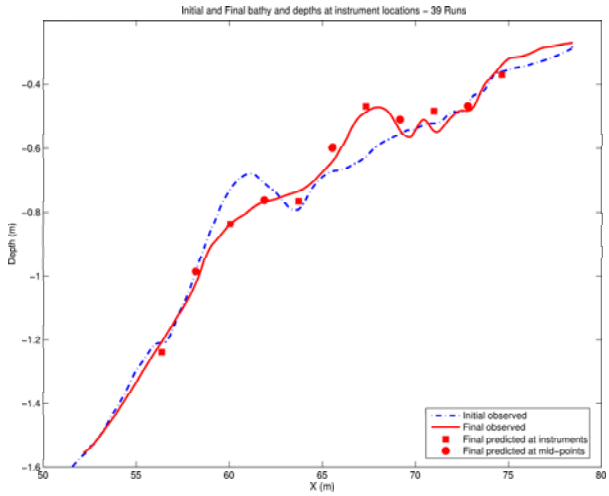

Fig. 5.8: *Onshore* migration predictions (AM Model) with no low-pass filtering. Initial observations (dashed), final observations (solid), and final predictions (squares and circles).

The conclusion is that low-pass filtering the data had little effect on the energetic offshore migratory conditions. The model predictive skills and best-fit model free parameters remained relatively unchanged for this case. As shown above, however, the model predictions were visually less appealing for the onshore migratory conditions. Correspondingly, the model predictive skill values were smaller than those computed from the unfiltered velocity model predictions.

Table 5.1: Low-Pass Filtered Model Predictive Skill Statistics for *Offshore* Migration

		Model Fits to Instrument Locations				Model Fits to Instrument Mid-points			
	Cf	acrit	Ka	RMS error	Skill	acrit	Ka	RMS error	Skill
Acceleration-based model	0.001	0.9	1E-05	0.043	0.035	0.9	1.0E-05	0.013	0.41
	0.003	0.9	1.0E-05	0.042	0.08	0.9	1.0E-05	0.009	0.78
	0.005	0.9	1.0E-05	0.041	0.10	0.7	9.0E-05	0.012	0.57
	0.0065	0.9	1.0E-05	0.041	0.09	0.6	7.0E-05	0.016	0.16
	0.01	0.8	7.0E-05	0.043	0.14	0.6	11E-05	0.027	-1.69

Table 5.2: Low-Pass Filtered Model Predictive Skill Statistics for *Onshore* Migration

	Cf	acrit	Ka	RMS error	Skill	acrit	Ka	RMS error	Skill
Acceleration-based model	0.001	0.1	1.0E-05	0.034	0.29	0.1	1.0E-05	0.011	0.62
	0.003	0.1	1.0E-05	0.030	0.40	0.1	1.0E-05	0.014	0.42
	0.005	0.1	1.0E-05	0.030	0.48	0.1	1.0E-05	0.019	-0.09
	0.0065	0.1	1.0E-05	0.028	0.51	0.1	1.0E-05	0.023	-0.61
	0.01	0.1	1.0E-05	0.027	0.53	0.1	1.0E-05	0.034	-2.25

5.1.4 Alternative ADV Database

An alternative ADV database was created by omitting the carriage ADV data and using solely wall-mounted ADV data. This decision was made because the significant hydrodynamic parameters ($\bar{u}$ and Q_x) measured and predicted by the carriage velocity files were, at times, significantly different than those of the adjacent wall-mounted ADV data. This was shown previously in Figures 3.9 and 3.10. Sharp 'jumps' occurred in the plots where carriage data were inserted, and potentially influenced the sediment transport model predictions. Therefore, to analyze the model sensitivity to replacing the carriage velocity data, the carriage data files were replaced with existing wall-mounted ADV data files.

During some periods of record, replacing the carriage ADV files solely with wall-mounted ADV files caused a greater number of sequential model runs to be replaced by a single data file. The $\bar{u}$ and Q_x parameters computed by this substitution, however, were more similar to the surrounding (in time) hydrodynamics than the carriage data replacement files.

The sensitivity analysis in this report was performed for the *onshore* migration case only since the offshore migration database did not use any carriage data as replacements. For the remainder of this report, the new ADV database will be referred to as the *alternative* replacement database. The sensitivity analysis was performed without low-pass filtering the data for comparison purposes.

Figures 5.9 and 5.10 show the $\bar{u}$ and Q_x measurements and predictions from the alternative replacement ADV database. The magnitudes of the 'jumps' are not as large as those that were seen using the original replacement database (with carriage ADV files).

Using the alternative replacement database served to increase model predictive skills and improve the predictions visually. Figure 5.11 displays the model predictions with the best-fit model parameters for the instrument locations. Similar predictions were made by tuning the model to the mid-point predictions. Those plots are not shown in this report, however. Table 5.3 lists the best-fit free parameters for the instrument locations with the alternative database.

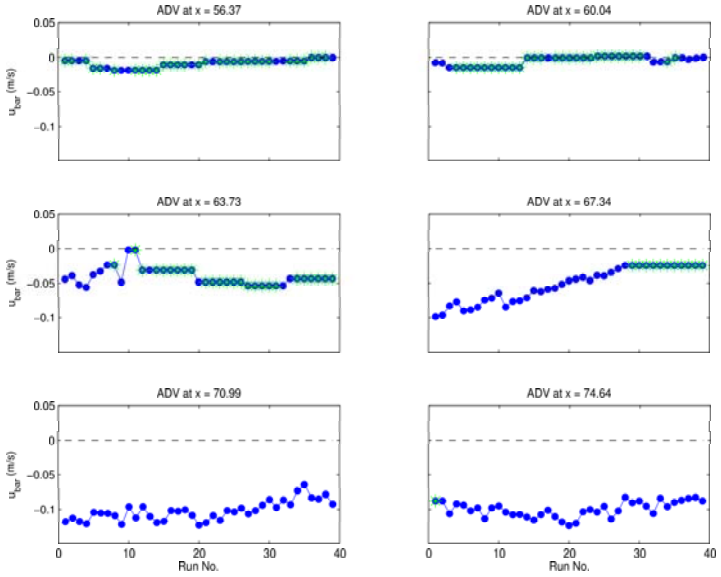

Fig. 5.9: *Onshore* migration - cross-shore mean velocity vs. run number for *alternative* replacement sequence of wall-mounted ADV's. Existing data (blue circles); replacement data (green stars)

Table 5.3: Model Predictive Skill Statistics for *Onshore* Migration *alternative replacement* database.

Acceleration-based	C_f	a_{crit}	K_a	RMS error	Skill
No Low-pass cutoff	0.001	0.2	3.0E-05	0.017	0.88
Instrument	0.003	0.2	3.0E-05	0.018	0.86
Locations	0.005	0.2	3.0E-05	0.02	0.79
	0.0065	0.1	1.0E-05	0.023	0.68
	0.010	0.1	1.0E-05	0.026	0.59

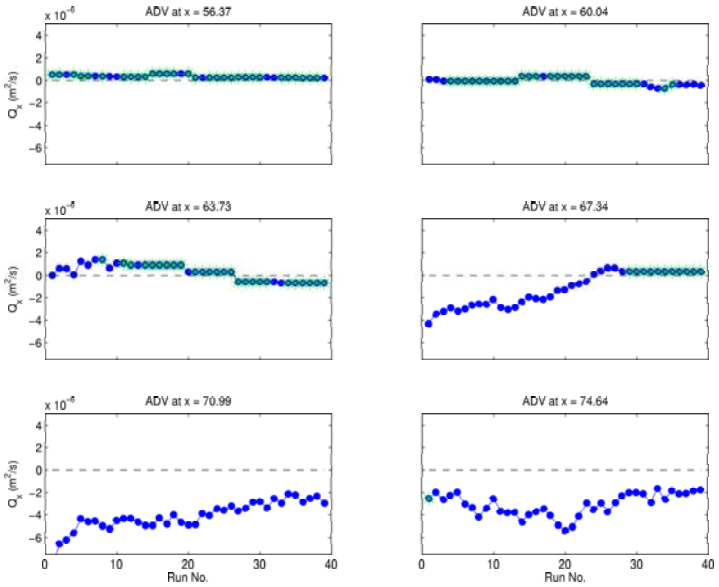

Fig. 5.10: *Onshore* migration - cross-shore sediment flux vs. run number for *alternative* replacement sequence of wall-mounted ADV's. Existing data (blue circles); replacement data (green stars)

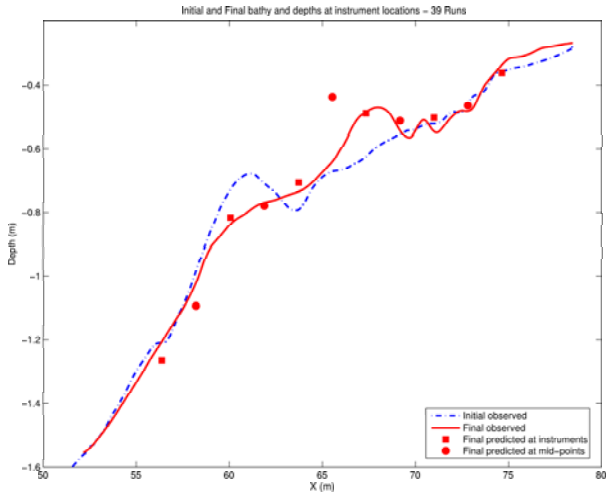

Fig. 5.11: *Onshore migration.* Acceleration-based model using the *alternative replacement* ADV database: initial observations (dashed), final observations (solid), and final predictions (squares and circles).

5.1.5 Alternative $\frac{dQ}{dx}$ Computations

Since the models in this report only compute bathymetric changes at specific locations, additional methods of computing the sediment flux gradients were examined in attempts to predict bathymetric change:

- Linear Interpolation
- Cubic Spline Interpolation
- PCHIP Spline Function (MATLAB routine)
- Smoothing Spline Routine (per S. Henderson)

All of these routines were applied using the computed sediment fluxes, Q_x, at the instrument locations. If accurate sediment flux gradients could be obtained at locations in between instruments, then, presumably, the bed change could be computed for all cross-shore locations, not just the instrument locations.

The linear interpolation routine computed, as the name suggests, the sediment flux gradients linearly, between instrument (or instrument mid-point) locations.

The cubic spline routine computed a piecewise polynomial fit through the data. The 'PCHIP' MATLAB routine computed a piecewise interpolation, as well, but preserved the shape of the function better because the sediment flux spatial series' were generally not smooth. PCHIP is different from a cubic spline because it does not require a continuous second derivative. However, it does not "overshoot" the data like the spline routine potentially does.

A smoothing spline routine (created by S. Henderson) computed a smoothed gradient function between the sediment fluxes. The extent to which the model "smooths" the data is user-selectable. At one extreme, the routine will predict a linear regression, at the other, a regression which intersects each sediment flux data point.

None of the interpolation routines improved predictions of the bed change significantly, or, if one did seem to improve predictions, its results were difficult to interpret for various reasons. For one, the linear interpolation created a step-function, more or less, due to its stepping nature; and the fact that gradients were assumed not to vary in between instrument locations. Prior to running this routine, it was evident that linear interpolation would not be an efficient measure of predicting bed change, but it was attempted anyways, as a method of comparing to the other interpolation methods.

The cubic spline, PCHIP and the smoothing spline routine appeared to predict the

bed change with more accuracy. The procedures updated the bathymetry at all interpolated locations. The concern with using any of these three methods, however, is that the behavior of the beach profile in between instrument locations is only estimated due to lack of observations. And, sand bars and troughs form where the observed sediment flux gradient is a maximum or minimum. These are points of convergence or divergence, but the model does not know where these locations are in the observations, it can only estimate their location.

Sediment transport models rely on the location of convergence or divergence to choose where to erode (or accrete) a bar, for instance. The spline interpolation routines, in efforts to fit the data as best as possible, may choose an incorrect location for the maximum or minimum in the sediment flux. When computed over several model runs sequentially, this can cause wildly different model predictions from the observations, forming bars or troughs, and predicting erosion or accretion where it was not observed.

6. CONCLUSIONS

A recent laboratory experiment has significantly augmented the number of available datasets of onshore bar migration. During the OHK portion of CROSSTEX, one offshore migration and two onshore bar migrations were observed under controlled laboratory conditions. The offshore migration occurred under higher wave energy conditions, representative of storm waves. The onshore migrations occurred under milder wave conditions, representative of post-storm recovery periods.

Two process-based sediment transport models (energetics (EM) and acceleration-based (AM)) were tested against the offshore migration and the first onshore migration datasets. The models were initialized with observed bathymetry and the change in elevation using observed velocity data was computed.

Two central difference methods for computing sediment flux gradients were described. The first method computed gradients at measurement locations, following previous sediment transport modeling efforts [*Gallagher et al.* (1998)]. The second method computed gradients in between measurement locations, and has a lower order of estimated error.

For the energetic waves during the offshore bar migration, the EM and AM models predicted very similar results. This was expected as the empirical extension in the AM model should not be actively contributing to the sediment flux during the highly energetic, erosive wave conditions. In this case, model predictive skills were low at the instrument locations but high at the instrument mid-point locations for both models.

When applied against the onshore migration dataset, the two models predicted remarkably different results. The energetics model did not predict erosion of an offshore bar, though it did predict slight accretion at the location of a newly formed onshore sandbar. On the other hand, the AM model accurately predicted the erosion of the offshore sandbar and the generation of the new sandbar shoreward, in accordance with the observations. Model predictive skills were generally higher at instrument locations and lower at instrument mid-point locations, in contrast to the findings from the offshore

dataset. Additionally, model skills increased greatly when the AM model was applied to the onshore migration.

The energetics model contained few free model parameters, and, thus, was relatively insensitive to variation of parameters. The AM model, however, contained several and was highly sensitive to variations in parameters due to its empirical nature. This was evidenced by the large range of best-fit free parameters found during the analysis of both the offshore and onshore migration events. Additionally, varying degrees of model predictive skill were observed.

Best-fit free parameters should be selected by tuning the model to the onshore migration case since these values predicted accurate bathymetric change for both the onshore and offshore cases. During energetic wave conditions, the acceleration-based model was relatively insensitive to varying free parameters. During milder wave conditions, however, the AM model was very sensitive to varying free parameters.

Selecting a different friction coefficient also had varying results on model predictions. The friction coefficient with the highest model predictive skill during energetic wave conditions was $C_f = 0.003$, in accordance with the value commonly used in recent modeling efforts [*Thornton et al.* (1996); *Gallagher et al.* (1998)]. During onshore migratory conditions, the model predictive skill was largest for small values of C_f (0.001 or 0.003). The skill levels decreased with increasing friction.

Furthermore, low-pass filtering of the velocity data prior to computing sediment transport had a significant effect on model predictions of the onshore sediment migration. The model skills decreased in the low-pass filtered predictions, implying that high-frequency noise in the data contributed largely to accurate model predictions. Conversely, low-pass filtering the offshore migration data had negligible effects on the model predictions. Model skills and best-fit free parameters were largely unchanged by low-pass filtering the offshore migration velocity data.

Finally, since both models were driven by the observed near-bottom velocities, different velocity databases caused variations in the predictive nature of the models. Noisy data files were replaced with adjacent 'clean' data files to alleviate any effects the noise had on predictions. An argument can be made in favor of replacing files in this manner

by assuming that the bathymetry did not change shape rapidly during the onshore migratory events. However, as was evident in the plots of mean velocities and predicted sediment fluxes versus time, the hydrodynamics tended to vary slightly from wave run to wave run. The assumption that the hydrodynamics at the measurement locations did not vary during the onshore bar migration may not be a valid assumption, after all.

As other researchers have found, model predictive skill is not always indicative of good model fit. When model skill is high (near a value of 1), it is a reliable delimiter, and implies accurate sediment transport prediction. However, when model skill is low (near zero) or even negative, the model results need to be interpreted with caution. There were several instances during this analysis in which model predictions were visually appealing yet had very low (or negative) skill values.

BIBLIOGRAPHY

Bagnold, R. A. (1963), *The Sea: Ideas and Observations*, vol. 3, chap. III. Sedimentation 21. Beach and Nearshore Processes Part I. Mechanics of Marine Sedimentation, pp. 507–528, Interscience.

Bagnold, R. A. (1966), An Approach to the Sediment Transport Problem From General Physics, *Geological Survey Professional Paper 422-I*, pp. I1–I37.

Bailard, J. A. (1981), An Energetics Total Load Sediment Transport Model for a Plane Sloping Beach, *Journal of Geophysical Research*, *86*(C11), 10,938–10,954.

Birkemeier, W. A. (1984), Time scales of profile change, in *Proceedings of the 19th International Coastal Engineering Conference*, pp. 1507–1521, American Society of Civil Engineers, New York.

Bowen, A. J. (1980), Simple Models of Nearshore Sedimentation; Beach Profiles and Longshore Bars, *The Coastline of Canada; Geological Survey of Canada*, *Paper 80-10*, 1–11.

Bruun, P. (1954), Coast Erosion and the Development of Beach Profiles, *Tech. Rep. 44*, U.S. Army Corps of Engineers, Beach Erosion Board.

Bunt, J. A. C., P. Larcombe, and C. F. Jago (1999), Quantifying the Response of Optical Backscatter Devices and Transmissometers to Variations in Suspended Particulate Matter, *Continental Shelf Research*, *19*, 1199–1220.

Church, J. C., and E. B. Thornton (1993), Effects of breaking wave induced turbulence within a longshore current model, *Coastal Engineering*, *20*, 1–28.

Conner, C. S., and A. M. De Visser (1992), A Laboratory Investigation of Particle Size Effects on an Optical Backscatterance Sensor, *Marine Geology*, *108*, 151–159.

D&A (1991), *Instruction Manual OBS-3 Suspended Solids and Turbidity Monitor*, D & A Instrument Company.

Dean, R. G. (1973), Heuristic models of sand transport in the surf zone, in *Conference on Engineering Dynamics in the Surfzone*, p. 7, Sydney, N. S. W.

Dean, R. G. (1977), Equilibrium beach profiles: U.s. atlantic and gulf coasts, *Tech. Rep. Ocean Engineering Report No. 12*, Dept. of Civil Engineering, University of Delaware.

Dean, R. G., and R. A. Dalrymple (2002), *Coastal Processes with Engineering Applications*, Cambridge University Press.

Downing, J. P., and R. A. Beach (1989), Laboratory Apparatus for Calibrating Optical Suspended Solids Sensors, *Marine Geology*, *86*, 243–249.

Drake, T. G., and J. Calantoni (2001), Discrete Particle Model for Sheet Flow Sediment Transport in the Nearshore, *Journal of Geophysical Research*, *106*(C9), 19,859–19,868.

Elgar, S., E. L. Gallagher, and R. T. Guza (2001), Nearshore Sandbar Migration, *Journal of Geophysical Research*, *106*(C6), 11,623–11,627.

Gallagher, E. L., S. Elgar, and R. T. Guza (1998), Observations of Sand Bar Evolution on a Natural Beach, *Journal of Geophysical Research*, *103*(C2), 3203–3215.

Goring, D. G., and V. I. Nikora (2002), Despiking Acoustic Doppler Velocimeter Data, *Journal of Hydraulic Engineering*, *128*(1), 117–126.

Greenwood, B., and R. G. D. Davisdon-Arnott (1979), Sedimentation and equilibrium in wave-formed bars: a review and case studies, *Canadian Journal of Earth Sciences*, *16*, 312–332.

Henderson, S. M., J. S. Allen, and P. A. Newberger (2004), Nearshore Sandbar Migration Predicted by an Eddy-Diffusive Boundary Layer Model, *Journal of Geophysical Research*, *109*(C06024), doi:10.1029/2003JC002137.

Hoefel, F., and S. Elgar (2003), Wave-Induced Sediment Transport and Sandbar Migration, *Science*, *299*, 1885–1887.

Kennedy, A. B., Q. Chen, J. T. Kirby, and R. A. Dalrymple (2000), Boussinesq modeling of wave transformation: Breaking and runup. i:1d, *Journal of Waterway, Port, Coastal and Ocean Engineering*, *126*(1), 39–47.

King, C. A. M., and W. W. Williams (1949), The Formation and Movement of Sand Bars by Wave Action, *Geographical Journal*, *113*, 70–85.

Kraus, N. C., and J. M. Smith (1994), Supertank laboratory data collection, volumes i & ii, *Tech. Rep. CERC-94-3*, US Army Corps of Engineers.

Kraus, N. C., M. Larson, and D. L. Kriebel (1991), Evaluation of Beach Erosion and Accretion Predictors, in *Coastal Sediments '91*, pp. 572 – 587.

Larson, M., and N. C. Kraus (1989), SBEACH: Numerical Model for Simulating Storm-Induced Beach Change: Report 1, *Technical Report CERC-89-9*, pp. 1–256.

Lippmann, T. C., and R. A. Holman (1990), The spatial and temporal variability of sand bar morphology, *Journal of Geophysical Research*, *95*(C7), 11,575–11,590.

Lynch, J. F., J. D. Irish, C. R. Sherwood, and Y. C. Agrawal (1994), Determining Suspended Sediment Particle Size Information from Acoustical and Optical Backscatter Measurements, *Continental Shelf Research*, *14*(10/11), 1139–1165.

Miller, R. L. (1976), Role of vortices in surf zone prediction: sedimentation and wave forces, *Beach and Nearshore Sedimentation, Society of Economic Paleontologists and Mineralologists*, *Special Publication 24*, 92–114.

Nortek (2004), *Vectrino Velocimeter - User's Manual*, Nortek AS.

Plant, N. G., K. T. Holland, J. Puleo, and E. L. Gallagher (2004), Prediction Skill of Nearshore Profile Evolution Models, *Journal of Geophysical Research*, *109*(C01006), doi:10.1029/2003JC001995.

Roelvink, J. A., and I. Brøker (1993), Cross-shore Profile Models, *Coastal Engineering*, *21*, 163–191.

Roelvink, J. A., and A. J. H. M. Reniers (1995), Lip 11d delta flume experiments: a dataset for profile evolution model validation, *Tech. Rep. H2130*, Delft University of Hydraulics.

Ruggiero, P., G. M. Kaminsky, G. Gelfenbaum, and B. Voigt (2005), Seasonal to interannual morphodynamics along a high-energy dissipative littoral cell, *Journal of Coastal Research*, *21*(3), 553–578.

Ruggiero, P., D. Walstra, G. Lesser, and G. Gelfenbaum (2006), Seasonal-scale nearshore morphological evolution, *Eos Trans. AGU*, *87*(36), Ocean Sci. Meet. Suppl., Abstract OS52E–03.

Sallenger, A. H., R. A. Holman, and W. A. Birkemeier (1985), Storm-Induced Response of a Nearshore-Bar System, *Marine Geology*, *64*, 237–257.

Sutherland, T. F., P. M. Lane, C. L. Amos, and J. Downing (2000), The Calibration of Optical Backscatter Sensors for Suspended Sediment of Varying Darkness Levels, *Marine Geology*, *162*, 587–597.

Thornton, E. B., R. T. Humiston, and W. Birkemeier (1996), Bar/Trough Generation on a Natural Beach, *Journal of Geophysical Research*, *101*(C5), 12,097–12,110.

Trowbridge, J., and D. Young (1989), Sand Transport by Unbroken Water Waves Under Sheet Flow Conditions, *Journal of Geophysical Research*, *94*(C8), 10,971–10,991.

Wright, L., and A. D. Short (1984), Morphodynamic Variability of Surf Zones and Beaches: A Synthesis, *Marine Geology*, *56*, 93–118.

APPENDIX

A. WAVE CASE STATISTICS

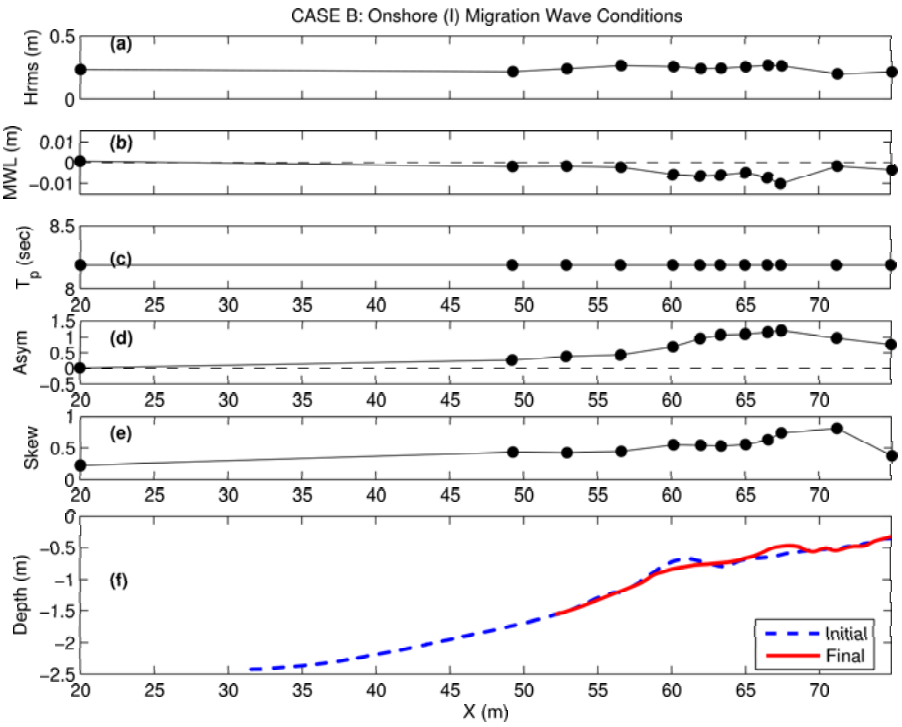

Fig. A.1: Wave case B: *onshore I* bar migration (a) H_{rms}, (b) mean water level, (c) peak period, (d) wave asymmetry and (e) wave skewness vs. cross-shore location averaged over all CASE B wave runs. (f) initial and final bathymetries.

Table A.1: CASE B Wave Statistics

	WG 1	WG 2	WG 3	WG 4	WG 5	WG 6
Hrms (m)	0.23	0.22	0.24	0.27	0.26	0.24
MWL (m)	0.001	-0.002	-0.002	-0.002	-0.006	-0.007
Tp (sec)	8.19	8.19	8.19	8.19	8.19	8.19
Asym	0.01	0.26	0.38	0.43	0.69	0.96
Skew	0.22	0.43	0.42	0.44	0.55	0.54

	WG 7	WG 8	WG 9	WG 10	WG 11	WG 12
Hrms (m)	0.25	0.26	0.27	0.26	0.20	0.22
MWL (m)	-0.006	-0.005	-0.007	-0.010	-0.002	-0.004
Tp (sec)	8.19	8.19	8.19	8.19	8.19	8.19
Asym	1.07	1.10	1.15	1.20	0.97	0.76
Skew	0.53	0.55	0.63	0.74	0.81	0.37

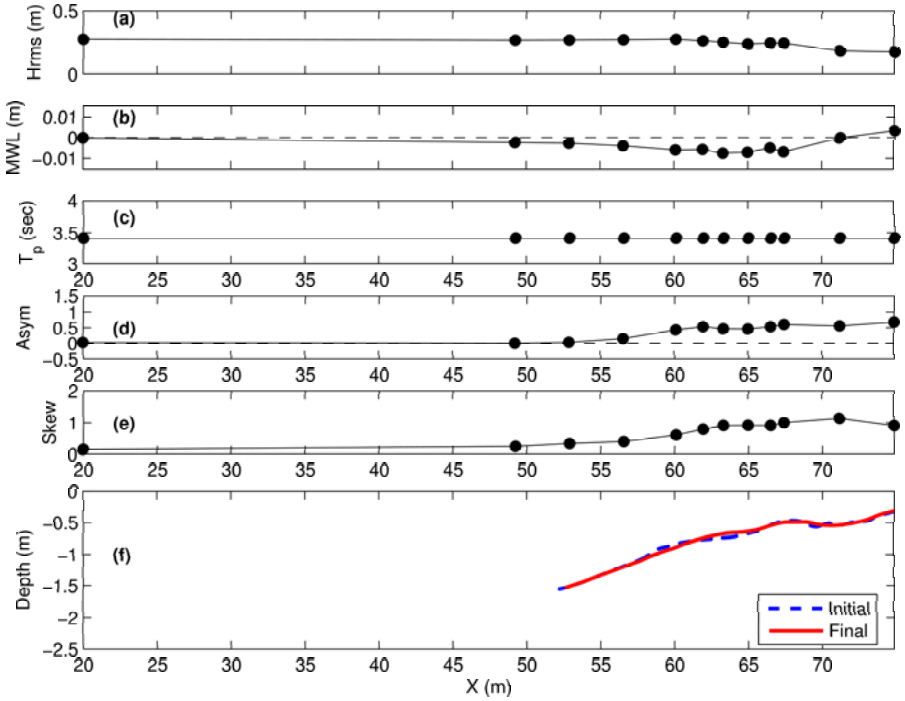

Fig. A.2: Wave case C: *intermediary* bar migration (a) H_{rms}, (b) mean water level, (c) peak period, (d) wave asymmetry and (e) wave skewness vs. cross-shore location averaged over all CASE C wave runs of $T_p = 3.5$ seconds. (f) initial and final bathymetries.

Table A.2: CASE C Wave Statistics

	WG 1	WG 2	WG 3	WG 4	WG 5	WG 6
Hrms (m)	0.28	0.27	0.27	0.27	0.28	0.27
MWL (m)	0.000	-0.002	-0.003	-0.004	-0.006	-0.006
Tp (sec)	3.41	3.41	3.41	3.41	3.41	3.41
Asym	0.02	0.00	0.03	0.15	0.43	0.53
Skew	0.14	0.24	0.33	0.39	0.60	0.79

	WG 7	WG 8	WG 9	WG 10	WG 11	WG 12
Hrms (m)	0.25	0.24	0.25	0.25	0.18	0.18
MWL (m)	-0.008	-0.007	-0.005	-0.007	0.000	0.003
Tp (sec)	3.41	3.41	3.41	3.41	3.41	3.41
Asym	0.46	0.46	0.53	0.60	0.55	0.68
Skew	0.91	0.92	0.91	1.00	1.14	0.91

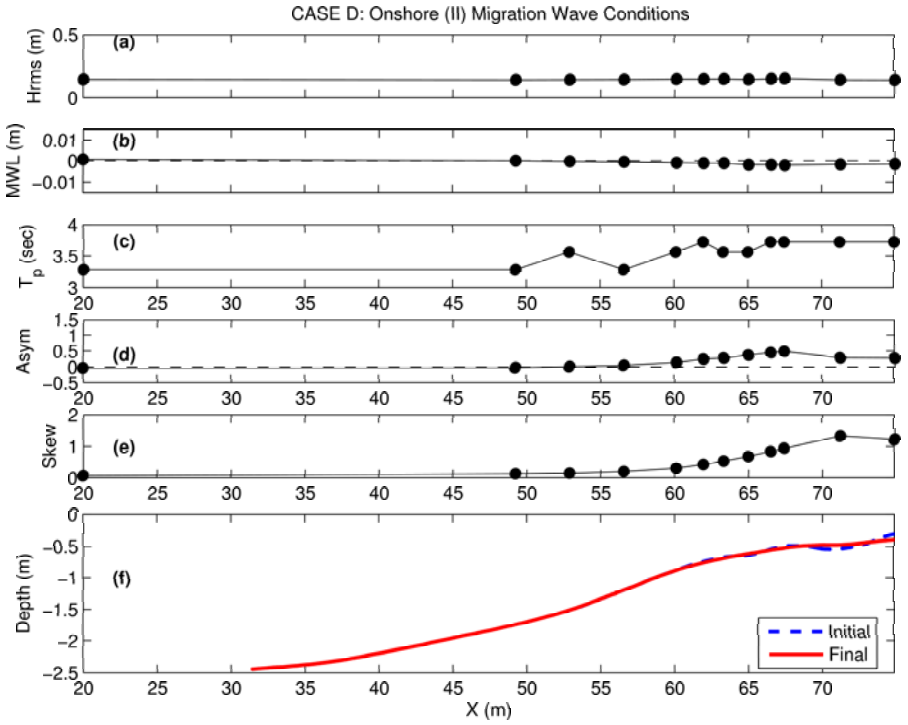

Fig. A.3: Wave case D: *onshore II* bar migration (a) H_{rms}, (b) mean water level, (c) peak period, (d) wave asymmetry and (e) wave skewness vs. cross-shore location averaged over all CASE D wave runs. (f) initial and final bathymetries.

Table A.3: CASE D Wave Statistics

	WG 1	WG 2	WG 3	WG 4	WG 5	WG 6
Hrms (m)	0.14	0.14	0.14	0.14	0.15	0.15
MWL (m)	0.001	0.000	0.000	-0.001	-0.001	-0.001
Tp (sec)	3.28	3.28	3.56	3.28	3.56	3.72
Asym	-0.03	-0.03	0.01	0.05	0.14	0.24
Skew	0.06	0.13	0.15	0.20	0.30	0.43

	WG 7	WG 8	WG 9	WG 10	WG 11	WG 12
Hrms (m)	0.15	0.14	0.15	0.15	0.14	0.14
MWL (m)	-0.001	-0.002	-0.002	-0.002	-0.002	-0.001
Tp (sec)	3.56	3.56	3.72	3.72	3.72	3.72
Asym	0.28	0.37	0.45	0.48	0.28	0.27
Skew	0.53	0.68	0.83	0.93	1.31	1.21

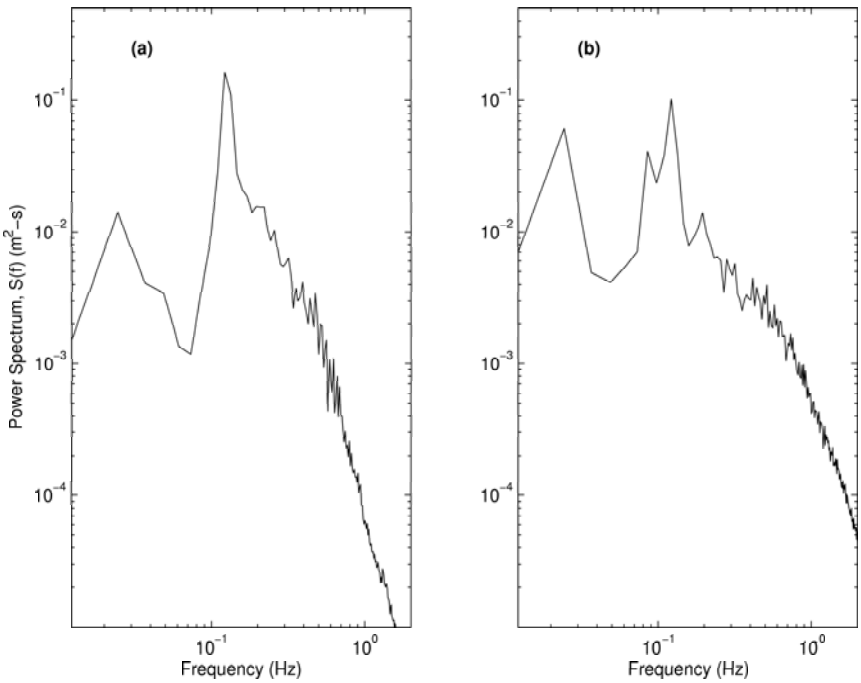

Fig. A.4: Wave case B: *onshore I* bar migration (a) Wave spectra from wave gauge 1 (Bay 20), (b) Wave spectra from wave gauge 12 (Bay 5).

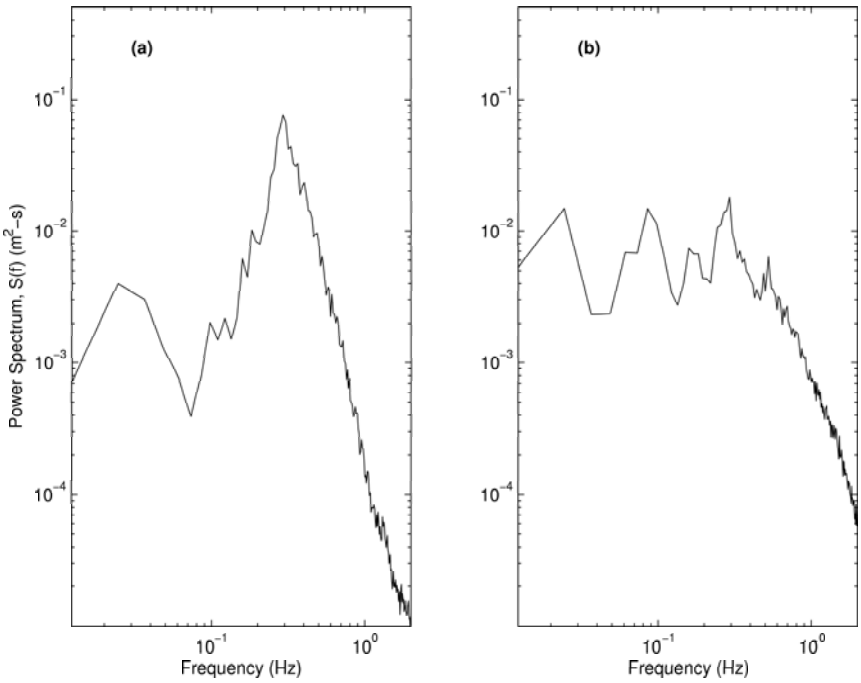

Fig. A.5: Wave case C: *intermediary* bar migration (a) Wave spectra from wave gauge 1 (Bay 20), (b) Wave spectra from wave gauge 12 (Bay 5).

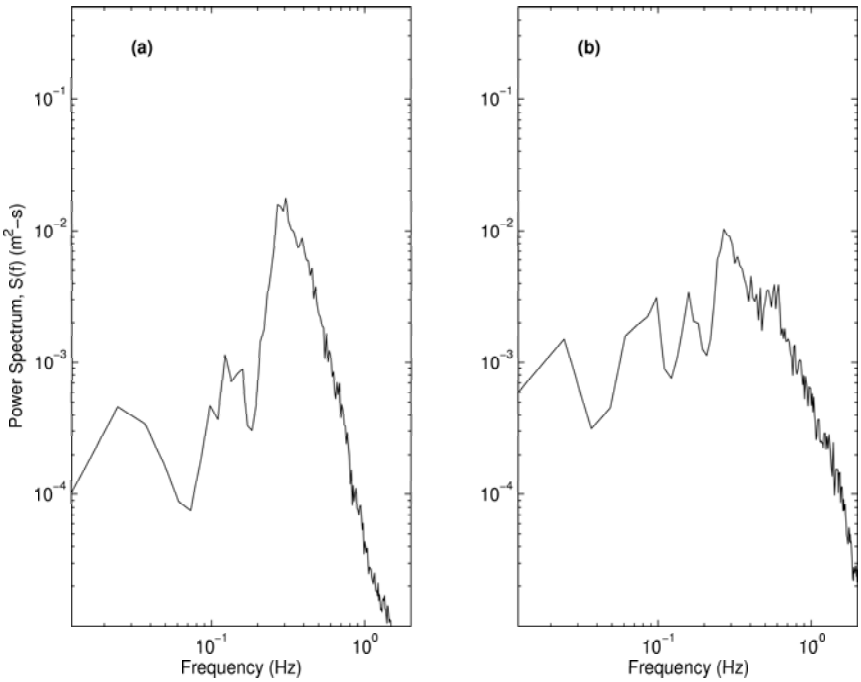

Fig. A.6: Wave case D: *onshore II* bar migration (a) Wave spectra from wave gauge 1 (Bay 20), (b) Wave spectra from wave gauge 12 (Bay 5).

B. VELOCITY STATISTIC COMPARISONS

As stated in the report, nearly all of the wall-mounted ADV velocity data from the *offshore* migration case were suitable to use. The last two wave runs at the Bay 9 location were the only ones that required replacement. They were replaced with the Bay 9 ADV files from model run 12.

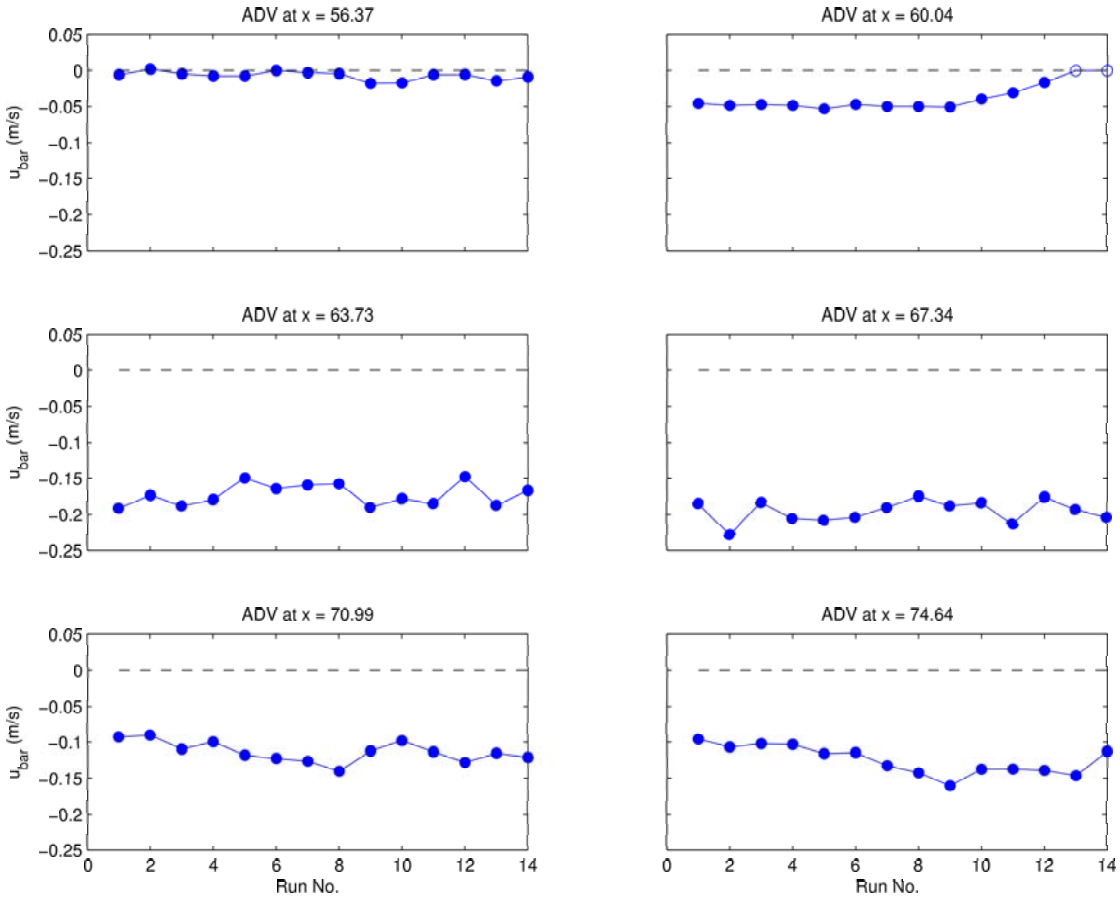

Fig. B.1: *Offshore* Migration - Mean cross-shore velocity vs. run number for *original* sequence of wall-mounted ADV's. Clean data (solid); Suspect data (open).

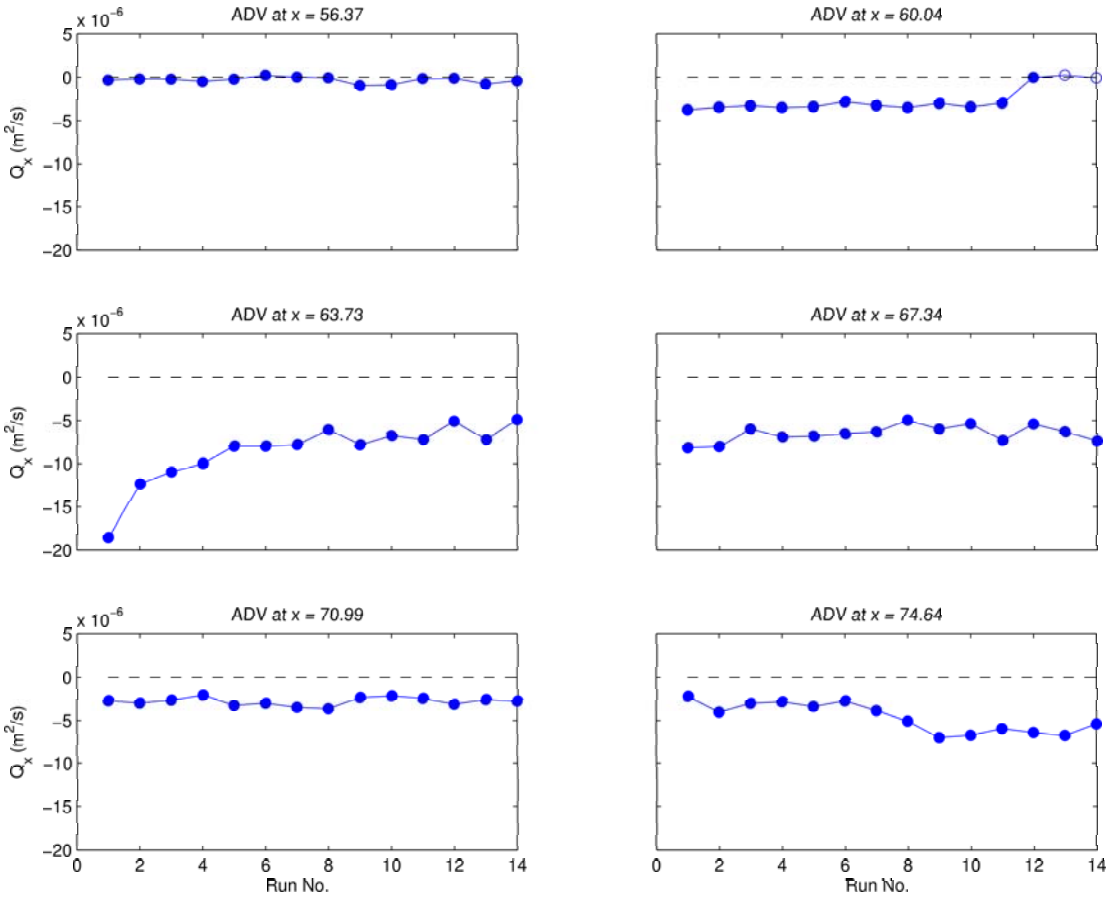

Fig. B.2: *Offshore* Migration **-** Cross-shore sediment flux vs. run number for cross-shore velocity of *original* sequence of wall-mounted ADV's. Clean data (solid); Suspect data (open)**.**

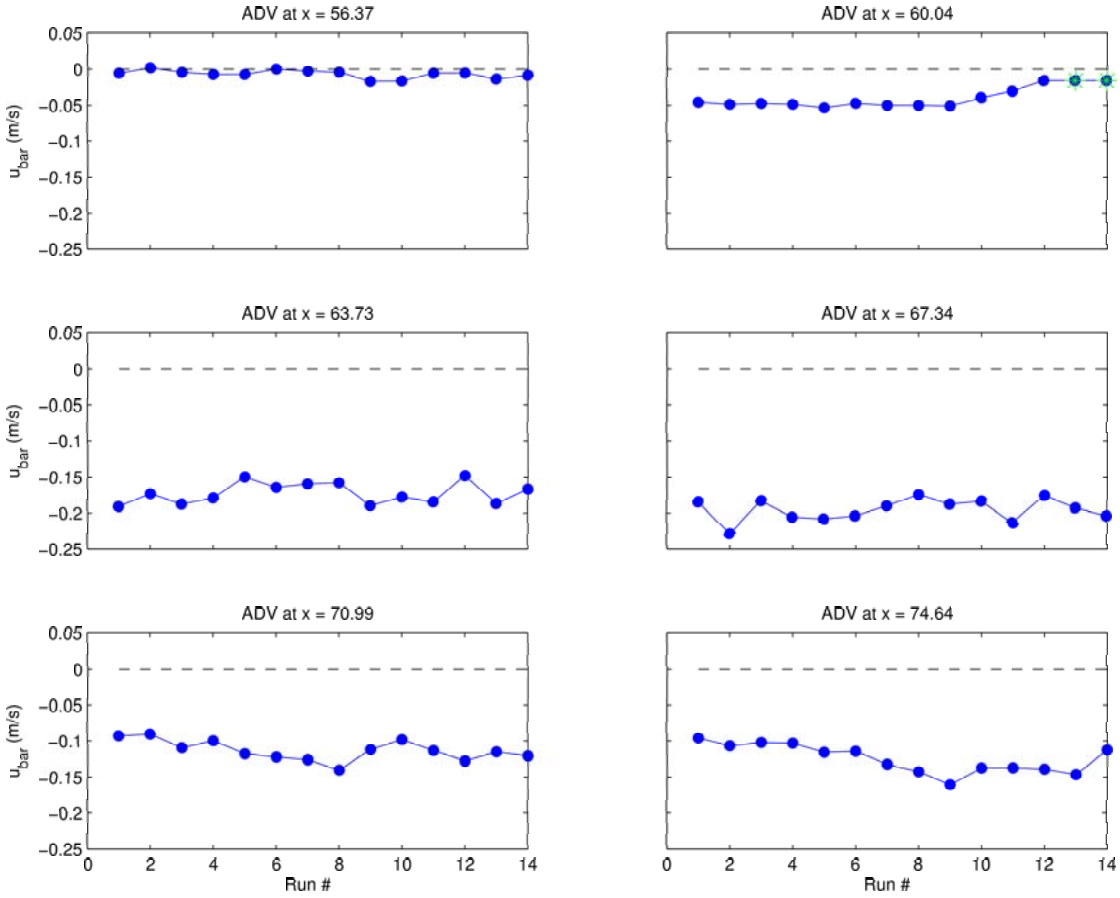

Fig. B.3: *Offshore* Migration - Mean cross-shore velocity vs. run number for *replacement* sequence of wall-mounted ADV's. Existing data (blue circles); Replacement data (green stars)

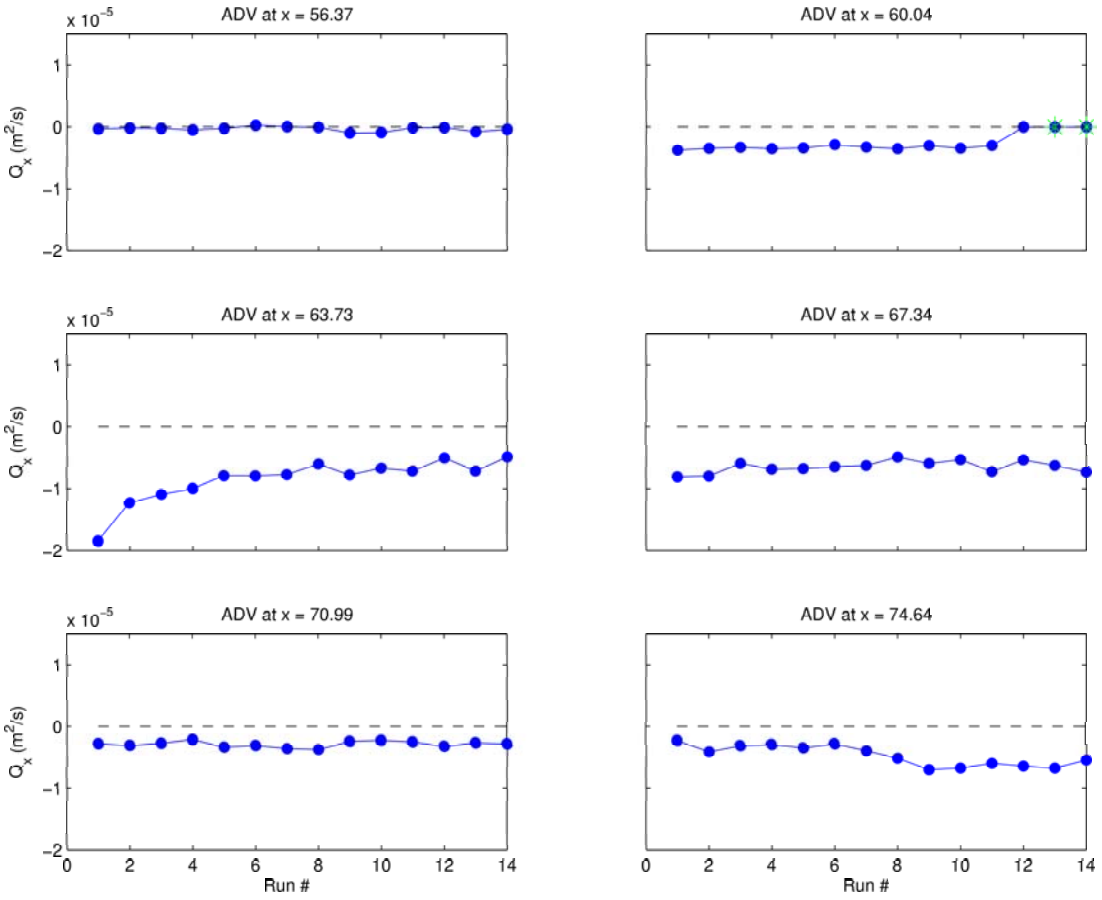

Fig. B.4: *Offshore* Migration **-** Cross-shore sediment flux vs. run number for *replacement* sequence of wall-mounted ADV's. Existing data (blue circles); Replacement data (green stars)

C. MODEL DATABASES

C.1 Survey Databases

The following tables list the MTA and manual survey files used for the CROSSTEX analysis for the respective offshore and onshore migration cases. The run numbers used in these tables correspond to the run numbers used for modeling purposes, and are different from the run numbers used during CROSSTEX. Run 0 corresponds to the initial bathymetry used to initialize the sediment transport models. Run entries denoted by a '-' act as a flag for entries in which ADV velocity data did not exist. DAQ entries denoted by a '-' act as a flag for entried in which wave data did not exist. Additional descriptions are in the last column on the right.

Table C.1: *Offshore* Migration Survey Database

Model Run	DAQ Prefix	MTA Survey Filename	Manual Survey Filename	Migration
0	**-**	survey_082205_1215.txt	hand_survey_082005_1530.txt	**Initial Bathymetry**
1	235.8157_	survey_082305_1510.txt	hand_survey_082305_1510.txt	**Offshore Migration**
2	235.9670_	survey_082305_1700.txt	hand_survey_082305_1700.txt	↓
3	236.7079_	survey_082405_1055.txt	hand_survey_082405_1055.txt	
4	236.7847_	survey_082405_1219.txt	hand_survey_082405_1219.txt	↓
5	236.8328_	survey_082405_1401.txt	hand_survey_082405_1401.txt	
6	236.8965_	survey_082405_1510.txt	hand_survey_082405_1510.txt	↓
7	236.9550_	survey_082405_1641.txt	hand_survey_082405_1641.txt	
8	237.0193_	survey_082405_1820.txt	hand_survey_082405_1820.txt	↓
9	237.7501_	survey_082505_1151.txt	hand_survey_082505_1151.txt	
10	237.8018_	survey_082505_1248.txt	hand_survey_082505_1248.txt	↓
11	237.8849_	survey_082505_1445.txt	hand_survey_082505_1445.txt	
12	237.9353_	survey_082505_1552.txt	hand_survey_082505_1552.txt	↓
13	237.9770_	survey_082505_1655.txt	hand_survey_082505_1655.txt	
14	238.0305_	survey_082605_0825.txt	hand_survey_082605_0825.txt	**Offshore Migration**

Table C.2: *Onshore* Migration Survey Database

Model Run	DAQ Prefix	MTA Survey Filename	Manual Survey Filename	Migration
0	-	survey_082605_0825.txt	hand_survey_082605_0825.txt	**Initial Bathymetry**
-	238.7042_	survey_082605_1023.txt	hand_survey_082605_1023.txt	**No Velocity Data**
1	-	survey_082605_1120.txt	hand_survey_082605_1120.txt	**No Wave Data**
2	238.9122_	survey_082605_1518.txt	hand_survey_082605_1518.txt	**Onshore Migration**
3	238.9462_	survey_082605_1607.txt	hand_survey_082605_1607.txt	
4	238.9803_	survey_082905_2120.txt	hand_survey_082605_1710.txt	↓
5	242.6641_	survey_083005_0924.txt	hand_survey_083005_0924.txt	
6	242.7021_	survey_083005_1016.txt	hand_survey_083005_1016.txt	↓
-	242.7375_	survey_083005_1108.txt	hand_survey_083005_1108.txt	**No Velocity Data**
7	242.8084_	survey_083005_1254.txt	hand_survey_083005_1254.txt	↓
8	242.8482_	-	-	
9	242.8776_	survey_083005_1430.txt	hand_survey_083005_1430.txt	↓
10	242.9129_	-	-	
11	242.9457_	survey_083005_1608.txt	hand_survey_083005_1608.txt	↓
12	242.9875_	-	-	
13	243.0342_	survey_083005_1812.txt	hand_survey_083005_1812.txt	↓
14	243.6424_	-	-	
15	243.6680_	survey_083105_0931.txt	hand_survey_083105_0931.txt	↓
16	243.8442_	-	-	
17	243.8672_	survey_083105_1415.txt	hand_survey_083105_1415.txt	↓
18	243.8997_	-	-	
19	243.9198_	survey_083105_1555.txt	hand_survey_083105_1555.txt	↓
20	243.9704_	-	-	
21	243.9936_	survey_083105_1716.txt	hand_survey_083105_1716.txt	↓
22	244.0523_	-	-	
23	244.6576_	survey_090105_0914.txt	hand_survey_090105_0914.txt	↓
24	244.7075_	-	-	
25	244.7289_	survey_090105_1057.txt	hand_survey_090105_1157.txt	↓
26	244.7757_	-	-	
27	244.7973_	survey_090105_1232.txt	hand_survey_090105_1232.txt	↓
28	244.8815_	survey_090105_1428.txt	hand_survey_090105_1428.txt	
		-Continued Onshore Migration with New Wave Condition-		
29	244.9106_	survey_090105_1518.txt	hand_survey_090105_1518.txt	**Onshore Migration**
30	244.9446_	-	-	↓
31	244.9692_	survey_090105_1641.txt	hand_survey_090105_1641.txt	
32	245.6533_	-	-	↓
33	245.6769_	survey_090205_0937.txt	hand_survey_090205_0937.txt	
34	-	-	-	No Wave Data

Continued on next page

Table C.2: (continued)

Model Run	DAQ Prefix	MTA Survey Filename	Manual Survey Filename	Migration
35	245.7712_	survey_090205_1154.txt	hand_survey_090205_1154.txt	↓
36	245.8260_	-	-	
37	245.8493_	survey_090205_1346.txt	hand_survey_090205_1346.txt	↓
38	245.8802_	-	-	
39	245.9070_	survey_090205_1507.txt	hand_survey_090205_1545.txt	**Onshore Migration**

C.2 ADV Databases

The following tables list the ADV files that were used to model sediment transport as described in this report (Section 3). In order for the databases to fit on the pages, the 6 columns that denote the cross-shore wall-mounted instruments were separated into 2 databases of 3 columns each. Bays 10-5 correspond to the ADV's in Ports: [1 2 3 6 7 8], as described in Appendix D. The ascii text files are listed here in order of Bay number (10-5, offshore to onshore) without the '*.txt*' extension.

Table C.3: *Offshore* Migration Velocimeter Database

Model Run	Bay 10	Bay 9	Bay 8
1	0823R05_VelWallADV1	0823R05_VelWallADV2	0823R05_VelWallADV3
2	0823R06_VelWallADV1	0823R06_VelWallADV2	0823R06_VelWallADV3
3	0824R01_VelWallADV1	0824R01_VelWallADV2	0824R01_VelWallADV3
4	0824R03_VelWallADV1	0824R03_VelWallADV2	0824R03_VelWallADV3
5	0824R04_VelWallADV1	0824R04_VelWallADV2	0824R04_VelWallADV3
6	0824R05_VelWallADV1	0824R05_VelWallADV2	0824R05_VelWallADV3
7	0824R06_VelWallADV1	0824R06_VelWallADV2	0824R06_VelWallADV3
8	0824R07_VelWallADV1	0824R07_VelWallADV2	0824R07_VelWallADV3
9	0825R01_VelWallADV1	0825R01_VelWallADV2	0825R01_VelWallADV3
10	0825R02_VelWallADV1	0825R02_VelWallADV2	0825R02_VelWallADV3
11	0825R03_VelWallADV1	0825R03_VelWallADV2	0825R03_VelWallADV3
12	0825R04_VelWallADV1	0825R04_VelWallADV2	0825R04_VelWallADV3
13	0825R05_VelWallADV1	↓	0825R05_VelWallADV3
14	0825R06_VelWallADV1	↓	0825R06_VelWallADV3

Model Run	Bay 7	Bay 6	Bay 5
1	0823R05_VelWallADV6	0823R05_VelWallADV7	0823R05_VelWallADV8
2	0823R06_VelWallADV6	0823R06_VelWallADV7	0823R06_VelWallADV8
3	0824R01_VelWallADV6	0824R01_VelWallADV7	0824R01_VelWallADV8
4	0824R03_VelWallADV6	0824R03_VelWallADV7	0824R03_VelWallADV8
5	0824R04_VelWallADV6	0824R04_VelWallADV7	0824R04_VelWallADV8
6	0824R05_VelWallADV6	0824R05_VelWallADV7	0824R05_VelWallADV8
7	0824R06_VelWallADV6	0824R06_VelWallADV7	0824R06_VelWallADV8
8	0824R07_VelWallADV6	0824R07_VelWallADV7	0824R07_VelWallADV8
9	0825R01_VelWallADV6	0825R01_VelWallADV7	0825R01_VelWallADV8
10	0825R02_VelWallADV6	0825R02_VelWallADV7	0825R02_VelWallADV8

Continued on next page

Table C.3: (continued)

11	0825R03_VelWallADV6	0825R03_VelWallADV7	0825R03_VelWallADV8
12	0825R04_VelWallADV6	0825R04_VelWallADV7	0825R04_VelWallADV8
13	0825R05_VelWallADV6	0825R05_VelWallADV7	0825R05_VelWallADV8
14	0825R06_VelWallADV6	0825R06_VelWallADV7	0825R06_VelWallADV8

Table C.4: *onshore* migration Velocimeter database

Model Run	Bay 10	Bay 9	Bay 8
1	↑	0826R05_VelWallADV2	0826R05_VelWallADV3
2	↑	0826R06_VelWallADV2	0826R06_VelWallADV3
3	0826R07_VelWallADV1	0826R07_VelWallADV2	0826R07_VelWallADV3
4	↓	↓	0826R08_VelWallADV3
5	↑	↓	0830R01_VelWallADV3
6	↑	↓	0830R02_VelWallADV3
7	0830R08_VelWallADV1	↓	0830R08_VelWallADV3
8	↑	↓	↓
9	0830R10_VelWallADV1	↓	0830R10_VelWallADV3
10	0830R11_VelWallADV1	↓	0830R11_VelWallADV3
11	↓	↑	↓
12	↓	↑	↑
13	↓	↑	0830R15_VelWallADV3
14	↓	**0831R01_VelCartADV3**	↓
15	↑	↓	**0831R02_VelCartADV2**
16	↑	↓	↓
17	↑	0831R07_VelWallADV2	↓
18	↑	↓	↓
19	0831R09_VelWallADV1	↓	↓
20	↓	↓	0831R12_VelWallADV3
21	↑	↓	↓
22	0831R15_VelWallADV1	↓	↓
23	↓	↓	↓
24	↓	↑	↓
25	**0901R03_VelCartADV2**	↑	↓
26	↓	**0901R04_VelCartADV2**	↓
27	↓	↓	**0902R05_VelCartADV2**
28	↓	↓	↓
29	↓	↓	↓
30	↓	↓	↓
31	0901R11_VelWallADV1	0901R11_VelWallADV2	↓
32	0902R01_VelWallADV1	0902R01_VelWallADV2	0902R01_VelWallADV3
33	↓	0902R02_VelWallADV2	0902R02_VelWallADV3
34	↓	↓	↓
35	↓	↑	↓
36	↑	0902R06_VelWallADV2	↓
37	↑	0902R07_VelWallADV2	↓
38	↑	0902R08_VelWallADV2	↓

Continued on next page

Table C.4: (continued)

39	0902R09_VelWallADV1	0902R09_VelWallADV2	↓

Model Run	Bay 7	Bay 6	Bay 5
1	0826R05_VelWallADV6	0826R05_VelWallADV7	0826R06_VelWallADV8
2	0826R06_VelWallADV6	0826R06_VelWallADV7	0826R06_VelWallADV8
3	0826R07_VelWallADV6	0826R07_VelWallADV7	0826R07_VelWallADV8
4	0826R08_VelWallADV6	0826R08_VelWallADV7	0826R08_VelWallADV8
5	0830R01_VelWallADV6	0830R01_VelWallADV7	0830R01_VelWallADV8
6	0830R02_VelWallADV6	0830R02_VelWallADV7	0830R02_VelWallADV8
7	0830R08_VelWallADV6	0830R08_VelWallADV7	0830R08_VelWallADV8
8	0830R09_VelWallADV6	0830R09_VelWallADV7	0830R09_VelWallADV8
9	0830R10_VelWallADV6	0830R10_VelWallADV7	0830R10_VelWallADV8
10	0830R11_VelWallADV6	0830R11_VelWallADV7	0830R11_VelWallADV8
11	0830R12_VelWallADV6	0830R12_VelWallADV7	0830R12_VelWallADV8
12	0830R13_VelWallADV6	0830R13_VelWallADV7	0830R13_VelWallADV8
13	0830R15_VelWallADV6	0830R15_VelWallADV7	0830R15_VelWallADV8
14	0831R01_VelWallADV6	0831R01_VelWallADV7	0831R01_VelWallADV8
15	0831R02_VelWallADV6	0831R02_VelWallADV7	0831R02_VelWallADV8
16	0831R06_VelWallADV6	0831R06_VelWallADV7	0831R06_VelWallADV8
17	0831R07_VelWallADV6	0831R07_VelWallADV7	0831R07_VelWallADV8
18	0831R08_VelWallADV6	0831R08_VelWallADV7	0831R08_VelWallADV8
19	0831R09_VelWallADV6	0831R09_VelWallADV7	0831R09_VelWallADV8
20	0831R12_VelWallADV6	0831R12_VelWallADV7	0831R12_VelWallADV8
21	0831R13_VelWallADV6	0831R13_VelWallADV7	0831R13_VelWallADV8
22	0831R15_VelWallADV6	0831R15_VelWallADV7	0831R15_VelWallADV8
23	0901R01_VelWallADV6	0901R01_VelWallADV7	0901R01_VelWallADV8
24	0901R02_VelWallADV6	0901R02_VelWallADV7	0901R02_VelWallADV8
25	0901R03_VelWallADV6	0901R03_VelWallADV7	0901R03_VelWallADV8
26	0901R04_VelWallADV6	0901R04_VelWallADV7	0901R04_VelWallADV8
27	0901R05_VelWallADV6	0901R05_VelWallADV7	0901R05_VelWallADV8
28	0901R08_VelWallADV6	0901R08_VelWallADV7	0901R08_VelWallADV8
29	↓	0901R09_VelWallADV7	0901R09_VelWallADV8
30	↓	0901R10_VelWallADV7	0901R10_VelWallADV8
31	↓	0901R11_VelWallADV7	0901R11_VelWallADV8
32	↓	0902R01_VelWallADV7	0902R01_VelWallADV8
33	↓	0902R02_VelWallADV7	0902R02_VelWallADV8
34	**0902R04_VelCartADV2**	0902R04_VelWallADV7	0902R04_VelWallADV8
35	↓	0902R05_VelWallADV7	0902R05_VelWallADV8
36	↓	0902R06_VelWallADV7	0902R06_VelWallADV8

Continued on next page

Table C.4: (continued)

37	↓	0902R07_VelWallADV7	0902R07_VelWallADV8
38	↓	0902R08_VelWallADV7	0902R08_VelWallADV8
39	↓	0902R09_VelWallADV7	0902R09_VelWallADV8

D. LWF COORDINATE SYSTEM

D.1 LWF Origin

The cross-shore origin of the LWF coordinate system (LWFCS) is at waveboard zero (where the waveboard is vertical). The vertical origin is at the top of the east wall of the LWF. The alongshore origin in this report is the inside edge of the east LWF wall. Positive directions follow a right-handed coordinate system. *Note: Though all vertical locations are given in this coordinate system, plots will typically show the SWL as* $Z = 0$.

Not all positioning measurements provided below are in the LWFCS. Some require a quick conversion. If measurements below are not given in the LWFCS a conversion is provided. The following sections provide all necessary details regarding the coordinate system and location of instruments within it.

D.2 Cross-shore (wall-mounted) Instrument Locations

The locations of the *cross-shore array* of instruments are provided in the LWFCS. Two tables of coordinates exist for the wall- and carriage-mounted instruments because three ADV's were replaced during the experiment. On 08/29/2005, the three ADV probes on the Bay 8 wallplate were replaced. The DAQ port number and respective ADV numbers (prior to and following the changeout) are given in Table D.1. Coordinates for all of the wall-mounted instruments are provided in Tables D.2 and D.3. *Note: Cross-shore locations are provided in meters. Alongshore and vertical locations are provided in centimeters.*

The cross-shore and alongshore locations of the instruments in the cross-shore array remained constant for the duration of the experiment. The vertical elevations of the instruments were adjusted manually for only one instrument (denoted by a * in Table D.3). The reason for the adjustment was that the instrument was buried and/or producing a large scour hole beneath its sensor. After each adjustment, measurements were made of

the distance from the ADV sensors to the bed (using the Nortek AS supplied software). This was done on 09/02/2005 and 09/05/2005 (Table D.4). These measurements can be compared to the bathymetry survey from that particular time period and backed out to obtain the ADV distance below the LWF wall ($z = 0$). (*Port 3 does not report a depth because that ADV was a side-looking ADV; it did not measure the bed elevation*).

Table D.1: Wall-Mounted ADV Serial and DAQ Port No.

	Vectrino Serial Number	
Port	8/14/05 – 8/26/05	8/29/05 – 9/10/05
1	7170	7170
2	7149	7149
3	7144	7129
4	7163	7157
5	7130	7154
6	7135	7135
7	7127	7127
8	7160	7160

Table D.2: Coordinates of Cross-shore Instruments 8/15/2005 - 8/26/2005

		Sensor Location			Sample Volume Loc.		
Bay	Vectrino	X(m)	Y(cm)	Z(cm)	X(m)	Y(cm)	Z(cm)
5	N-7160	74.643	50.5	-146	74.643	50.5	-151
6	N-7127	70.994	50.5	-165	70.994	50.5	-170
7	N-7135	67.344	50.5	-179	67.344	50.5	-184
8	N-7130	63.725	54.5	-181.5	63.725	59.5	-181.5
8	N-7163	63.700	42.5	-180.5	63.700	42.5	-185.5
8	N-7144	63.795	43.5	-143.5	63.795	43.5	-148.5
9	N-7149	60.037	51	-200	60.037	51	-205
10	N-7170	56.369	51	-237	56.369	51	-242

Bay	OBS	X(m)	Y(cm)	Z(cm)	X(m)	Y(cm)	Z(cm)
5	2496	74.643	43.2	-151	74.643	n/a	-151
6	2504	70.994	43	-169.3	70.994	n/a	-169.3
7	2499	67.344	43	-184	67.344	n/a	-184
8	2493	63.795	53	-185.5	63.795	n/a	-185.5
8	2501	63.700	44	-181.5	63.700	n/a	-181.5
8	2502	63.820	54.5	-148.5	63.820	n/a	-148.5
9	2494	60.037	43	-205	60.037	n/a	-205
10	2491	56.369	43.5	-242	56.369	n/a	-242

Table D.3: Coordinates of Cross-shore Instruments 8/29/2005 - 9/10/2005

		Sensor Location			Sample Volume Loc.		
Bay	Vectrino	X(m)	Y(cm)	Z(cm)	X(m)	Y(cm)	Z(cm)
5	N-7160	74.643	50.5	-146	74.643	50.5	-151
6	N-7127	70.994	50.5	-165	70.994	50.5	-170
7	*N-7135	67.344	50.5	-179	67.344	50.5	-184
8	N-7129	63.725	54.5	-181.5	63.725	59.5	-181.5
8	N-7157	63.700	42.5	-180.5	63.700	42.5	-185.5
8	N-7154	63.795	43.5	-143.5	63.795	43.5	-148.5
9	N-7149	60.037	51	-200	60.037	51	-205
10	N-7170	56.369	51	-237	56.369	51	-242

Bay	OBS	X(m)	Y(cm)	Z(cm)	X(m)	Y(cm)	Z(cm)
5	2496	74.643	43.2	-151	74.643	n/a	-151
6	2504	70.994	43	-169.3	70.994	n/a	-169.3
7	2499	67.344	43	-184	67.344	n/a	-184
8	2493	63.795	53	-185.5	63.795	n/a	-185.5
8	2501	63.700	44	-181.5	63.700	n/a	-181.5
8	2502	63.820	54.5	-148.5	63.820	n/a	-148.5
9	2494	60.037	43	-205	60.037	n/a	-205
10	2491	56.369	43.5	-242	56.369	n/a	-242

Table D.4: ADV Distance from Sensor to Bed (09/02/2005)

Port	Vectrino	09/02/05 h(cm)	09/05/05 h(cm)
1	7170	6.4	6.9
2	7149	8.5	7.6
3	7129	-	-
4	7157	16.9	11.3
5	7154	20.2	14.9
6	7135	4.1	11.5
7	7127	16.4	11.2
8	7160	12.3	12.1

The cross-shore locations of the wave gauges are shown in Table D.5. Cross-shore locations are in the LWF coordinate system. A description of the relative location of each wave gauge follows.

Table D.5: Cross-Shore wave gauge Array

wave gauge	Bay	X-Location	Description
1	20.0	19.99	Onshore bolt hole - backed out assuming 12 ft. bays
2	12.0	49.23	Onshore bolt hole (from survey of offshore bolt holes)
3	11.0	52.89	Onshore bolt hole (from survey of offshore bolt holes)
4	10.0	56.56	Onshore bolt hole (from survey of offshore bolt holes)
5	9.0	60.10	Centerline of bolt holes at Bay 9
6	8.5	61.94	1.83 m onshore of WG 5
7	8.0	63.31	3.21 m onshore of WG 5
8	7.8	64.98	4.89 m onshore of WG 5
9	7.3	66.51	6.41 m onshore of WG 5
10	7.0	67.42	Centerline of bolt holes at Bay 7
11	6.0	71.18	Onshore bolt hole (from survey of offshore bolt holes)
12	5.0	74.86	Onshore bolt hole (from survey of offshore bolt holes)

D.3 Carriage Instrument Locations

Measurements of the carriage-mounted instruments were made from a slightly different coordinate system because the carriage did not have a fixed cross-shore position. The alongshore (y) and vertical (z) origins remained in the same LWF coordinate system (i.e. $y = 0$ corresponded to the east wall of the LWF and $z = 0$ corresponded to the top of the wall). However, the cross-shore origin (x=0) of the instruments was the *offshore* edge of the center wing (Wing #2). This was selected to simplify the measurements of the carriage instrument locations. As stated previously, the *offshore* edge of Wing #2 was located 46.75 cm *onshore* of the centerline of the MTA. Because a cross-shore location reading from the laser was recorded prior to every wave run, adding the separation distance between the MTA centerline and Wing #2 to the cross-shore laser measurement places the carriage coordinate system in the LWF coordinate system.

Table D.6 provides the port and respective ADV serial number for the carriage-mounted Vectrinos. Three carriage-mounted Vectrino probes were replaced on 08/29/2005. The replacement Vectrino serial numbers are provided in the table.

Carriage instrument coordinate locations are presented in Tables D.7 and D.8. *Note all units are in centimeters in both tables.* Figures D.1 and D.2 provide a pictorial representation of the carriage array.

Table D.6: Carriage-Mounted ADV Serial and DAQ Port No.

	Vectrino Serial Number	
Port	$8/14 - 8/26$	$8/29 - 9/10$
1	7140	7140
2	7132	7130
3	7166	7163
4	7126	7144

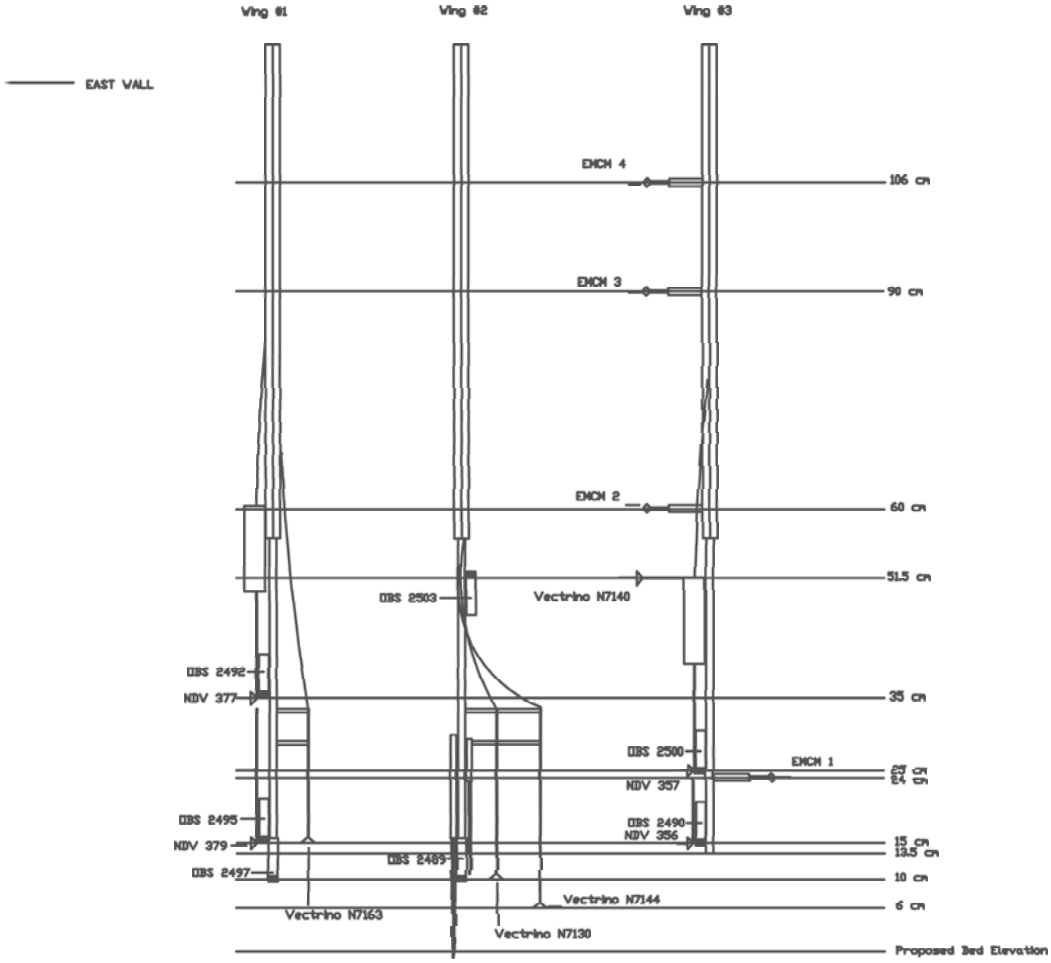

Fig. D.1: Layout of Carriage instruments. Instrument legend displayed in Figure D.2.

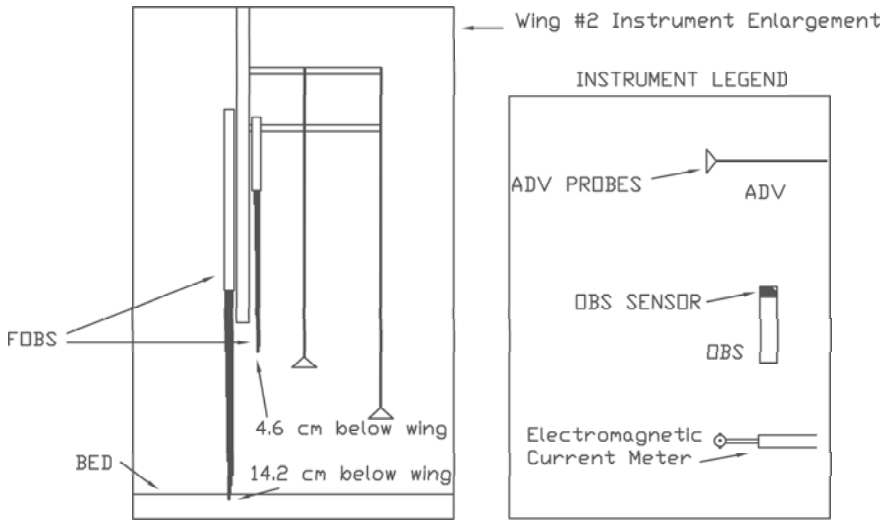

Fig. D.2: (Left) Enlargement of Wing #2 instruments with FOBS detail. (Right) Instrument Legend.

Table D.7: Coordinates of Carriage Instruments 8/15/2005 - 8/26/2005

Instrument	Serial No.	X(cm)	Y(cm)	Z(cm)
NDV	N377	-1.5	140.5	35.0
NDV	N379	18.0	140.0	15.0
NDV	N356	14.5	235.0	15.0
NDV	N357	3.0	235.0	25.0
Vectrino	7166	7.5	156.5	15.0
Vectrino	7132	8.5	186.0	10.0
Vectrino	7126	8.5	191.8	6.0
Vectrino	7140	7.5	211.5	51.5
EMCM	1	7.5	269.0	24.0
EMCM	2	8.0	217.0	61.0
EMCM	3	8.0	216.5	91.0
EMCM	4	8.0	216.5	106.0
OBS	2495	9.5	145.0	15.5
OBS	2492	6.0	145.0	35.5
OBS	2497	16.5	147.5	10.0
OBS	2489	16.5	178.5	10.0
OBS	2503	7.5	181.0	52.0
OBS	2490	7.5	241.0	15.0
OBS	2500	11.0	241.0	25.5
FOBS	lower	9.0	181.1	-1.2
FOBS	upper	9.0	177.0	9.0

Table D.8: Coordinates of Carriage Instruments 8/29/2005 - 9/10/2005

Instrument	Serial No.	X(cm)	Y(cm)	Z(cm)
NDV	N377	-1.0	140.0	35.0
NDV	N379	18.0	140.5	15.0
NDV	N356	14.5	235.5	15.0
NDV	N357	3.0	235.5	25.0
Vectrino	7163	8.0	157.0	15.0
Vectrino	7130	8.0	186.0	10.0
Vectrino	7144	8.0	192.5	6.0
Vectrino	7140	8.0	212.0	51.5
EMCM	1	7.5	96.0	24.0
EMCM	2	8.0	217.0	60.0
EMCM	3	8.0	217.0	90.0
EMCM	4	8.0	217.0	105.0
OBS	2495	9.5	145.0	15.5
OBS	2492	6.0	145.0	35.5
OBS	2497	17.0	148.5	10.0
OBS	2489	17.0	179.0	10.0
OBS	2503	7.5	181.0	52.0
OBS	2490	7.5	241.0	15.0
OBS	2500	11.0	241.0	25.0
FOBS	lower	9.0	181.1	-1.2
FOBS	upper	9.0	177.0	9.0

Table D.9: FOBS Sensor Array Coordinate Locations

Lower Probe	X (cm)	Y(cm)	z(cm)
Channel 0	9.0	181.0	-1.0
Channel 1	9.0	181.0	0.0
Channel 2	9.0	181.0	1.0
Channel 3	9.0	181.0	2.0
Channel 4	9.0	181.0	3.0
Channel 5	9.0	181.0	4.0
Channel 6	9.0	181.0	5.0
Channel 7	9.0	181.0	6.0
Channel 8	9.0	181.0	7.0
Channel 9	9.0	181.0	9.0
Upper Probe			
Channel 10	9.0	177.0	9.0
Channel 11	9.0	177.0	11.0
Channel 12	9.0	177.0	14.0
Channel 13	9.0	177.0	17.0
Channel 14	9.0	177.0	21.0
Channel 15	9.0	177.0	26.0
Channel 16	9.0	177.0	32.0
Channel 17	9.0	177.0	38.0
Channel 18	9.0	177.0	44.0
Channel 19	9.0	177.0	51.0

E. INSTRUMENT CALIBRATIONS

The NDVs and Vectrinos were factory calibrated, thus, requiring no additional calibration prior to deployment. The resistance-type wave gauges were calibrated as the LWF was filled with water. Voltages were recorded at depth intervals, and calibrations were calculated corresponding to best fit linear regressions for each gauge. The OBSs and FOBSs required additional calibration, however (described further in the next section).

E.1 Optical Instrument Calibration Setup

The FOBS and OBS were both calibrated prior to the CM portion of CROSSTEX (preceding the OHK deployment) and following the OHK deployment.

The FOBS and OBS were calibrated in a recirculating chamber (Figure E.1) composed of a clear, plexiglass rectangular shell with a matte black PVC cylindrical pipe mounted vertically in the interior [*Downing and Beach* (1989)]. A propeller motor was mounted at the base of the cylinder to propel the fluid up. The lid of the rectangular tank was composed of a split racetrack channel that divided and redirected the flow to the sides of the tank and back down to the propeller. The motor was connected to a variable speed power supply that allowed the user to determine the proper speed to uniformly suspend sediments in the solution. The lid of the tank contained locking latches to reduce air entrainment inside the tank.

To calibrate the FOBS, one probe was inserted in the tank at a time, oriented vertically, down the centerline of the cylindrical chamber. To calibrate the OBSs, a wooden plank was secured to the cylindrical chamber that supported 4 OBSs at a time (Figure E.2). The OBSs were oriented vertically on the plank such that the sensors pointed horizontally across the chamber, perpendicular to the direction of flow. The sensors faces were oriented to eliminate interference from adjacent OBSs or the sidewall of the cylinder.

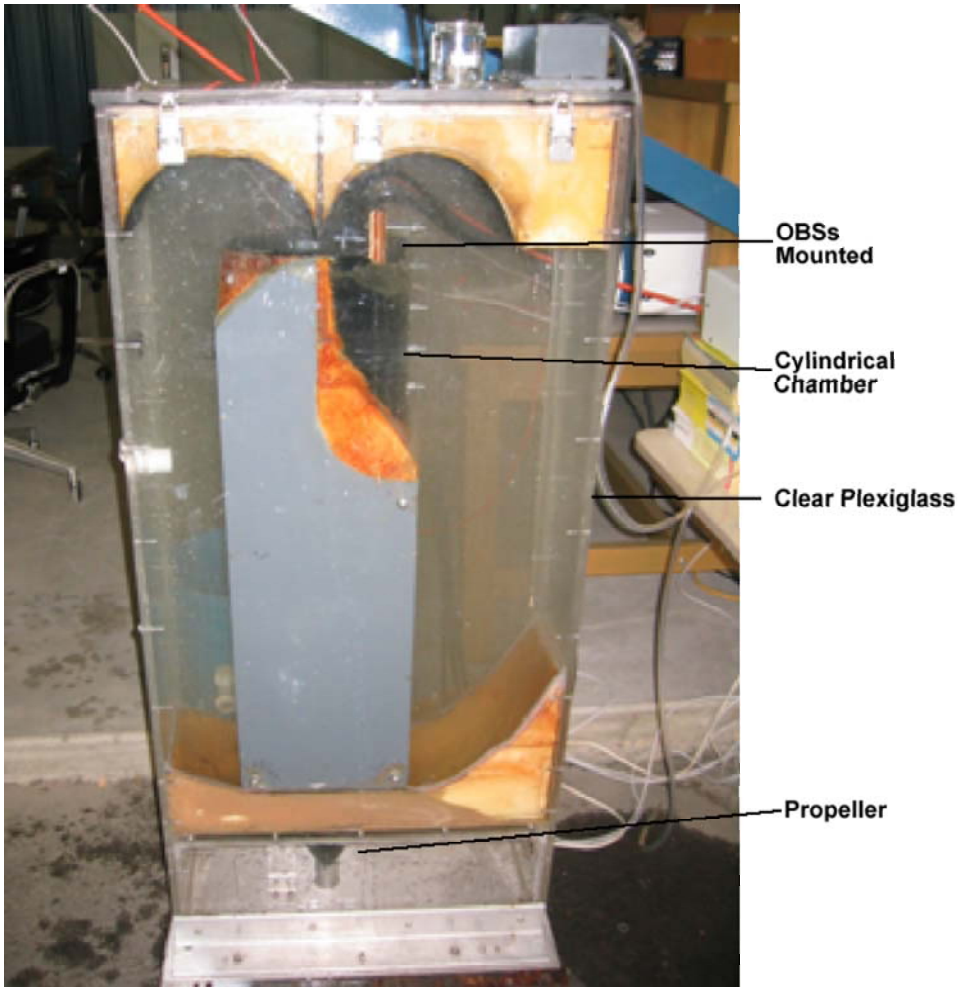

Fig. E.1: OBS and FOBS plexiglass calibration tank. The black vertical cylindrical chamber is housed by the gray rectangular chamber in the center of the tank.

E.2 Calibration Method

The typical procedure involved recording a 3-minute time series of OBS voltages over a range of concentrations. The first recorded test was always conducted with zero-concentration of sediments in the tank (with the motor running) to determine the baseline OBS voltage means. Next, dried beach sand was added in pre-determined increments, augmenting the suspended sediment concentration with each addition.

In the interest of ensuring the most accurate calibration technique, two calibration methods were initially incorporated. The first method (called M1, hereinafter) assumed that a known volume of water resided in the tank (99 L in this case). A predetermined

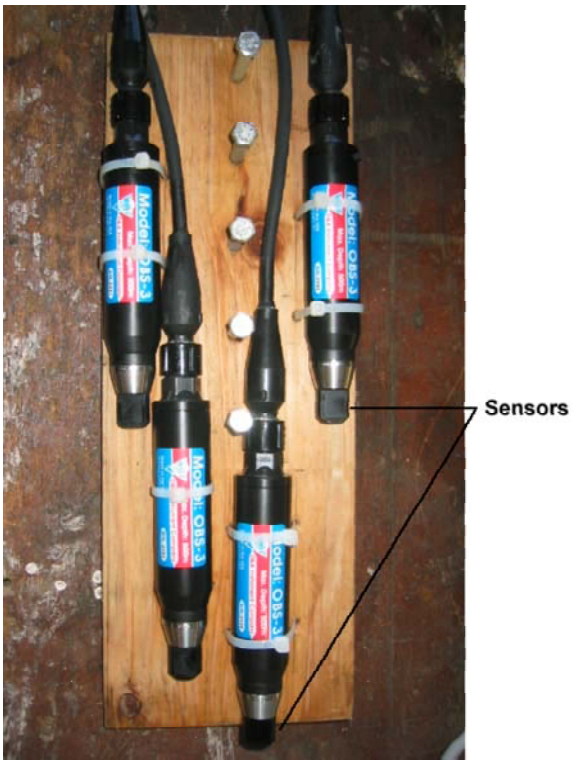

Fig. E.2: 4 OBSs mounted on wooden plank ready for vertical placement in calibration tank cylinder. Sensors are towards bottom of OBSs in image and face horizontally across the cylinder when mounted in the calibration tank, perpendicular to the flow direction.

mass of dried beach sand was added for each subsequent test. The SSC was known directly as the mass of sand per volume of water.

An assumption made during this process, however, is that the added sand volume did not alter the volume of the total solution. In other words, the errors introduced by adding sand volume to the solution were small when compared to the large volume of water in the calibration tank.

The second test method (called M2, hereinafter) did not make any direct assumptions about volume of solution. Instead, the objective was to add sand in pre-determined increments as above and take samples of the solution after each increment.

Prior to any testing, a series of small glass jars were weighed, and the dry mass of the jars was recorded. Following each addition of sand, a peristaltic pump was used to sample solutions from the calibration tank. Samples were gathered in proximity to the

OBS sample volumes. The sampled solution was placed in a glass jar, where the total weight of the jar and solution was recorded. The jars were dried (without lids) in an oven at $43^oC(110^oF)$ for a minimum of 24 hours. Finally, the mass of the dried sand in the solution was obtained by weighing the *dry jar (with lid) and sediment* and subtracting the weight of the *dry jar only.* The difference between the total weight of the *jar plus solution* and the *dry weight of the jar and sediment* yielded the mass of the water in solution. The volume of water was determined by dividing the mass of the water by the density of the water (assumed to be 1000 kg/m^3 in this freshwater case). This procedure yielded the mass of sand and volume of water and, thus, the concentration of the sand in water.

This procedure required some assumptions as well, however. First, we assumed that the pump sampled a representative solution from the flow in the tank. It is difficult to verify this, however, because the pump sampled from a rapid moving fluid-sediment solution through a small diameter tube. An accurate representation of the sediment concentration may not have been sampled each time. Additionally, the glass storage jars allowed for only a small sample of solution to be collected. Therefore, errors in sampling became more significant than if larger solutions had been sampled.

E.3 Calibration Method Selection

The two methods (M1 and M2) were compared for two tests of 4 OBSs each. Best fit linear and quadratic regression lines were computed for the correlation between the mean OBS voltages and the SSC. To compare the two methods, the r^2 correlation was determined.

The best fit linear and quadratic r^2 correlation coefficients are shown in Table E.1 for each method. It is apparent in some cases that the correlation coefficient values did not differ greatly between the two methods, though the regressions appeared (visually) to be slightly less accurate for the results of Method M2 than the results of Method M1 (Figures E.3-E.4). This trend was true for both the linear and quadratic regressions of both regressions. The r^2 coefficients increased slightly in both methods when a quadratic

regression was computed, but Method M1 still returned higher r^2 values than Method M2.

Table E.1: OBS Calibration Method Percent Errors

	Linear Regression		Quadratic Regression		% Error	
OBS	r^2_{M1}	r^2_{M2}	r^2_{M1}	r^2_{M2}	Linear	Quad.
2500	0.998	0.964	1.000	0.990	3.40	1.00
2501	0.998	0.966	0.999	0.991	3.20	0.80
2502	0.997	0.962	1.000	0.992	3.50	0.80
2503	0.991	0.949	0.998	0.990	4.20	0.80
2489	0.997	0.992	1.000	0.994	0.50	0.60
2491	0.997	0.993	1.000	0.995	0.40	0.50
2492	0.997	0.992	1.000	0.994	0.50	0.60
avg	0.996	0.974	1.000	0.992	-	-

The percent difference between the r^2 values was calculated as a means for further comparison:

$$\%\text{Difference} = (r^2_{M1} - r^2_{M2})/r^2_{M1} \times 100 \tag{E.1}$$

The final two columns on the right of Table E.1 depict the percentage differences between the r^2 values of Method M1 and Method M2 for the Linear and Quadratic regression equations, respectively. The correlation between the two calibration methods was as large as 4.20%. For that particular OBS (s/n #2503), this corresponds to a 3 g/L prediction error in suspended sediment concentration, which may be significant depending upon the expected SSC in the area at which the instrument will be deployed.

One thing to note is the percentage difference trends between the first set of OBSs (#2500 - #2503) and the second set of OBSs (#2489, #2491 and #2492). The percentage differences in the linear regression column for the first set of OBSs (3-4%) far exceeded the percentage differences in the same column for the second set of OBSs (<1%). Some of this inconsistency can be explained through human error. However, much of the inconsistency is probably attributable to the inconsistent sampling technique of method M2. If the % errors between the two methods were random, then a different explanation may suffice. However, there are two obvious trends between the two groups of OBSs that were sampled, alluding to a potential sampling problem with method, M2.

The explanation is probably human error in this situation as well. However, caution was exercised because the errors introduced were not random. If human sampling method errors can lead to such a large variation in percentage errors, method M2 may not be the most consistent method to calibrate OBSs.

The decision was made, therefore, to calibrate the remaining OBSs following the procedure of Method M1, for several reasons. First, Method M1 required less procedural time than Method M2. Second, the data collected following the procedure of M1 had a higher correlation than the data collected through Method M2, and, thus, was determined to be more reliable. The percentage differences between the correlation coefficients of the two methods were not large; however, the objective during calibration was to be as accurate as possible to reduce errors. A higher correlation coefficient denotes more consistency between the obs voltages and SSC.

The small percentage differences between the two methods corresponded up to a 3 g/L prediction error in concentration over a 25 g/L range of concentrations. If the expected in situ concentrations measured by the OBSs were large, the differences in calibration methods would not have a large impact on predictions. In other words, if large concentrations are expected in the region the OBS will be deployed, then calibration errors would not influence the measurements greatly. However, the expected range of suspended sediment concentrations in the surfzone were unknown prior to CROSSTEX, therefore the calibrations needed to be as accurate and consistent as possible.

The remaining OBSs were calibrated with Method M1. All OBS calibrations had a linear trend at low concentrations, with high correlation to the linear regression. However, towards higher suspended sediment concentrations, the curves began to taken on a parabolic shape. Quadratic best fit regression lines were selected for the calibrations based on the increased correlation to the data and the visually parabolic shape of the Concentration vs. Voltage calibration curves (See Figures E.3 - E.4). *Note: OBS #2493 was calibrated prior to the OHK deployment by the CM group. However, it could not be postcalibrated due to a cable connection that was no longer watertight. Therefore, the pre-calibration constants were used instead (Table E.4), but no plot is displayed of this calibration.*

E.4 Optical Instrument Calibrations

Mean voltages for the FOBS and OBS sensors were computed for each sensor over a 3-minute time series. The length of the time series allowed sufficient representation of the mean concentration of the flow in front of the sensors during that period. Calibrations were computed through quadratic regression analysis. The coefficients for the calibration equations follow a $y = ax^2 + bx + c$ format and are detailed in the following tables. 'y' is the suspended sediment concentration (g/L) expected for voltage, 'x'. Calibration coefficient tables for the OBS and FOBS are listed below followed by calibration curves of the regression analysis for each sensor. **Note: FOBS channel 12 was lost during the OHK deployment (beginning with file: fobs_082505_1215.txt). For the remainder of the experiment, channel 12 data does not appear in the datafile. The higher channels, 13 to 19, are consequently recorded in the columns for channels 12 to 18.**

The OBS sensors were calibrated by C. Scott, G. Guannel and J. Magalen. The FOBS sensors were calibrated by C. Scott, T. Suzuki and J. Magalen. Calibration routines were run by C. Scott and J. Magalen.

Table E.2: OBS Calibration Coefficients: $y = ax^2 + bx + c$

OBS	a	b	c	r^2
[-]	[(g/L) / V2]	[(g/L)/V]	[g/L]	[-]
2480	0.07	3.12	13.80	1.000
2489	0.06	2.69	11.72	1.000
2490	0.06	3.20	14.21	1.000
2491	0.07	3.00	12.91	1.000
2492	0.05	2.40	10.43	1.000
2493	0.02	2.57	12.14	0.999
2494	0.06	2.40	10.56	1.000
2495	0.05	3.07	13.93	1.000
2496	0.04	2.57	11.74	1.000
2497	0.06	2.94	13.14	1.000
2499	0.05	2.59	11.83	1.000
2500	0.05	2.67	12.00	1.000
2501	0.06	3.12	13.92	0.999
2502	0.07	2.98	12.95	1.000
2503	0.09	2.60	10.84	0.998
2504	0.05	2.58	11.64	1.000

Table E.3: FOBS Calibration Coefficients: $y = ax^2 + bx + c$

Lower Probe	a	b	c	r^2
[-]	[(g/L) / V2]	[(g/L)/V]	[g/L]	[-]
0	1.15E-05	0.018	-1.54	0.997
1	1.40E-05	0.018	-2.08	1.000
2	6.71E-06	0.014	-1.12	0.996
3	9.12E-06	0.017	-0.46	0.998
4	1.26E-05	0.019	-1.00	0.996
5	3.22E-05	0.030	-0.81	0.995
6	1.57E-05	0.021	-0.64	0.998
7	1.60E-05	0.018	-0.73	0.999
8	1.51E-05	0.021	-0.38	0.996
9	1.18E-05	0.018	-0.57	0.997
Upper Probe				
[-]	[(g/L) / V2]	[(g/L)/V]	[g/L]	[-]
10	9.99E-06	0.016	-1.39	0.997
11	1.06E-05	0.016	-2.58	0.988
12	6.33E-06	0.022	-4.18	1.000
13	1.16E-05	0.016	-1.68	0.995
14	6.78E-06	0.016	-1.28	0.999
15	1.57E-05	0.017	-4.29	0.999
16	1.22E-05	0.016	-1.12	0.985
17	1.50E-05	0.016	-0.23	0.991
18	1.19E-05	0.014	-0.28	0.997
19	1.56E-05	0.017	-0.87	0.999

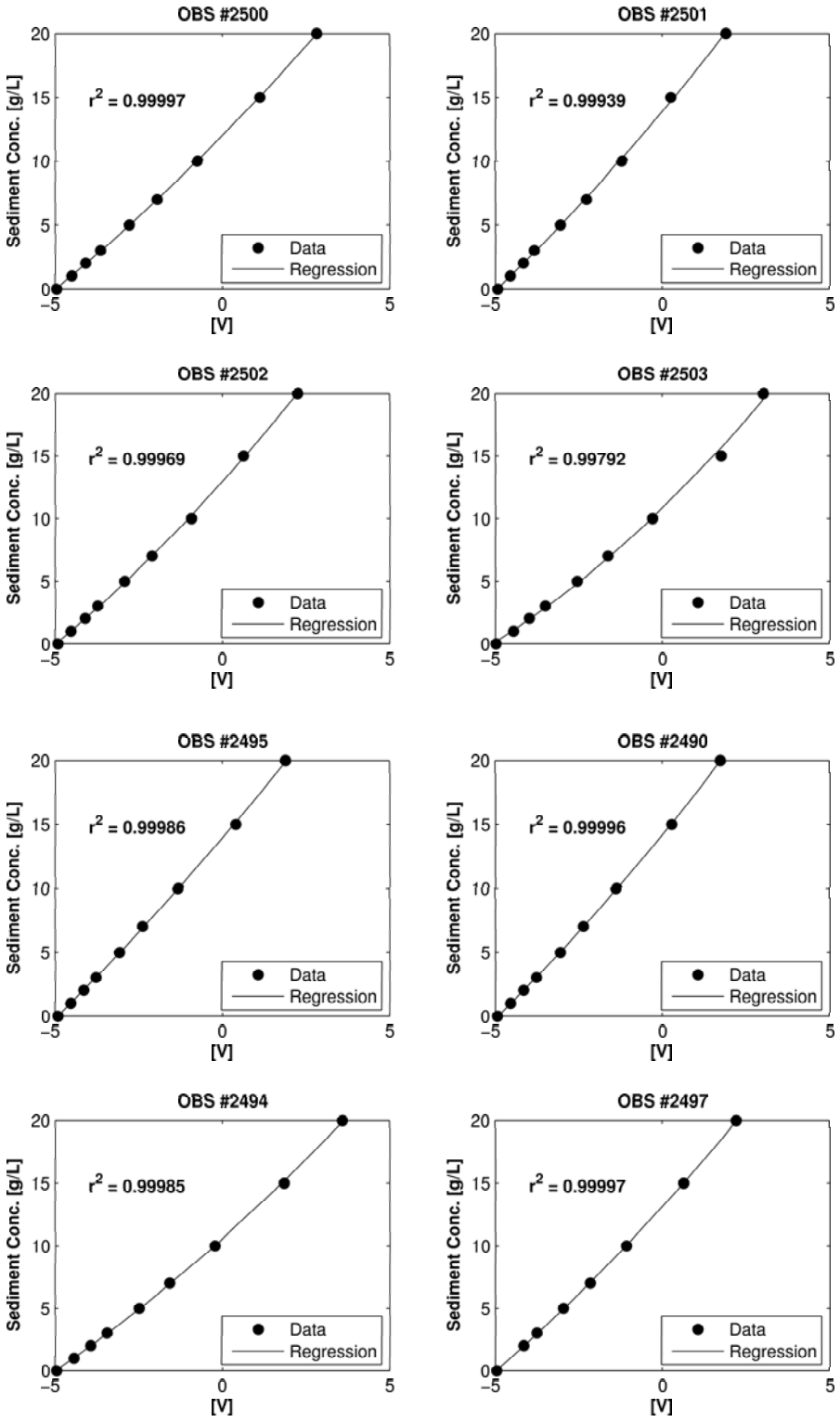

Fig. E.3: Quadratic regression calibration curves for OBSs (I).

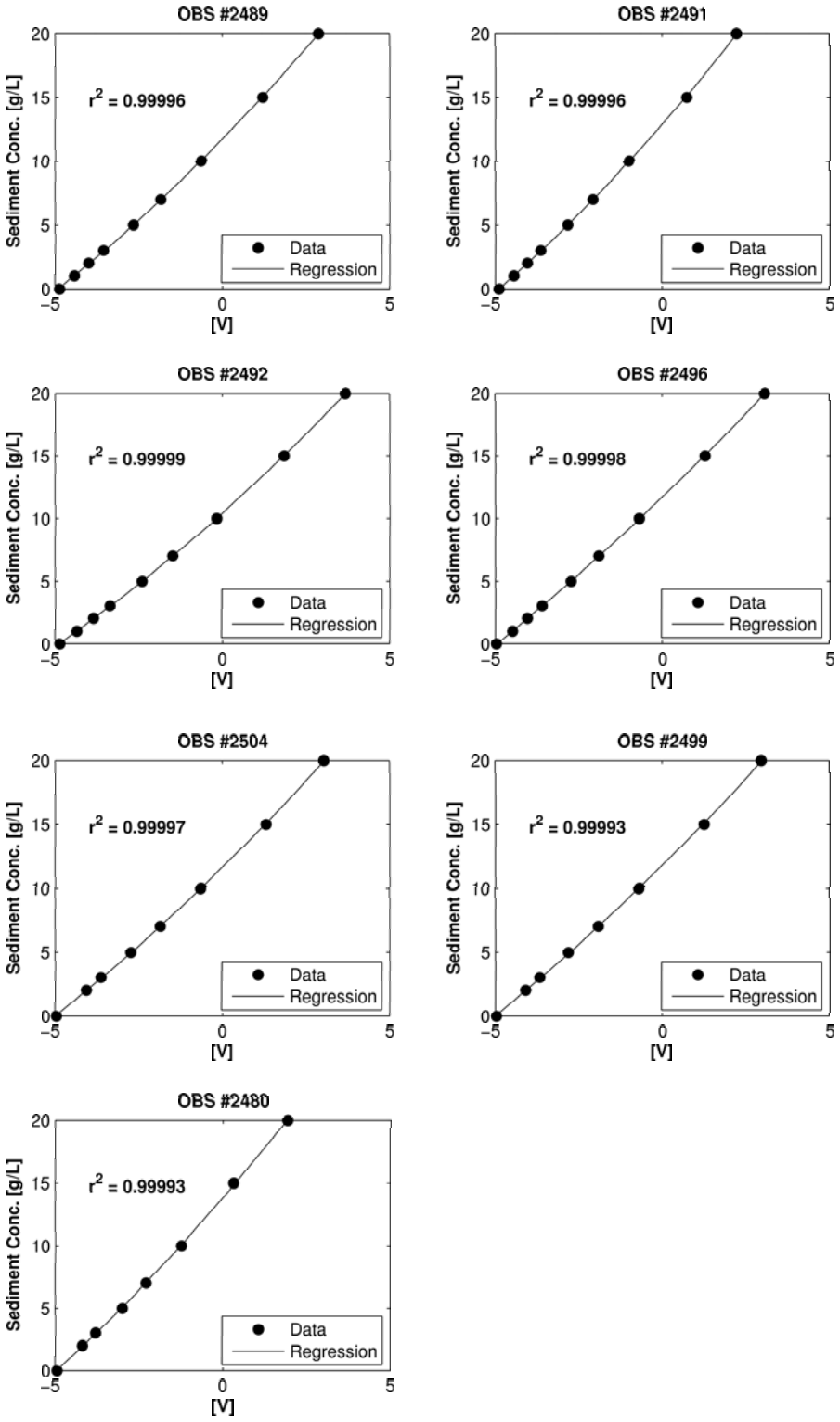

Fig. E.4: Quadratic regression calibration curves for OBSs (II)

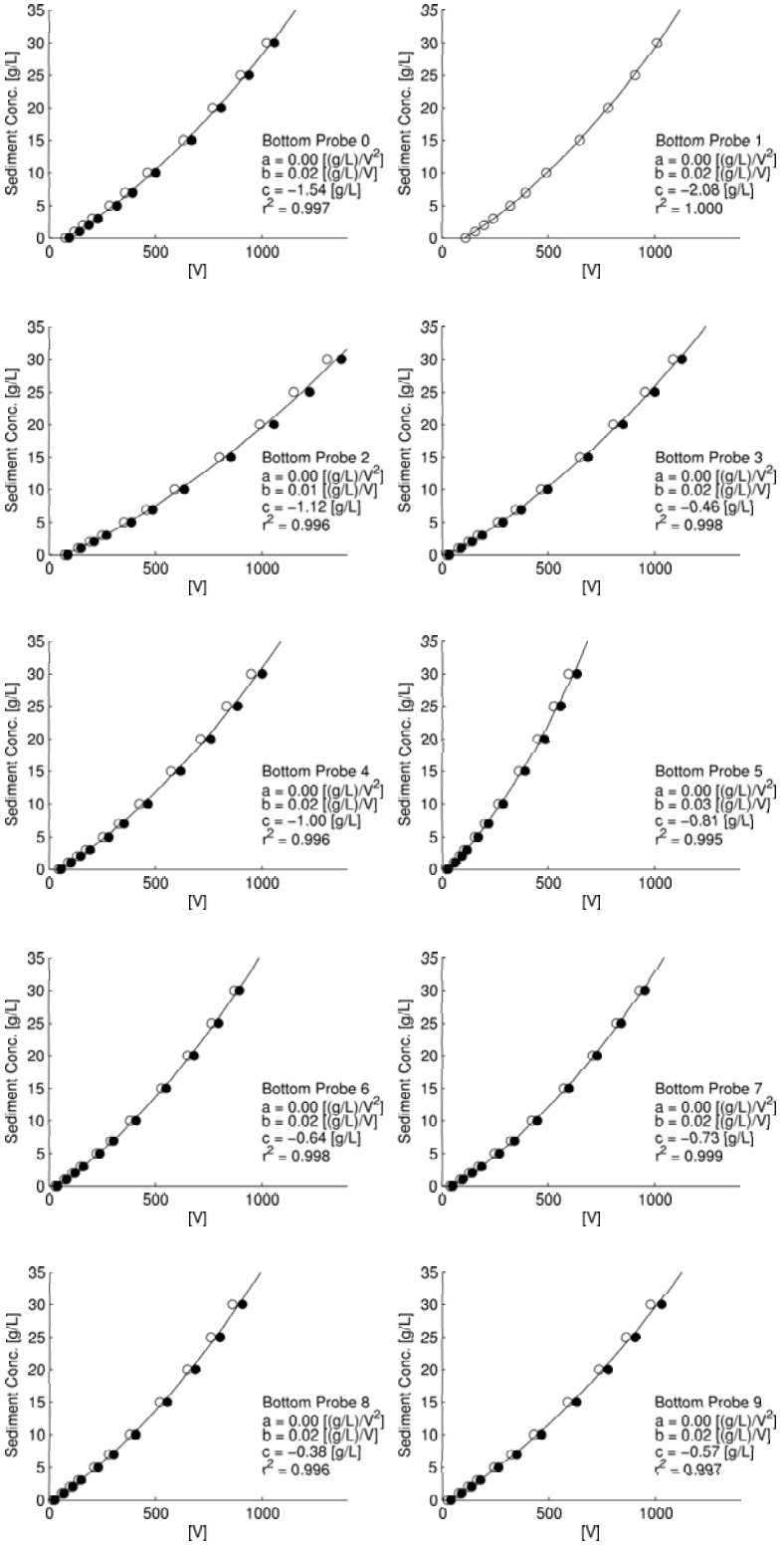

Fig. E.5: Lower FOBS Calibration Curves (*analysis routine by C. Scott*). Pre-calibration (open symbols), Post-calibration (closed) and best-fit regression line.

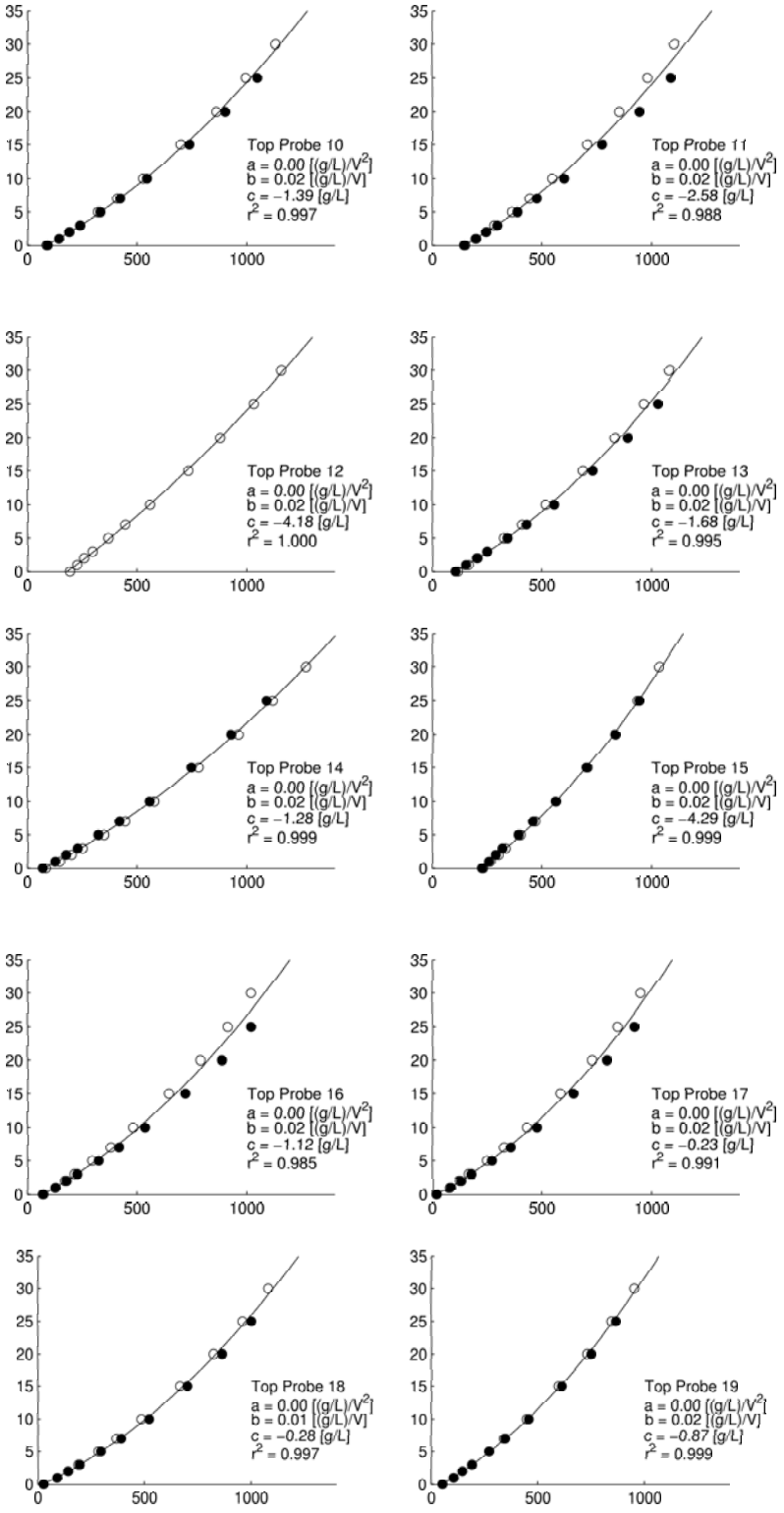

Fig. E.6: Upper FOBS Calibration Curves (*analysis routine by C. Scott*). Pre-calibration (open symbols), Post-calibration (closed) and best-fit regression line.

F. INSTRUMENT ERROR ANALYSIS

F.1 Velocimeters

When there was a sufficient number of backscattering particles in the water column, the accuracy of the Vectrino velocimeters was $\pm 0.5\%$ of the measured velocity $\pm 1 mm/s$ [*Nortek* (2004)]. For a 1 m/s velocity, this corresponds to a 0.004-006 m/s error in estimation. If there was not a sufficient number of particles in the water column, the data files tended to be rather noisy in appearance (i.e. many spikes to unreasonably positive (or negative) velocities). When this occurred, a subjective decision needed to be made about which data files to use.

In an attempt to objectively single out 'noisy' data files from clean data files, we looked at the total number of flagged 'outliers' from the filtering routines (Section 2.6.3) and compared to the total number of data points in a file. The objective was to set a threshold by which to deem files usable. If the percentage of outliers to the total number exceeded a certain threshold, the file would not be used.

This was not a sufficient method, however, because it did not always eliminate noisy data files. Some data files were extremely noisy (visually), but did not generate a large number of points outside the phase-space [*Goring and Nikora* (2002)]. The result was a noisy data file (in appearance) with a relatively low ratio of outliers to total data points. For the purposes of this analysis, data files were deemed noisy if a significant portion of the wave signal was not visible in the data portion under analysis.

F.2 Wave Gauges

At times during the OHK portion of the experiment, wave gauge wires were partially buried by the migrating sand bar. Therefore, a test was conducted to determine the errors introduced in water surface elevation prediction when a wave gauge was buried in sediment. Three 5-minute water surface elevation time series' were collected for different

burial scenarios: A previously buried wave gauge (baseline), the buried wave gauge with an additional 10 cm of sediment added, and the same buried wave gauge with a second 10 cm increment of sediment added (total of 20 cm).

The values presented in Table F.1 are *not* from a de-meaned voltage time series, but, rather, are just voltages converted into meters for comparison purposes. The same wave gauge was used for each comparison (wave gauge 12, located at Bay 5):

Table F.1: Buried Wave Error Estimates

Sand Elevation	Water Surface Elevation (m)
baseline	-0.266
10 cm	-0.216
20 cm	-0.156

From this analysis, a wave gauge that is buried 20 cm may result in a water surface elevation error of 10 cm.

F.3 Optical Backscatter Sensors

F.3.1 OBS - Water Clarity and Ambient Light

It is well known that OBSs are highly sensitive to variability in grain size and shape [*Conner and De Visser* (1992); *Lynch et al.* (1994) *Bunt et al.* (1999)]. OBSs have also been found to be sensitive to color in the ambient surroundings (i.e. calibration tanks), sediment color and type, and bubbles [*Conner and De Visser* (1992); *Lynch et al.* (1994); *Bunt et al.* (1999); *Sutherland et al.* (2000)]. Therefore, in support of previous studies, the OBSs were subjected to an error analysis in October, 2005, after the completion of the CROSSTEX experiment, in an attempt to quantify the effects these variations have on OBS output. Three tests occurred to determine the effects of

1. Clean Water (Tap) vs. Turbid Water (LWF CROSSTEX)
2. Dark Color (Blue) Bucket vs. Light Color (White) Bucket
3. Bubbles

on the OBS voltage outputs.

The dry, natural beach sand used for the CROSSTEX experiment contained a large amount of dirty, fine sediments, which became suspended or dissolved in solution rapidly under wave action. To reduce the turbidity in the water, it was necessary to drain and fill the LWF repeatedly. Therefore, at any given time, the murkiness of the water varied depending on the amount of wave activity that occurred since the flume had last been drained. It was inconvenient to drain the tank frequently so it was important to quantify the effect of clear water versus turbid water on OBS mean voltages, to estimate the errors that might be associated with suspended sediment predictions.

Two water samples taken during the CROSSTEX experiment were analyzed. One sample was taken following the CM deployment. A second sample was taken during the OHK deployment. The water sampled during the CM rotation had a higher turbidity (visually) than the water sampled during the OHK rotation. The CM sample was contained in a dark blue colored bucket, while the OHK sample was contained in a white colored bucket. This scenario allowed for the analysis of the effects of both color and water clarity on OBS measurements. One OBS (s/n #2500) was used for the analysis. The OBS was held vertically against the inside of the bucket (sensor pointing horizontally across the bucket). Table F.2 describes the 4 tests that were conducted on 10-10-2005.

Table F.2: OBS Ambient Light and Turbidity Sensitivity Tests

Run #	Test Dur.(min)	Bucket Color	Water Type
2	3	Blue	Clean (Tap)
3	3	Blue	Dirty (LWF)
4	3	White	Clean (Tap)
5	3	White	Dirty (LWF)

The first two runs measured the effects of the tap water versus CROSSTEX water within the same colored buckets. The mean voltages from the tap water cases were used as the baseline for comparison so that positive voltage differences corresponded to increased turbidity. The second test compared the mean voltages observed by the OBS for the clear (tap) water situation for each colored bucket. The objective was to quantify the effect the different colored buckets had on the amount of ambient light that influenced

the OBS mean voltage readings. Table F.3 displays the voltage increases recorded by the OBS for these two tests.

Table F.3: OBS Ambient Light and Turbidity Sensitivity Analysis

Bucket	Volt Diff.	Difference [g/L]	% Chg.	Description
Blue	0.181	0.485	3.66	Turbid vs Tap Water
White	0.088	0.235	1.78	Turbid vs Tap Water
Blue vs. White	0.016	0.043	0.32	Tap Water

As expected, the water used during the CM and the OHK portions of CROSSTEX caused increases in the mean voltages recorded by the OBSs. The water in the blue colored bucket had a higher turbidity than the water in the white bucket and, thus, resulted in a larger voltage difference (3.7%) in turbid vs. tap water compared to the voltage increase of turbid vs. tap water in the white bucket. In both colored buckets, the increases were of the order of 0.1v to 0.2v. For OBS #2500, a voltage increase of this magnitude corresponded to a concentration increase of 0.25-0.5 g/L, based on the calibration curve estimates. (Table E.4).

The second test directly compared the mean voltage outputs of the OBS in tap water in the two different colored buckets. The blue bucket signal was used as a baseline for comparison. The result was a slight increase in voltage recorded by the OBS in the white bucket. This amounted only to a change of 0.32% compared to the mean voltage recorded in the darker, blue colored bucket. This makes intuitive sense as the white bucket was more translucent than the blue bucket, and, thus, allowed more light to reach the OBS sensor. However, it does not appear that ambient light affects the mean OBS voltage recordings to a large extent. For this particular OBS (S/N #2500), this would amount to approximately a 0.04 g/L increase in estimated suspended sediment.

F.3.2 OBS - Bubbles

Due to the uncertainty of the effects of bubbles in the surfzone on OBS readings, a bubble error analysis was conducted in the OBS calibration tank after the CROSSTEX

experiment concluded. Four OBSs (s/n #2500, #2501, #2502, #2503) were secured in the calibration tank on the above-mentioned wood plate. Table F.4 describes the tests that were run for this assessment on 10-05-2005.

Table F.4: OBS Bubble Sensitivity Tests

Run #	Dur. (min)	Description
6	1	Still Water Test (Baseline)
7	3	Bubbles Induced Throughout Calibration Tank
8	3	Bubbles (again) Induced Throughout Calibration Tank
9	3	Still Water Test: Slight Residual Bubble Entrainment

The calibration tank was not filled completely with water, leaving an air space in the tank once the cover was secured. When the propeller motor was started, the air space in the tank mixed with the upwelling of water and formed bubbles that eventually traveled down through the tank and back up the cylinder, saturating the tank with bubbles. Different water levels in the tank were used for Runs 7 and 8, generating different bubble scenarios. Run 7, conducted with a lower water level, generated larger-sized bubbles. Run 8, conducted at a higher water level in the tank, generated smaller-sized bubbles that appeared to be distributed more uniformly in the tank than the larger bubbles in Run 7. The effects of the bubbles on the OBS mean voltage readings are described in Table F.5.

Table F.5: OBS Bubble Sensitivity Analysis

	OBS #2500		OBS #2501		OBS #2502		OBS #2503	
Run #	[V] Diff.	% Diff	[V] Diff.	% Diff	[V] Diff.	% Diff	[V] Diff.	% Diff
7	0.164	3.23	0.116	2.34	0.103	2.09	0.087	1.74
8	0.104	2.09	0.094	1.89	0.089	1.81	0.092	1.85
9	0.003	0.07	0.031	0.62	0.002	0.03	0.0004	0.01

Run 6 was used as a baseline for comparison. The voltage differences show the increase in mean voltage due to the bubbles, compared to the still water test of Run 6. In test Runs 7 and 8, bubble saturation had a maximum effect of increasing the mean voltage by 0.164 volts and a minimum effect of increasing the mean voltage by 0.087 volts for OBSs #2500-#2503. These both occurred during test Run 7, when the bubbles did not appear,

visually, to be uniformly distributed in the calibration tank. During Run 8, however, the range of voltage change varied between 0.089 volts and 0.104 volts, when the bubbles in the tank appeared to be uniformly distributed. These changes correspond to percentage differences of 1%-3% over Runs 7 and 8. From the calibration curves presented above, a voltage change on the order of 0.10 volts would cause estimates of concentration to increase by a small amount, 0.26-0.31 g/L, approximately.

A second assessment compared the still water test prior to the introduction of bubbles (Run 6) and the still water test following the introduction of bubbles (Run 9). Tiny, residual bubbles in the calibration tank resulted in slight increases in the mean voltage recorded by the OBSs. The largest effect was seen from OBS #2501, with recorded a difference of 0.031 volts (0.62% difference, 0.097 g/L). Thus, even microscopic bubbles affect the voltage readings of OBSs.

G. SEDIMENT ANALYSIS

Sediment samples were taken on three occasions from several cross-shore locations of the LWF. The first samples were collected prior to the start of the OHK experiment (08/08/2005). The second samples were collected toward the end of the OHK experiment (09/06/2005). The final set of samples were collected following the OHK experiment (09/10/2005). Each of the sediment samples were sieved through a series of 6 sieves (maximum allowable) at the Oregon State University Soils Laboratory.

The samples collected on 08/08/2005 were sieved twice. The first analysis was immediate (within a few days of collecting the sediment). The second analysis occurred after the OHK experiment. Different sieve sizes were used for the post-experimental analysis to improve estimates of the median grain size. The sieve sizes from the later analysis are reported here and are shown in the left column of Table G.1. The median grain size (d_{50}) from this analysis from each cross-shore location is presented in Table G.2, the values of which are in accordance with an independent analysis by the Cox-Maddux group.

The sediments sampled on 09/06/2005 and 09/10/2005 were sieved at a separate time (post-experimental) and with different sieve sizes than the 08/08/2005 samples. These sieve sizes are shown in the right column of Table G.1. The corresponding median grain diameters from this analysis are displayed in Table G.2.

Table G.1: Sediment Sieve Sizes

08/08/2005		09/06/2005 09/10/2005	
Sieve	d (mm)	Sieve	d (mm)
40	0.420	40	0.420
50	0.300	50	0.300
60	0.250	65	0.208
65	0.208	100	0.149
100	0.149	140	0.106
140	0.106	200	0.075

Table G.2: Median Sediment Grain Sizes, d_{50}

08/08/2005		09/06/2005		09/10/2005	
Bay	d_{50} (mm)	Bay	d_{50} (mm)	Bay	d_{50} (mm)
3	0.227	2	0.238	SWL	0.278
5	0.226	3	0.238	3	0.237
7	0.228	5	0.233	4	0.237
9	0.223	6	0.241	4.5	0.236
10	0.226	7	0.234	5	0.235
12	0.218	8	0.236	5	0.236
-	-	9	0.229	-	-
-	-	10	0.224	-	-

The median grain sizes of the sediment samples were computed through interpolation. A slight increase in grain size was observed between the 08/08/2005 samples and the 09/10/2005 samples. However, diameters ranged between 0.22 mm and 0.24 mm for the duration of the OHK experiment. The exception to this was the sieve analysis from the still water line, at which the median grain size diameter was larger ($d_{50} = 0.28mm$).

Sediment grain size distributions from each sediment sample are presented in Figures G.1 - G.3. The dashed line denotes the median grain size (d50).

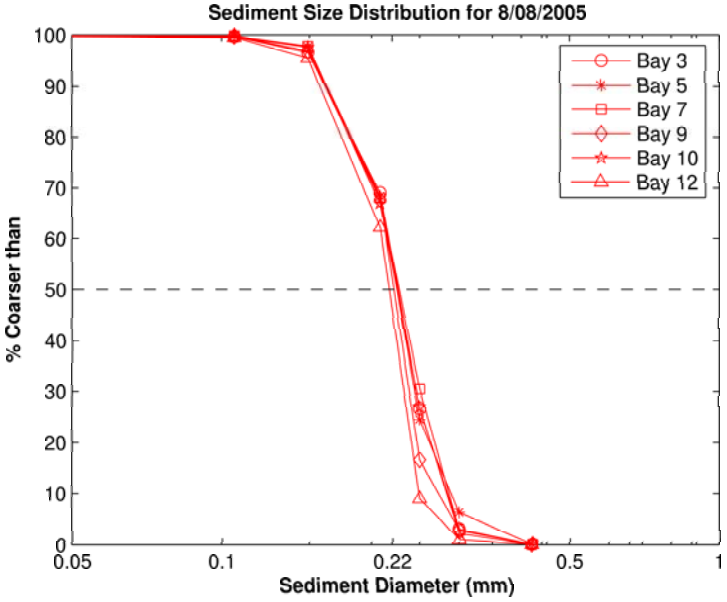

Fig. G.1: Median sediment grain size analysis for 08/08/2005.

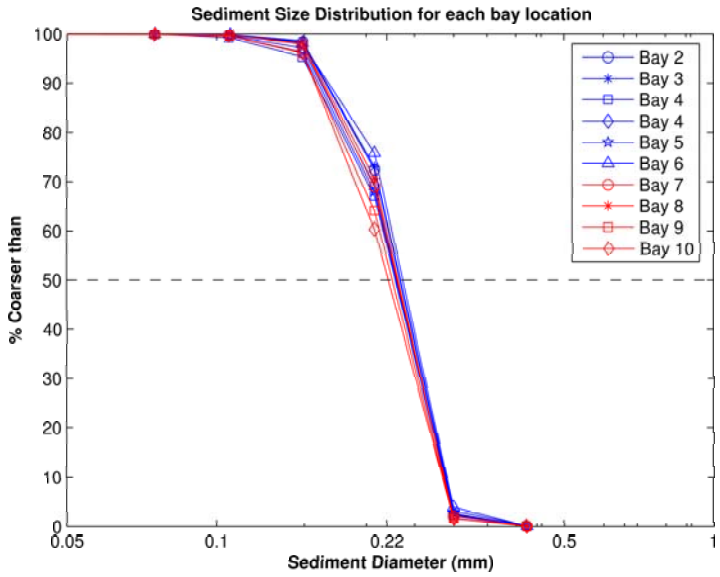

Fig. G.2: Median sediment grain size analysis for 09/06/2005.

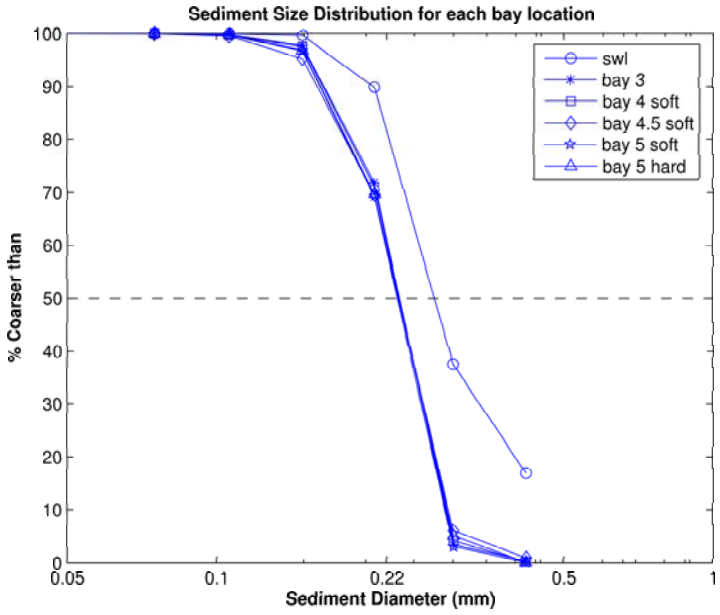

Fig. G.3: Median sediment grain size analysis for 09/10/2005.